Osaka University Knowledge Archive

Title	Development of Functional MultinuclearGold (I) Complexes with Bis (diphenylphosphine) Ligands
Author(s)	井川, 高輔
Citation	大阪大学, 2017, 博士論文
Version Type	VoR
URL	https://doi.org/10.18910/61477
rights	
Note	

Osaka University Knowledge Archive : OUKA

https://ir.library.osaka-u.ac.jp/

Osaka University

Development of Functional Multinuclear Gold(I) Complexes with Bis(diphenylphosphine) Ligands

（ビスジフェニルホスフィン配位子をもつ機能性
金(I)多核錯体の開発）

Kosuke Igawa

Department of Chemistry, Graduate School of Science
Osaka University

2017

Contents

Chapter I. General Introduction. 1

Chapter II. Multinuclear $Au^{I}Ni^{II}$ Complexes with Bis(diphenylphosphino)ethane and Thiomlic Acid.

II-1. Introduction. 5

II-2. Experimental section.

II-2-1. Materials. 7

II-2-2. Synthesis of Au^{I} metalloligands with dppe.

(a) $[Au^{I}_2(dppe)(rac\text{-}H_2msa)_2]$ ([H_4**1**]). 7

(b) $[Au^{I}(dppe)_2]_2[Au^{I}_2(dppe)(R\text{-}Hmsa)(S\text{-}Hmsa)]$ ([**1'**]). 7

II-2-3. Reactions of [H_4**1**] with Ni^{II} ions.

(a) *rac*-$Na_2[Ni^{II}\{Au^{I}_2(dppe)(msa)_2\}]$ (Na_2[**2**]). 8

(b) *rac*-$Mg[Ni^{II}\{Au^{I}_2(dppe)(msa)_2\}]$ (Mg[**2**]). 8

(c) *rac*-$Ni[Ni^{II}\{Au^{I}_2(dppe)(msa)_2\}]$ (Ni[**2**]). 9

(d) *rac*-$Co[Ni^{II}\{Au^{I}_2(dppe)(msa)_2\}]$ (Co[**2**]). 9

(e) *meso*-$Ca_2[Ni^{II}_2\{Au^{I}_2(dppe)(msa)_2\}_2]$ (Ca_2[**3**]). 9

(f) $[Ni^{II}_3\{Au^{I}_2(dppe)(Hmsa)_2\}\{Au^{I}_2(dppe)(msa)_2\}(MeOH)_3]$ ([**4**]). 9

II-2-4. Structural control of $Au^{I}Ni^{II}$ complexes by solution pH. 10

II-2-5. Physical measurements. 10

II-2-6. X-ray structural determinations. 11

II-3. Results and discussion.

II-3-1. Synthesis, characterization of Complexes with dppe and msa.

(a) Au^{I} metalloligands. 13

(b) $Au^{I}Ni^{II}$ heterometal complexes. 15

II-3-2. Structural Control of $Au^{I}Ni^{II}$ Complexes by Counter Cations. 21

II-3-3. Structural Control of $Au^{I}Ni^{II}$ Complexes by Solution pH. 21

II-4. Conclusion. 24

Chapter III. Cage-type Digold(I) Complexes with Bis(diphenylphosphino)methane.

III-1. Introduction. 66

III-2. Experimental section.

III-2-1. Materials. 67

III-2-2. Synthesis of $[Au^{I}_2(dppm)_3]Cl_2\cdot 8.5H_2O$ ([**5**]$Cl_2\cdot 8.5H_2O$). 67

III-2-3. Synthesis of $[Au^{I}_2(dppm)_3](OTf)_2\cdot H_2O$ ([**5**]$(OTf)_2\cdot H_2O$). 67

III-2-4. Thermal conversion of [**5**]$Cl_2\cdot 8.5H_2O$. 67

III-2-5. Physical measurements. 68

III-2-6. Luminescence measurements. 68
III-2-7. X-ray structural determinations. 69
III-2-8. DFT calculations. 71
III-3. Results and discussion.
III-3-1. Synthesis and characterization of complexes.
(a) $[Au^{I}_2(dppm)_3]Cl_2 \cdot 8.5H_2O$ ([**5**]$Cl_2 \cdot 8.5H_2O$). 72
(b) $[Au^{I}_2(dppm)_3](OTf)_2 \cdot H_2O$ ([**5**]$(OTf)_2 \cdot H_2O$). 72
III-3-2. Photoluminescence behavior of [**5**]$Cl_2 \cdot 8.5H_2O$ and [**5**]$(OTf)_2 \cdot H_2O$. 73
III-3-3. Two-step thermal transformation and emission color change of [**5**]$Cl_2 \cdot 8.5H_2O$. 74
III-4. Conclusion. 77

Chapter IV. Concluding Remarks. 94

References. 96

Acknowledgement. 100

Appendix.
Chapter A. Optical Resolution of Thiomalic Acid with Chiral Amine Compound.
A-1. Introduction. 101
A-2. Experimental section.
A-2-1. Materials. 102
A-2-2. Synthesis of [(*S*)-Hpea][(*R*)-H_2msa] ([**7**]). 102
A-2-3. X-ray structural determinations. 102
A-3. Results and discussion.
A-3-1. Crystal Structure of [(*S*)-Hpea][(*R*)-H_2msa] ([**7**]). 103
A-4. Conclusion. 104
A-5. References. 104

Chapter I. General Introduction.

Since the Hofmann's first preparation of triethylphosphine platinum(II) and gold(I) complexes in mid-19th century,[1] phosphine ligands have continued to play an important role in coordination chemistry because of their soft Lewis basicity and π-accepting character like carbon monoxide. The early development of the metal complexes of phosphines was mainly motivated by the catalytic activity of low valent transition metals, *e.g.* palladium(0), rhodium(I), and ruthenium(II). However, from the discovery of strong photoluminescence of $[Au(PPh_3)_3]Cl$ by Dori in 1971[2] and the following reports on catalytic activities[3] and anti-cancer activities[4] of phosphine-gold(I) compounds, a variety of phosphine ligands have been used to prepare gold(I) complexes and the photophysical,[5] catalytic,[6] and medical functionalities[7] of products have been intensively investigated.

Owing to the closed-shell d^{10} electron configuration, gold(I) ions can take a various coordination geometries, *e.g.* 2-coordinated linear, 3-coordinated trigonal-planer, 3-coordinated T-shape, and 4-coordinated tetrahedral structures, depending on the reaction conditions.[6] Owing to the variation of coordination geometries, which allows to afford several kinds of molecular structures from one kind of phosphine ligand, the gold(I)-phosphine chemistry has been widely expanded. For example, triphenylphosphine (PPh_3), which is one of the simplest monophosphine ligands, forms four kinds of mononuclear gold(I) complexes with different coordination geometries; linear $[Au(PPh_3)X]$ and $[Au(PPh_3)_2]^+$, trigonal-planer $[Au(PPh_3)_3]^+$, and tetrahedral $[Au(PPh_3)_4]^+$ (X = monoanions).[7] It has been shown that these complexes show photophysical[5,8] and pharmaceutical properties[4,9] different from each other, indicating that the functionality of the gold(I)-phosphine complexes relies not only on the kind of phosphine ligands, but also on the whole molecular structure or composition of complexes. However, such a widely expanded chemistry has caused a difficulty in the comprehensive study, and the most of gold(I)-phosphine studies have focused on a single species ignoring any other fascinating analogous compounds. Such unexplored compounds are potential 'treasure-trove', embedding excellent or unknown functionalities. To discover a break-through for the next generation of coordination chemistry, it is apparent that the re-evaluation of the classical gold(I)-phosphine chemistry is high desired.

In this study, I focused on the coordination system consisting of gold(I) ions and α,ω-bis(diphenylphosphino)alkanes ($Ph_2P(CH_2)_nPPh_2$ = Ph_2P^PPh_2; Chart 1-1). The ligands are commercially available and their gold(I) complexes have been investigated over several decades.[10-19] Nevertheless, several new fascinating functionalities were discovered in the present study.

It has been reported that the reaction of gold(I) ions with Ph_2P^PPh_2 gives mainly four types of products dependent on the reaction ratios: (i) linear-shaped [Au_2(Ph_2P^PPh_2)X_2] (Au : Ph_2P^PPh_2 = 2:1), (ii) ring-shaped [Au_2(Ph_2P^PPh_2)$_2$]$^{2+}$ (Au : Ph_2P^PPh_2 = 1:1), (iii) cage-shaped [Au_2(Ph_2P^PPh_2)$_3$]$^{2+}$ (Au : Ph_2P^PPh_2 = 2:3), and (iv) mononuclear [Au(Ph_2P^PPh_2)$_2$]$^+$ (Au : Ph_2P^PPh_2 = 1:2) (Chart 1-2). In the case of linear-shaped complex [Au_2(Ph_2P^PPh_2) X_2] (i), each of two gold(I) centers has a terminal Lewis base to give heteroleptic digold(I) complexes, [Au^I_2(Ph_2P^PPh_2)L_2] (L = halide, thiolate or alkenyl). McAuliffe and coworkers isolated this class of complexes using halide ligands (X^-) as the terminal, [Au_2(Ph_2P^PPh_2)X_2], in 1979 for the first time.[10] They also reported that the terminal halide ligands can be replaced by other Lewis bases. When the Lewis base ligands having multi coordinative sites are selected, the [Au_2(Ph_2P^PPh_2)(L)$_2$] complexes can act as metalloligands. For examples, Vicente and coworkers have reported the reactions of the first-raw transition metal ions and the digold metaloligands, [Au_2(Ph_2P^PPh_2)(C≡Cbpyl)$_2$] (bpyl = 2,2'-bipyridin-5-yl), which have terminal coordinative bipyridine sites.[11] Konno and coworkers have reported a series of digold metalloligands containing a diphosphine linker and two terminal tridentate D-penicillaminate (D-pen) ligands, [Au_2(Ph_2P^PPh_2)(D-pen)$_2$]$^{2-}$, which can act as metalloligands toward transition metal ions through N, O, and S atoms of D-pen moieties.[12-15] They also reported that the resulting heterometallic coordination compounds form unique metallosupramolecular structures in the crystalline state, supported by intermolecular C-H$\cdots\pi$ and/or $\pi\cdots\pi$ interactions between Ph_2P^PPh_2 moieties. Therefore, this class of gold(I)-phosphine compounds has been widely utilized as the building block for constructing metallosupramolecular structures.

Unlike (i), the coordination sites of gold(I) ions are fully occupied by phosphine ligands in (ii)-(iv). In the case of ring-shaped complexes [Au_2(Ph_2P^PPh_2)$_2$]$^{2+}$ (ii), two gold(I) ions can form an attractive intramolecular interaction between two ions (aurophilic interaction),[16] which often leads to excellent emission properties for digold(I) structures.[17] For example, Huttner and coworkers have reported that [Au_2(dppm)$_2Cl_2$] show a blue emission derived from intramolecular aurophilic interactions, more specifically, the HOMO (Au-Au $\sigma^*(6s,5d_{z2})$) → LUMO (Au-Au $\sigma(6p_z)$) charge transfer (dppm = bis(diphenylphosphino)methane).[5a] The cage-shaped complexes [Au_2(Ph_2P^PPh_2)$_3$]$^{2+}$ (iii) are also expected to exhibit photoluminescence originating from intramolecular aurophilic interaction. However, this class of complexes has never been structurally characterized, and their structures have been proposed only by spectroscopic analysis.[18] The emission property of this class of digold(I) complexes has not been studied at all. The mononuclear [Au(Ph_2P^PPh_2)$_2$]$^+$ complexes (iv) have applied as emission materials or antitumor medicines. Wilson and coworkers reported that orange emission derived from the LMCT transition (π^*(Ph-Ph) → Au(d)-P(p)) is observed in

$[Au(dppe)_2]PF_6$ (λ_{em} = 595 nm) (dppe = 1,2-bis(diphenylphosphino)ethane).[19] Crooke and coworkers showed an antitumor activity of $[Au(dppe)_2]Cl$.[20]

Based on the above mentioned situations, I selected the linear $[Au_2(Ph_2P^{\wedge}PPh_2)X_2]$ and the cage-type $[Au_2(Ph_2P^{\wedge}PPh_2)_3]^{2+}$ complexes for the further investigation. The linear $[Au_2(Ph_2P^{\wedge}PPh_2)X_2]$ complexes readily bind to soft Lewis bases strongly and possess phenyl groups as supramolecular interaction sites. Generally, it is difficult to isolate a highly hydrophilic compound from a polar solvent. By the introduction of the hydrophobic $[Au_2(Ph_2P^{\wedge}PPh_2)]^{2+}$ units to the hydrophilic target compound, the hydrophilicity should be compensated by the $[Au_2(Ph_2P^{\wedge}PPh_2)]^{2+}$ units. Therefore, it is expected that highly hydrophilic molecules can be easily crystallized by combining with the $[Au_2(Ph_2P^{\wedge}PPh_2)]^{2+}$ unit. For the cage-type $[Au_2(Ph_2P^{\wedge}PPh_2)_3]^{2+}$ complexes, their emission properties have not been investigated at all, in spite of the presence of potentially emissive intramolecular aurophilic interaction moieties in the proposed cage-like structures. Generally, the emission quantum yield is increase by using the more rigid structure that prevents a non-radiative transition. Thereby, this class of complexes are expected to show a strong emission.

In this thesis, first of all, the linear-type digold(I) unit with dppe, $[Au_2(dppe)]^{2+}$, was combined with thiomaic acid (H_3msa). Thiomalic acid (H_3msa) is known as one of the simplest mercapto dicarboxylic acids possessing one thiol and two carboxy donor groups in the structure. Despite its high biocompatibility and high chelating ability to metal ions, its transition metal complexes are mostly unexplored due to high water solubility of msa complexes. By the introduction of the hydrophobic $[Au_2(dppe)]^{2+}$ unit, the complex with msa will be easy to crystalize owing to the decrease of water solubility. Indeed, the digold(I) $[Au_2(dppe)(msa)_2]^{4-}$ and its nickel(II) derivatives were successfully crystallized and structurally characterized based on single-crystal X-ray crystallography.

Next, the cage-like digold(I) complexes with dppm, $[Au_2(dppm)_3]X_2$ (X = Cl, triflate), were prepared and their molecular structures were fully characterized using single-crystal X-ray diffraction analyses. In addition, their emission properties were also investigated. As a result, it was found that these compounds exhibit an extremely high emission quantum yield (ca. 100 %) at room temperature in the solid state. The counter anion dependency on emission property was discussed. Moreover, the reversible, two-step solid phase structural conversion accompanied by an emission color change was observed in the dehydration/hydration and dissociation/coordination cycles of $[Au_2(dppm)_3]Cl_2$.

The coordination system including linear $[Au_2(dppe)]^{2+}$ and msa^{3-} was summarized in chapter II, whereas the emission property of cage-type $[Au_2(dppm)_3]^{2+}$ was described in chapter III.

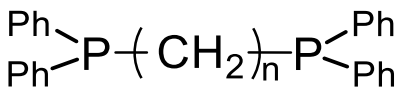

Chart 1-1. Molecular structure of α,ω-bis(diphenylphosphino)alkanes.

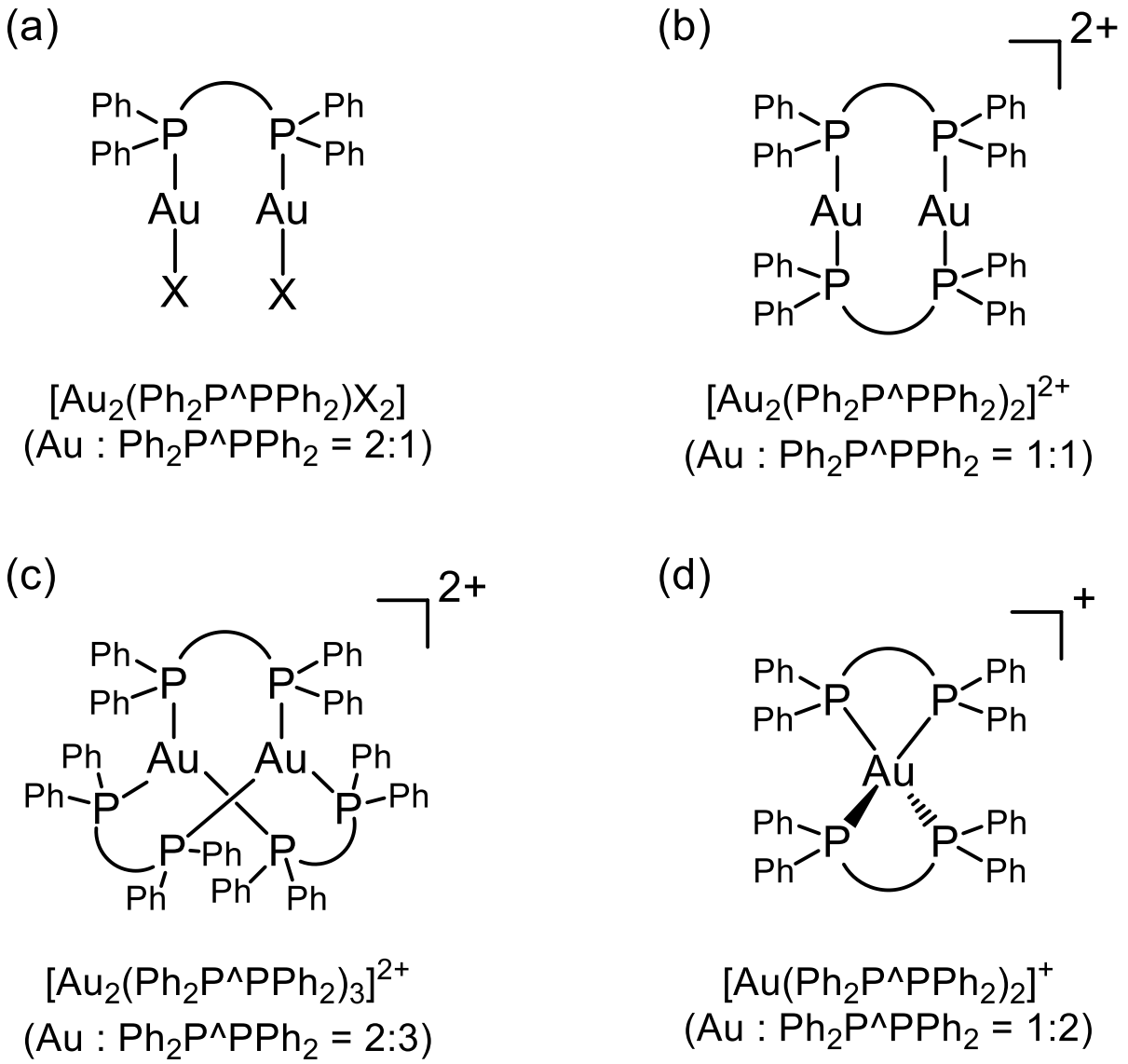

Chart 1-2. Four types of gold-diphosphine complexes (a) linear-type $[Au_2(Ph_2P\text{^}PPh_2)X_2]$ (X = halide, thiolate or alkenyl) (Au : $Ph_2P\text{^}PPh_2$ = 2:1), (b) ring-type $[Au_2(Ph_2P\text{^}PPh_2P)_2]^{2+}$ (Au : $Ph_2P\text{^}PPh_2$ = 1:1), (c) cage-type $[Au_2(Ph_2P\text{^}PPh_2)_3]^{2+}$ (Au : $Ph_2P\text{^}PPh_2$ = 2:3), and (d) mononuclear $[Au(Ph_2P\text{^}PPh_2)_2]^{+}$ (Au : $Ph_2P\text{^}PPh_2$ = 1:2).

Chapter II. Multinuclear $Au^{I}Ni^{II}$ Complexes with Bis(diphenylphosphino)ethane and Thiomlic Acid.

II-1. Introduction

Thiomalic acid ($H_3msa = C_4H_6O_4S$; Chart 2-1) is known as one of the simplest mercapto dicarboxylic acids possessing one thiol and two carboxy donor groups in the structure. The fully deprotonated form of H_3msa is trianionic, which is advantageous to construct coordination compounds with larger anionic charge. In addition, H_3msa has an asymmetric carbon atom next to the thiol group, which produces a pair of enantiomers, *R*- and *S*-H_3msa. The racemate of H_3msa (*rac*-H_3msa) is commercially available, and the enantiopure form is easily accessible by the optical resolution of *rac*-H_3msa using (*R*)- or (*S*)-pea (pea = 1-phenylethanamine) (See appendix A). Therefore, H_3msa can be recognized as a useful chiral S-donating chelating ligand, like L-cysteine and D-penicillamine.

During the early 1940s, Gannon reported that a gold(I) complex of H_3msa ($[Na_2Au(rac\text{-}msa)]_n$) shows an antirheumatoid activity for the first time.[21] Motivated by the finding, the reactivity of H_3msa with major transition metal ions, such as V^{V},[22] Mn^{II},[23] Fe^{II},[23] Co^{II},[23] Ni^{II},[23] Cu^{II},[24] Zn^{II},[25] Cd^{II},[25] Hg^{II},[26] and Ag^{I},[27] were intensively investigated, and their pharmacological activities were examined. However, almost all of the complexes have not been isolated and have been characterized only by absorption spectroscopy in solution. Therefore, insights of coordination behavior of H_3msa has yet to be revealed. In 1990, the first crystal structure of coordination compound of H_3msa, $[Mo^{IV}_3S(S_2)_3(Hmsa\text{-}O,S)_3]^{2-}$,[28] has been reported. Subsequently, five gold complexes, *rac*-$[Au^{I}(msa\text{-}S)_2]^{5-}$,[29] $[Au^{I}(R\text{-}msa\text{-}S)_2]^{5-}$,[29] ($[Au^{I}(\mu_2\text{-}msa\text{-}S)]^{2-})_n$,[30] $[Au^{III}(damp)(Hmsa\text{-}O,S)]$ (damp = 2-((dimethylamino)methyl)phenyl),[31] and $[Ru^{II}_2(\eta^6\text{-}p\text{-cymene})_2(Hmsa\text{-}O,S)_2]$,[32] have been structurally characterized (Chart 2-2). In these crystals, msa^{3-} coordinates to a metal center through a monodentate-*S* or bidentate-*O*,*S* mode, but the most plausible tridentate-*O*,*O*',*S* coordination mode has not been observed. Therefore, the further investigation of the coordination behavior of msa^{3-} to a variety of metal ions, especially first-law transition metal ions, is still a challenging task.

Reports on the crystal structures of the metal complexes with H_3msa is highly limited in number in comparison with those of cysteine and penicillamine, for which more than one hundred crystal structures have been reported.[33] The difficulty in the crystallization of msa^{3-} complexes can be explained by the following two reasons; (i) the high hydrophilicity of msa^{3-} leads to the high solubility in polar solvents, and (ii) the lack of hydrogen bonding donor sites

in the structure of msa^{3-} prevents the formation of supramolecular interactions in crystal. With this in mind, it is expected that the use of hydrophobic auxiliary ligand improves the crystallinity of this class of complexes because of the reduction of the hydrophilicity of msa complexes and the formation of non-covalent interactions between the hydrophobic auxiliary ligands.

In this chapter, the improvement of crystallinity of msa complexes by the introduction of gold(I)-phenylphosphine complex was investigated. As mentioned in the general introduction, the linear-type $[Au_2(Ph_2P^\wedge PPh_2)]^{2+}$ unit readily binds to thiolate ligands to give a heteroleptic product, $[Au_2(Ph_2P^\wedge PPh_2)(SR)_2]$. So, it is expected that the combination of $[Au_2(Ph_2P^\wedge PPh_2)]^{2+}$ with a deprotonated msa gives a linear digold(I) complex, $[Au_2(Ph_2P^\wedge PPh_2)(msa\text{-}S)_2]^{4-}$, which may act as a metalloligand toward transition metal ions using thiolato S and carboxylate O atoms of msa moieties. It is anticipated that the phenyl groups in $Ph_2P^\wedge PPh_2$ moiety form intermolecular C-H$\cdots\pi$ interactions, which improves the crystallinity of products.

It was found that a digold(I) unit with 1,2-bis(diphenylphosphino)ethane (dppe), $[Au_2(dppe)]^{2+}$, readily reacts with H_3msa to form a new digold(I) complex, $[Au_2(dppe)(rac\text{-}H_2msa\text{-}S)_2]$ ($[H_4\mathbf{1}]$) (Chart 2-3). The complex was fully characterized by ^1H and ^{31}P NMR and IR spectra, and elemental analyses. Moreover, the reactivity of the metalloligand $[\mathbf{1}]^{4-}$ to Ni^{II} ions was studied in order to clarify the coordination behavior of msa^{3-} to an octahedral metal center. As a result, three new heterometallic complexes, $[Ni\{Au_2(dppe)(msa)_2\}]^{2-}$ ($[\mathbf{2}]^{2-}$), $[Ni_2\{Au_2(dppe)(msa)_2\}_2]^{4-}$ ($[\mathbf{3}]^{4-}$), and $[Ni_3\{Au_2(dppe)(Hmsa)_2\}\{Au_2(dppe)(msa)_2\}(MeOH)_3]$ ($[\mathbf{4}]$), were obtained dependent on the reaction conditions. As expected, all the three heterometalic complexes were successfully crystallized and structurally characterized by single-crystal X-ray diffraction analyses. These complexes were further characterized by electronic absorption and IR spectra and fluorescent X-ray and elemental analyses. In addition, a unique structural conversion among complexes $[\mathbf{2}]^{2-}$, $[\mathbf{3}]^{4-}$, and $[\mathbf{4}]$ were also discussed based on the electronic absorption, ESI-mass spectroscopy, and magnetic property.

II-2. Experimental section.

II-2-1. Materials.

All starting materials except [Au_2(dppe)Cl_2] were commercially available and used without further purification. All manipulations were carried out under aerobic conditions. [Au_2(dppe)Cl_2] was prepared by modified literature methods.[34]

a) [Au_2(dppe)Cl_2].

To an orange solution containing 2.00 g (5.0 mmol) of Na[$AuCl_4$]·$2H_2O$ in a mixed solvent of H_2O (16 mL) and MeOH (26 mL) was added a colorless solution containing 1.85 g (15.1 mmol) of $S(CH_2CH_2OH)_2$. To the mixture was added a colorless solution containing 1.00 g (2.5 mmol) of dppe in a mixed solvent of $CHCl_3$ (16 mL) and MeOH (4 mL). The solution was stirred at room temperature for 4 h and then MeOH (80 mL) was added to it. The resulting white powder was collected by filtration and dissolved in $CHCl_3$ (320 mL). After filtration, the filtrate was evaporated to dryness to give a white powder of [Au_2(dppe)Cl_2]. Yield: 2.09 g (96%). IR spectrum (cm^{-1}, KBr disk): 1436 (ν_{Ph}), 1105 (ν_{P-Ph}).

II-2-2. Synthesis of Au^I metalloligands with dppe.

a) [Au_2(dppe)(*rac*-H_2msa-*S*)$_2$] ([$H_4$1**])**

To a white suspension containing 2.00 g (2.3 mmol) of [Au_2(dppe)Cl_2] in EtOH (150 mL) were added a colorless solution containing 0.77 g (5.1 mmol) of *rac*-H_3msa in EtOH (50 mL) and a 0.1 M aqueous solution of NaOH (51 mL). The mixture was stirred at room temperature in the dark for 1 d, and the resulting white precipitate of [H_4**1**] was collected by filtration and washed with two portions of EtOH (10 mL) and a portion of $CHCl_3$ (10 mL). Yield: 2.14 g (83%). Anal. Found: C, 37.38; H, 3.14%. Calcd for [Au_2(dppe)(H_2msa)$_2$] = $C_{34}H_{34}O_8S_2P_2Au_2$: C, 37.44; H, 3.14%. IR spectrum (cm^{-1}, KBr disk): 1708, 1688 ($\nu_{C=O,COOH}$), 1436 (ν_{Ph}), 1105 (ν_{P-Ph}). ^{1}H NMR spectrum (ppm from TMS, DMSO-d_6): 7.84-7.79 (m, 8H), 7.59-7.50 (m, 12H), 3.98 (dd, 2H, J_1 = 10.1 Hz, J_2 = 4.6 Hz), 2.92-2.85 (m, 6H), 2.66 (dd, 2H, J_1 = 16.7 Hz, J_2 = 4.8 Hz). ^{31}P NMR spectrum (ppm from 80 % H_3PO_4, DMSO-d_6): 37.085.

b) [Au(dppe)$_2$]$_2$[Au_2(dppe)(*R*-Hmsa)(*S*-Hmsa)]·2EtOH ([1'])

To a white suspension containing 0.052 g (0.060 mmol) of [Au_2(dppe)Cl_2] in EtOH (5 mL) was added a colorless solution containing 0.019 g (0.13 mmol) of *rac*-H_3msa in a 0.1 M aqueous solution of NaOH (3 mL). The mixture was stirred at room temperature in the dark for 3.5 h, and added EtOH (5 mL) to it. The resulting colorless solution was evaporated to dryness.

The resulting white powder was recrystallized from a mixture of EtOH (6 mL) and H_2O (3 mL). The resulting colorless block crystals of **1'** were collected by filtration. Yield: 0.015 g (38%). Anal. Found: C, 53.67; H, 4.38%. Calcd for $[Au(dppe)_2]_2[Au_2(dppe)(Hmsa)_2]\cdot 2EtOH$ = $C_{142}H_{140}O_{10}S_2P_{10}Au_2$: C, 53.83; H, 4.45%. IR spectrum (cm^{-1}, KBr disk): 1584 ($\nu_{C=O,COO-}$), 1435 (ν_{Ph}), 1101 (ν_{P-Ph}). ^1H NMR spectrum (ppm from TMS, DMSO-d_6): 7.95 (s(br) 8H),7.52-7.49 (m, 12H), 7.38 (t, 16H), 7.35-7.30 (m, 32H), 7.24-7.20 (m, 32H), 3.90 (s(br), 2H), 2.89 (m, 8H), 2.55 (s, 16H).

II-2-3. Reactions of $[H_4\mathbf{1}]$ with Ni^{II} ions.

a) *rac*-$Na_2[Ni\{Au_2(dppe)(msa)_2\}]\cdot 3MeOH$ ($Na_2[\mathbf{2}]$).

To a white suspension containing 0.50 g (0.46 mmol) of $[H_4\mathbf{1}]$ in MeOH (50 mL) was added a 0.1 M methanolic solution of NaOH (18 mL). The mixture was stirred at room temperature in the dark for 1 h. To the resulting colorless solution was added 0.11 g (0.46 mmol) of $Ni(OAc)_2\cdot 4H_2O$ as a solid. The mixture was stirred at room temperature in the dark for 1.5 h, and the resulting green solution was evaporated to dryness. The green residue was recrystallized from MeOH (8 mL), and the resulting green block crystals of $Na_2[\mathbf{2}]$ were collected by filtration. Yield: 0.37 g (60%). Anal. Found: C, 30.87; H, 3.30%. Calcd for $Na_2[Ni\{Au_2(dppe)(msa)_2\}]\cdot 7H_2O = C_{34}H_{44}O_{15}S_2P_2Au_2NiNa_2$: C, 31.00; H, 3.37%. IR spectrum (cm^{-1}, KBr disk): 1579 ($\nu_{C=O,COO-}$), 1435, (ν_{Ph}), 1105 (ν_{P-Ph}). ESI-MS (in methanol) *m/z*: 1144.81 ($\{H[\mathbf{2}]\}^-$, 48.1%), 1164.76 ($\{HK[\mathbf{3}]\}^{2-}$, 8.5%), 1166.77 ($\{Na[\mathbf{2}]\}^-$, 100%) in negative mode, *m/z*: 1212.90 ($\{Na_3[\mathbf{2}]\}^+$, 100%) in positive mode.

b) *rac*-$[Mg(H_2O)_4(MeOH)_2][Ni\{Au_2(dppe)(msa)_2\}]\cdot 6H_2O$ ($Mg[\mathbf{2}]$).

To a white suspension containing 100 mg (0.092 mmol) of $[H_4\mathbf{1}]$ in MeOH (10 mL) was added a 0.1 M methanolic solution of NaOH (3.7 mL). The mixture was stirred at room temperature for 1 h. To the resulting colorless solution was added 23 mg (0.092 mmol) of $Ni(OAc)_2\cdot 4H_2O$ in H_2O (0.5 mL). The mixture was stirred at room temperature for 1 h, and the resulting green solution was divided into 2 parts. To this green solution was added a solution containing 21 mg (0.097 mmol) of $Mg(OAc)_2\cdot 4H_2O$ in H_2O (1 mL). The mixture was stirred for a few minutes, followed by standing at room temperature for 5 days. The resulting green plate crystals of $Mg[\mathbf{2}]$ were collected by filtration. Yield: 34 mg (54%). Anal. Found: C, 30.15; H, 3.66%. Calcd for $Mg[Ni\{Au_2(dppe)(msa)_2\}]\cdot 10H_2O = C_{34}H_{50}O_{18}S_2P_2Au_2NiMg$: C, 30.26; H, 3.73%. IR spectrum (cm^{-1}, KBr disk): 1572 ($\nu_{C=O,COO-}$), 1436, (ν_{Ph}), 1103 (ν_{P-Ph}).

c) *rac*-[Ni(H_2O)$_4$($MeOH$)$_2$][Ni{Au$_2$(dppe)(msa)$_2$}]·6H_2O (Ni[2]).

To a green solution containing 50 mg (0.038 mmol) of Na_2[**2**] in MeOH (3 mL) was added a solution containing 11 mg (0.038 mmol) of $Ni(NO_3)_2·6H_2O$ in H_2O (0.5 mL). The mixture was stirred for 1 h, followed by standing at room temperature for 3 days. The resulting green plate crystals of Ni[**2**] were collected by filtration. Yield: 25 mg (45%). IR spectrum (cm^{-1}, KBr disk): 1577 ($\nu_{C=O,COO-}$), 1436, (ν_{Ph}), 1103 (ν_{P-Ph}).

d) *rac*-[Co(H_2O)$_4$($MeOH$)$_2$][Ni{Au$_2$(dppe)(msa)$_2$}]·4H_2O (Co[2]).

To a green solution containing 50 mg (0.038 mmol) of Na_2[**2**] in MeOH (3 mL) was added a solution containing 9 mg (0.038 mmol) of $Co(OAc)_2·4H_2O$ in H_2O (0.5 mL). The mixture was stirred for a few minutes, followed by standing at room temperature for 3 days. The resulting purple plate crystals of Co[**2**] were collected by filtration. Yield: 30 mg (56%). IR spectrum (cm^{-1}, KBr disk): 1572 ($\nu_{C=O,COO-}$), 1435, (ν_{Ph}), 1104 (ν_{P-Ph}).

e) *meso*-[Ca$_2$(H_2O)$_7$][Ni$_2${Au$_2$(dppe)(msa)$_2$}$_2$]·12H_2O (Ca$_2$[3]).

To a green solution containing 20 mg (0.015 mmol) of Na_2[**2**] in MeOH (2 mL) was added a solution containing 5 mg (0.030 mmol) of $Ca(OAc)_2·H_2O$ in H_2O (0.5 mL). The mixture was stirred for a few minutes, followed by standing at room temperature for 3 weeks. The resulting green plate crystals of Ca_2[**3**] were collected by filtration. Yield: 7 mg (60%). Anal. Found: C, 30.87; H, 3.30%. Calcd for $Ca_2[Ni_2\{Au_2(dppe)(msa)_2\}_2]·17H_2O$ = $C_{68}H_{94}O_{33}S_4P_4Au_4Ni_2Ca_2$: C, 30.51; H, 3.54%. IR spectrum (cm^{-1}, KBr disk): 1577 ($\nu_{C=O,COO-}$), 1436, (ν_{Ph}), 1105 (ν_{P-Ph}).

f) [Ni$_3${Au$_2$(Hmsa)$_2$(dppe)}{Au$_2$(msa)$_2$(dppe)}($MeOH$)$_3$]·4MeOH ([4]).

To a white suspension containing 0.10 g (0.092 mmol) of [H_4**1**] in MeOH (10 mL) was added a 0.1 M methanolic solution of NaOH (1.8 mL, 0.18 mmol). The mixture was stirred at room temperature overnight. To the resulting colorless solution was added 0.034 g (0.093 mmol) of $Ni(ClO_4)_2·6H_2O$. The mixture was stirred at room temperature for a few minutes, followed by standing at room temperature for 5 days. The resulting yellow-green crystalline powder was collected by filtration. Yield: 17 mg (21%). Anal. Found: C, 31.39; H, 3.32%. Calcd for $[Ni_3\{Au_2(Hmsa)_2(dppe)\}\{Au_2(msa)_2(dppe)\}]·13H_2O$ = $C_{68}H_{88}O_{29}S_4P_4Au_4Ni_3$: C, 31.59; H, 3.43%. IR spectrum (cm^{-1}, KBr disk): 1718 ($\nu_{C=O,COOH}$), 1583 ($\nu_{C=O,COO-}$), 1437 (ν_{Ph}), 1103 (ν_{P-Ph}).

Single-crystals of [**4**] suitable for X-ray analysis were obtained as follows: To a white suspension containing 0.10 g (0.092 mmol) of [H_4**1**] in MeOH (10 mL) was added a 0.1 M methanolic solution of NaOH (2.8 mL). The mixture was stirred at room temperature for 2 h.

To the resulting colorless solution was added 0.034 g (0.092 mmol) of $Ni(ClO_4)_2 \cdot 6H_2O$. The mixture was stirred at room temperature for 2 h, and the resulting yellow-green solution was evaporated to dryness. The yellow-green residue was recrystallized from MeOH (10 mL) at room temperature, which gave yellow-green plate crystals.

Compound [**4**] was also obtained as a crystalline powder starting from Na_2[**2**] as follows: To a green solution containing 50 mg (0.038 mmol) of Na_2[**2**] in MeOH (3 mL) was added 7 mg (0.019 mmol) of $Ni(ClO_4)_2 \cdot 6H_2O$ and a 1 M methanolic solution of TfOH (76 μL). The mixture was stirred at room temperature for a few minutes, followed by standing at room temperature overnight. The resulting yellow-green crystalline powder was collected by filtration. Yield: 27 mg (54%).

II-2-4. Structural control of $Au^{I}Ni^{II}$ complexes by solution pH.

To a white suspension containing 50 g (0.046 mmol) of [H_4**1**] in MeOH (5 mL) was added a 0.1 M methanolic solution of NaOH (0.9 mL). The mixture was stirred at room temperature for 1 h. To the resulting colorless solution was added 17 mg (0.045 mmol) of $Ni(ClO_4)_2 \cdot 6H_2O$, followed by stirring at room temperature for 1.5 h to give a yellow-green solution that shows a d-d band at 672 nm in the absorption spectrum. To the resulting yellow-green solution was added a 0.1 M methanolic solution of NaOH (from 0.4 equiv to 2.0 equiv). As increasing the amount of the NaOH solution added, the solution color gradually changed from yellow-green to green, and finally, the absorption spectrum of the solution became to be superimposed with that of Na_2[**2**] on the addition of 2 equiv of NaOH. Subsequently, to the resulting green solution was added a 0.1 M methanolic solution of TfOH (from 0.4 equiv to 2.0 equiv). As increasing the amount of the TfOH solution added, the solution color gradually reverted back from green to yellow-green, and finally, the absorption spectrum of the solution became to be superimposed with the original spectrum with a d-d band at 672 nm on the addition of 2 equiv of TfOH.

II-2-5. Physical Measurements.

The IR spectra were recorded on a JASCO FT/IR-4100 infrared spectrophotometer using KBr disks at room temperature. The electronic absorption spectra in solution were recorded on a JASCO V-660 spectrophotometer at room temperature. The reflection spectra in the solid state were recorded with a JASCO V-570 UV/VIS/NIR spectrometer using a 1 cm quartz cell at room temperature. The emission and excitation spectra were recorded on a spectrofluorometer (JASCO FP-8500) at an excitation wavelength of 370 nm using a Xe lamp as the light source. The elemental analyses (C, H) were performed using a Yanako MT-5 or MT-7 recorder. The ^{1}H and ^{31}P NMR spectra in solution were measured on a JEOL EX-500 spectrometer at the probe

temperature in dimethyl sulfoxide-d_6, using tetramethylsilane (TMS) as the internal standard for ^{1}H NMR measurements and 80% H_3PO_4 as the external standard for ^{31}P NMR measurements. The X-ray fluorescence analyses were made on a HORIBA MESA-500 spectrometer. Variable temperature magnetic susceptibility measurements were made using a SQUID magnetometer MPMS XL (Quantum Design) at 0.5 T. Diamagnetic correction was determined from Pascal's constants. The electrospray ionization mass spectra (ESI-MS) were measured on a QSTAR Elite LC/MS/MS system in methanol. Thermal gravity (TG) and differential thermal analysis (DTA) measurements were measured on a SHIMADZU DTG-60 analyzer.

II-2-6. X-ray Structural Determinations.

The single crystal X-ray diffraction measurements were performed on a Rigaku RAXIS VII imaging plate and Vari-Max with graphite monochromated Mo-Kα radiation (λ = 0.71075 Å) at 200 K. The intensity data were collected by the ω-scan technique and empirically corrected for absorption. The structures of complexes were solved by direct methods using SHELXS2013.[35] The structure refinements were carried out using full matrix least-squares (SHELXL-2013). In the structure of [**1'**]·2EtOH, a half of digold(I) complex anion, a monogold(I) complex cation, and an EtOH molecule were crystallographically independent. All non-hydrogen atoms except the C and O atoms were refined anisotropically. Hydrogen atoms were included in calculated positions except that of hydroxyl group in the EtOH molecule. Two of the phenyl rings are disordered. For Na_2[**2**], two $[NiAu_2(dppe)(msa)_2]^{2-}$ anions, four Na^+ cations, and six MeOH molecules were crystallographically independent. All non-hydrogen atoms except the C atoms were refined anisotropically. Hydrogen atoms were included in calculated positions, except those of OH groups of methanol molecules. Several bond distances of two phenyl groups and some msa ligands were restrained. For Mg[**2**], one $[NiAu_2(dppe)(msa)_2]^{2-}$ anion, one $[Mg(MeOH)_2(H_2O)_4]^{2+}$ cation, and water molecules were crystallographically independent. All non-hydrogen atoms were refined anisotropically. Hydrogen atoms were included in calculated positions, except those of water molecules and OH groups of methanol molecules. The program PLATON[36] indicated a solvent accessible void space of 2938 Å^3 , corresponding to 782 electrons in a unit cell in the case of Mg[**2**]. Since the solvent molecules were grossly disordered and could not be modeled, their contribution was excluded using the subroutine SQUEEZE.[36]

For Ni[**2**], one $[NiAu_2(dppe)(msa)_2]^{2-}$ anion, one $[Ni(MeOH)_2(H_2O)_4]^{2+}$ cation, and water molecules were crystallographically independent. All non-hydrogen atoms except a part of O atoms were refined anisotropically. Hydrogen atoms were included in calculated positions

except those of water molecules. For Co[**2**], one $[NiAu_2(dppe)(msa)_2]^{2-}$ anion, one $[Co(MeOH)_2(H_2O)_4]^{2+}$ cation, and water molecules were crystallographically independent. All non-hydrogen atoms except a part of O atoms were refined anisotropically. Hydrogen atoms were included in calculated positions except those of water molecules. For Ca_2[**3**], two units of half of $[Ni_2Au_4(dppe)_2(msa)_4]^{4-}$ anions, two Ca^{2+} cations, and water molecules were crystallographically independent. All non-hydrogen atoms except O atoms were refined anisotropically. Hydrogen atoms were included in calculated positions except those of water molecules. For [**4**], one $[Ni_3Au_4(dppe)(Hmsa)_2(msa)_2(MeOH)_3]$ molecule and four solvated MeOH molecules were crystallographically independent. All non-hydrogen atoms, except for solvated MeOH molecules, were refined anisotropically. Hydrogen atoms were included in calculated positions, except those of OH groups of MeOH molecules.

II-3. Results and Discussion.

II-3-1. Synthesis and Characterization of Complexes with dppe and msa

a) Au^I Metalloligands

Synthesis and Characterization of [Au_2(dppe)(H_2msa-*S*)$_2$] ([$H_4$1**]).**

The 1:2 reaction of [Au_2(dppe)Cl_2] with *rac*-H_3msa in EtOH/H_2O in the presence of 2 equiv of NaOH gave a white suspension, from which a white powder was obtained by filtration. The resulting crude powder was washed with EtOH and $CHCl_3$ in order to remove NaCl and unreacted raw materials, giving a pure sample of [H_4**1**] in a high yield. The elemental analytical data of [H_4**1**] were in good agreement with the formula of a 1:2 adduct of $\{Au_2(dppe)\}^{2+}$ and H_2msa^- without any counter ions. In addition, the IR spectrum of [H_4**1**] gave a strong ν_{CO} band at around 1708 and 1688 cm^{-1},[37] indicating the presence of two protonated carboxy groups in the structure (Figure 2-1). The ^{1}H NMR spectrum of [H_4**1**] in DMSO-d_6 showed a multiplet signal at δ 7.84-7.79, a multiplet signal at δ 7.59-7.50, a double doublet signal at δ 3.98 (J_1 = 12.3 Hz, J_2 = 4.6 Hz), a multiplet signal at δ 2.92-2.85, a double doublet signal at δ 2.66 (J_1 = 16.7 Hz, J_2 = 4.8 Hz) in an integral intensity ratio of 8:12:2:6:2 (Figure 2-2 and Table 2-1). Among the proton signals, the fourth signal (δ 2.92-2.85) can be considered as the overlapping signal of double doublet (δ 2.88, J_1 = 16.8 Hz, J_2 = 10.4 Hz) and singlet (δ 2.87) signals in an integral intensity ratio of 2:4. The assignment of these ^{1}H NMR signals was summarized in Table 2-1. The multiplet signals observed in the aromatic region and the overlapped singlet signal in the aliphatic region were assigned to phenyl and methylene protons of dppe, respectively. Two sharp double doublet and overlapping double doublet signals observed in the aliphatic region were assigned to two methylene and one methine protons of msa, respectively. This characterization and the integral intensity ratio of these signals imply the presence of dppe and msa in a 1:2 ratio in [H_4**1**]. The ^{31}P NMR spectrum in DMSO-d_6 showed a singlet signal at δ 37.1 (Figure 2-3). To sum up these information, [H_4**1**] is characterized to a C_2 symmetrical neutral linear digold(I) complex, [Au_2(dppe)(H_2msa-*S*)$_2$], in which two terminal H_2msa^- ligands are spanned by $\{Au_2(dppe)\}^{2+}$ moiety (Scheme 2-1). Considering the chirality of two terminal H_2msa^- ligands (*R* or *S*), two diastereomers, the racemic (*RR*/*SS*) and the meso (*RS*) forms, are possible for [H_4**1**]. However, the ^{1}H and ^{31}P NMR spectroscopy showed only a single set of signals for [H_4**1**], which implies that the selective formation of one of the two isomers or the rapid structural conversion between the two isomers occurs in solution.

Synthesis and Characterization of $[Au(dppe)_2]_2[Au_2(dppe)(Hmsa\text{-}S)_2]\cdot 2EtOH$ ([1']).

In the course of trials to obtain single-crystal of $[H_4\mathbf{1}]$, it was found that the reaction with an excess amount of base gives single-crystals containing the digold(I) complex. The 1:2 reaction of $[Au_2(dppe)Cl_2]$ with *rac*-H_3msa in EtOH/H_2O in the presence of 5 equiv of NaOH gave a colorless solution, from which a white powder was obtained by concentrating the solution to dryness. The resulting crude powder was recrystallized from EtOH/H_2O, which gave colorless crystals of [**1'**]. Single-crystal X-ray analysis indicated that crystal [**1'**] contains not only the expected digold(I) complex anion, $[Au_2(dppe)(Hmsa)_2]^{2-}$, but also a monogold(I) complex cation, $[Au(dppe)_2]^+$. The elemental analytical data of [**1'**] were in a good agreement with the formula of a 1:2 adduct of $[Au_2(dppe)(Hmsa)_2]^{2-}$ and $[Au(dppe)_2]^+$ without any counter ions. In addition, the IR spectrum of [**1'**] gave a strong ν_{CO} band at around 1584 cm^{-1} with a weak shoulder at around 1700 cm^{-1}, indicating the presence of both deprotonated and protonated carboxy groups in the structure (Figure 2-1). Moreover, an absorption band corresponding to ν_{Ph} observed at around 1435 cm^{-1} in the IR spectrum is more intense rather than that of $[H_4\mathbf{1}]$, which supports the presence of a larger amount of dppe ligands in the crystal [**1'**]. The ^{1}H NMR spectrum of [**1'**] in DMSO-d_6 showed two sets of intensive signals each corresponding to the C_2-symmetrical $[Au_2(dppe)(Hmsa)_2]^{2-}$ and D_2-symmetrical $[Au(dppe)_2]^+$, besides a single set of weak msa signals (Figure 2-2). The cationic part of $[Au(dppe)_2]^+$ was assumed to be formed by the decomposition of the precursor digold(I) material $[Au_2(dppe)Cl_2]$ or the digold metalloligand $[H_4\mathbf{1}]$ (Scheme 2-2). The hydrophobicity of the cations may support the crystallization of the digold metalloligand in [**1'**]. Under UV light irradiation at room temperature, the solid sample of [**1'**] showed an orange emission. In the emission spectrum, [**1'**] showed a broad band centered at 596 nm (Figure 2-5). The emission spectrum of [**1'**] was similar to that of $[Au(dppe)_2]PF_6$ (λ_{max} = 595 nm).[19] Therefore, the emission was assigned to a LMCT transition from π*(Ph-Ph) to Au(d)-P(p), involved with excimer of phenyl groups in $[Au(dppe)_2]^+$.

Crystal Structure of $[Au(dppe)_2]_2[Au_2(dppe)(Hmsa)_2]\cdot 2EtOH$ ([1']).

The molecular structure is shown in Figure 2-6. The crystallographic data are summarized in Table 2-2, and the selected bond distances and angles are listed in Table 2-3. Crystal [**1'**]·2EtOH contains one monogold(I) complex cation, $[Au(dppe)_2]^+$, one-half of digold(I) complex anion, $[Au_2(dppe)(Hmsa)]^{2-}$, and a solvated EtOH molecule in the asymmetric unit. The complex cation comprises of two dppe and a Au^I center (av. Au–P = 2.40 Å). Two dppe ligands act as a P,P-chelating ligand for the Au^I center, giving a tetrahedral structure of $[Au(dppe)_2]^+$. The complex anion comprises of one *R*-$Hmsa^{2-}$, one *S*-$Hmsa^{2-}$, and one

$\{Au_2(dppe)\}^{2+}$ (Au–P = 2.27 Å, Au–S = 2.29 Å), forming a linear dinuclear structure of $[Au_2(dppe)(R\text{-Hmsa-}S)(S\text{-Hmsa-}S)]^{2-}$, in which the *R*-Hmsa^{2-} and *S*-Hmsa^{2-} ligands are bridged by a $[Au_2(dppe)]^{2+}$ moiety through S atoms. In crystal, each complex anion connects two neighboring complex anions through CH···OOC interactions (average C···O = 3.46 Å). Moreover the complex anion further contacts with two complex cations through CH···π interactions and CH···OOC interactions (average C···O = 3.35 Å) to form a 3D supramolecular structure (Figure 2-7).

Structural Conversion of Au^I_2 Metalloligands by base.

In order to investigate the unexpected formation of $[Au(dppe)_2]^+$ in basic conditions in detail, the reactivity of [H_4**1**] with base was investigated. To a suspension containing [H_4**1**] in EtOH was added 3 equiv of aqueous solution of KOH. After 6 days, the solution was dried up, and the ^{1}H NMR spectrum was measured in DMSO-d_6. As a result, two sets of signals, which are corresponding to the starting digold(I) metalloligand ([H_4**1**]) and $[Au(dppe)_2]^+$, were observed (Figure 2-4). However, the signals of the digold(I) metalloligand were slightly broaden, which suggests the coexistence of other partially-decomposed species that are quickly interconvertible with [H_4**1**]. From the NMR study, it was revealed that base promotes the decomposision of the digold(I) metalloligand [H_4**1**] and formation of $[Au(dppe)_2]^+$ cations.

b) Au^INi^{II} Metal Complexes

Absorption Spectrum of Reaction Solutions Containing Au^I_2 Complexes and Ni^{II}.

The 1:1 reaction of [H_4**1**] with $Ni(OAc)_2 \cdot 4H_2O$ in the presence of 4 molar equiv of NaOH gave a green solution. The absorption spectrum of the green solution showed two broad bands at around 650 and 1140 nm. (Figure 2-8). These bands are assignable to $^3T_{1g} \leftarrow {}^3A_{2g}$ and $^3T_{2g} \leftarrow {}^3A_{2g}$ transitions of octahedral d^8 Ni^{II} center respectively,[12a, 33c] which suggests that the Ni^{II} center is coordinated by the digold(I) metalloligand through S and O atoms of msa moieties to have a O_4S_2 octahedral geometry.

***rac*-Na_2[Ni{Au_2(dppe)(msa)$_2$}]·3MeOH (Na_2[2]).**

The slow evaporation of the green solution containing [H_4**1**], $Ni(OAc)_2 \cdot 4H_2O$, and NaOH in a 1:1:4 ratio gave green crystals with a block-like shape (Na_2[**2**]) in a moderate yield (60%). In the IR spectrum, Na_2[**2**] showed a strong ν_{CO} band at 1579 cm^{-1}, which indicates the presence of msa including deprotonated carboxy groups (Figure 2-9). Elemental analysis data were in good agreement with the formula of Na_2[Ni{Au_2(dppe)(msa)$_2$}] with 7 water molecules, and the fluorescent X-ray analysis showed that Na_2[**2**] contains Ni and Au atoms in a 1:2 ratio. The

diffuse reflection spectrum of Na_2[**2**] in the solid state showed a near IR band at 1041 nm and a visible band at 651 nm, which are assignable to d-d transitions (Figure 2-10 and Table 2-4). As shown in Figure 2-11, the electronic absorption spectrum of Na_2[**2**] in MeOH showed a near IR band at 1135 nm and a visible band at 651 nm. This spectral pattern is identically the same as that of the reaction solution (Figure 2-8). These results are consistent with the trinuclear structure of $[Ni\{Au_2(dppe)(msa)_2\}]^{2-}$, in which the $[Au_2(dppe)(msa)_2]^{4-}$ metalloligand chelates a Ni^{II} center, as observed in the single-crystal X-ray crystallography (see below). The overall pattern of the absorption spectra are similar to that of a relating trinuclear $Au^I_2Ni^{II}$ complex with D-penicillaminate (D-pen) $[\{Au_2(dppm)\}\{Ni(D\text{-pen-}N,O,S)_2\}]$, which possesses an octahedral $\{Ni(D\text{-pen-}N,O,S)_2\}^{2-}$ unit,[12a] but the absorption energy of each band is red shifted due to the decrease of ligand field splitting energy from ($N_2O_2S_2$) to (O_4S_2) donor sets. The retention of the trinuclear structure of Na_2[**2**] in MeOH was confirmed by the similarity of the spectral patterns in the UV-Vis-NIR region between the methanolic solution and the solid state.

X-ray structural analysis of Na_2[**2**] showed the presence of two crystallographically independent trinuclear complex anions, $[Ni\{Au_2(dppe)(msa)_2\}]^{2-}$, four Na^+ ions, and MeOH molecules in the asymmetric unit. The structure is illustrated in Figure 2-13. The crystallographic data are summarized in Table 2-6, and selected bond distances and angles are listed in Table 2-7. Complex Na_2[**2**] forms a trinuclear complex anion composed of an Au^I_2 metalloligand $[Au_2(dppe)(msa)_2]^{4-}$ and a Ni^{II} ion. In the trinuclear structure, Ni^{II} ion is coordinated by two msa moieties from the Au^I_2 metalloligand in a hexadentate-O_4S_2 mode, to form an octahedral O_4S_2 coordination environment of the Ni^{II} center. The two msa moieties possess the same absolute configuration, that is, there are only *SS* and *RR* isomers in the crystal. In the molecular structure of msa, there are two kinds of carboxy groups. In order to distinguish the two carboxyl groups of msa, O atom of carboxyl group located in an alpha-position on thiol group was defined as O_α and that located in a beta-position was defined as O_β (Chart 2-4). For the octahedral $[Ni(R\text{-msa})_2]^{4-}$ and $[Ni(S\text{-msa})_2]^{4-}$ units, three structural isomers (*trans* O_α, *trans* O_β, and *trans* S) are possible (Chart 2-5). In $[\mathbf{2}]^{2-}$, two S and two O_β donor atoms make a *cis*-S, *cis*-O_β type square-plane and an two O_α atoms occupy axial positions to form the *trans* O_α isomer. The two bridging S atoms have the *R* and *S* configurations for the *SS* and *RR* isomers, respectively. The averaged bond distances of Ni–S, Ni–O_α, and Ni–O_β bonds are 2.42 Å, 2.07 Å, and 2.05 Å, respectively, and those of Au–S and Au–P bonds are 2.31 and 2.28 Å, respectively. In Na_2[**2**], the averaged intramolecular separation between two Au^I atoms is 2.96 Å, suggestive of the presence of an aurophilic interaction,[16] which has commonly been observed for other gold(I) species with a $\{Au_2(dppe)_2\}^{2+}$ moiety.[16] Na^+ ions are coordinated by carboxyl groups of msa units and MeOH molecules, with the bond distances of 2.28-2.64 Å.

In a packing structure, a 2D layer structure is constructed by the infinite connection of neighboring complex anions through C–H···π interactions between phenyl groups. In the 2D structure, msa moieties are oriented toward outside of the layer, forming two hydrophilic surfaces (Figure 2-14). Na^+ cations exist between two layers through the coordination with the carboxyl groups of complex anions. As a result, the 2D layers are stacked to form 3D structure with alternate hydrophobic and hydrophilic layers.

***rac*-[Mg(H$_2$O)$_4$(MeOH)$_2$][Ni{Au$_2$(dppe)(msa)$_2$}] (Mg[2]).**

In order to check the effect of the counter cation on the product, the cation exchange of Na_2[**2**] was carried out. To the green reaction solution containing Na_2[**2**] was added to an aqueous solution of $Mg(OAc)_2{\cdot}4H_2O$, from which green crystals with a plate-like shape (Mg[**2**]) were isolated. The IR spectrum of Mg[**2**] was very similar to that of Na_2[**2**] in the whole region, showing a strong ν_{CO} band at 1572 cm^{-1} (Figure 2-9). Elemental analysis data were in good agreement with the formula of $[Mg(H_2O)_6][Ni\{Au_2(dppe)(msa)_2\}]$ with 5 water molecules, and the fluorescent X-ray analysis showed that Mg[**2**] contains Ni and Au atoms in a 1:2 ratio. The diffuse reflection spectrum of Mg[**2**] in the solid state was also quite similar to that of Na_2[**2**], giving a near IR band at 1182 nm and a visible band at 653 nm (Figure 2-10 and Table 2-4). These results are consistent with the formation of a similar trinuclear structure of $[Ni\{Au_2(dppe)(msa)_2\}]^{2-}$ as found in Na_2[**2**], which is further confirmed by single-crystal X-ray crystallography.

X-ray structural analysis of Mg[**2**] showed the presence of a crystallographically independent trinuclear complex anion, $[NiAu_2(dppe)(msa)_2]^{2-}$, one octahedral *cis*-$[Mg(H_2O)_4(MeOH)_2]^{2+}$ cation, and solvated water molecules in the asymmetric unit. The structure is shown in Figure 2-15. The crystallographic data are summarized in Table 2-8, and selected bond distances and angles are listed in Table 2-9. The averaged bond distances of Ni–S, Ni–O$_\alpha$, and Ni–O$_\beta$ bonds are 2.40 Å, 2.03 Å, and 2.06 Å, respectively, and those of Au–S and Au–P bonds are 2.31 and 2.26 Å, respectively. In Mg[**2**], the averaged intramolecular separation between two Au^I atoms is 2.93 Å, suggestive of the presence of an aurophilic interaction. The trinuclear complex anoion in Mg[**2**] is composed of a Au^I_2 metalloligand $[Au_2(dppe)(msa)_2]^{4-}$ and a Ni^{II} ion. However, in the case of Mg[**2**], Mg^{2+} ion is not directly bound to carboxylate groups, but coordinated by six solvent molecules, which is clearly different from the case of Na_2[**2**].

In the packing structure in Mg[**2**], each complex-anion contacts with four neighboring complex-anions though intermolecular C–H···π interactions between phenyl groups, constructing a 2D sheet-like structure (Figure 2-15). The 2D sheets are parallel arranged to form

hydrophilic layers, the surfaces of which are covered by carboxyl groups of msa^{3-}. The hydrophilic layers accommodate $[Mg(H_2O)_4(MeOH)_2]^{2+}$ cations, each of which forms multiple O-H···O hydrogen bonds (av. O···O = 2.78 Å) with msa^{3-} ligands from three different complex-anions.

***rac*-[M(H$_2$O)$_4$(MeOH)$_2$][Ni{Au$_2$(dppe)(msa)$_2$}] (M[2], M = Ni^{2+}, Co^{2+}).**

Treatment of Na_2[**2**] with $Ni(OAc)_2{\cdot}4H_2O$ and $Co(OAc)_2{\cdot}4H_2O$ in MeOH/H_2O gave green plate crystals (Ni[**2**]) and purple plate crystals (Co[**2**]), respectively. The IR spectra of Ni[**2**] and Co[**2**] were very similar to that of Na_2[**2**] in the whole region, showing a strong ν_{CO} band at 1577 cm^{-1} and 1572 cm^{-1}, respectively (Figure 2-9). Elemental analysis data were in good agreement with the formula of $[M(H_2O)_6][Ni\{Au_2(dppe)(msa)_2\}]$ (M = Ni^{II}, Co^{II}), and fluorescent X-ray analysis showed that Ni[**2**] contains Ni and Au atoms in a 2:2 ratio and Co[**2**] contains Ni, Co and Au atoms in a 1:1:2 ratio. The diffuse reflection spectrum of Ni[**2**] in the solid state was also quite similar to that of Na_2[**2**], giving a near IR band at 1184 nm and a visible band at 649 nm, while the spectrum of Co[**2**] showed a near IR band at 1161 nm and two visible bands at 642 and 509 nm (Figure 2-10 and Table 2-4). These results are consistent with the formation of a similar trinuclear structure of $[Ni\{Au_2(dppe)(msa)_2\}]^{2-}$ as found in Na_2[**2**], which is further confirmed by single-crystal X-ray crystallography.

Crystals Ni[**2**] and Co[**2**] are isomorphic with Mg[**2**]. The structures are shown in Figure 2-16. The crystallographic data are summarized in Tables 2-10 and 2-12, and selected bond distances and angles are listed in Tables 2-11 and 2-13. In Ni[**2**], The averaged bond distances of Ni–S, Ni–O$_\alpha$, and Ni–O$_\beta$ bonds are 2.40 Å, 2.03 Å, and 2.07 Å, respectively, and those of Au–S and Au–P bonds are 2.32 and 2.27 Å, respectively. The averaged intramolecular separation between two Au^I atoms is 2.95 Å, suggestive of the presence of an aurophilic interaction. In Co[**2**], The averaged bond distances of Ni–S, Ni–O$_\alpha$, and Ni–O$_\beta$ bonds are 2.39 Å, 2.07 Å, and 2.07 Å, respectively, and those of Au–S and Au–P bonds are 2.32 and 2.27 Å, respectively. The averaged intramolecular separation between two Au^I atoms is 2.95 Å, suggestive of the presence of an aurophilic interaction.

***meso*-[Ca$_2$(H$_2$O)$_7$][Ni$_2${Au$_2$(dppe)(msa)$_2$}$_2$] (Ca$_2$[3]).**

Treatment of Na_2[**2**] with $Ca(OAc)_2$ in MeOH/H_2O gave green plate crystals (Ca_2[**3**]). The IR spectrum of Ca_2[**3**] gave a strong ν_{CO} band at 1577 cm^{-1}, indicating the presence of msa including deprotonated carboxy groups (Figure 2-9). Elemental analysis data were in good agreement with the 1:1:1 adduct of Ca^{2+}, Ni^{2+} and $[Au_2(dppe)(msa)_2]^{4-}$, and fluorescent X-ray analysis showed that Ca_2[**3**] contains Ni and Au atoms in a 1:2 ratio. The diffuse reflection

spectrum of Ca_2[**3**] in the solid state was similar to that of Na_2[**2**], giving a near IR band at 1175 nm and a visible band at 665 nm (Figure 2-10 and Table 2-4). These spectral features are consistent with the result of X-ray analysis, which showed an anionic hexanuclear structure of $[Ni_2\{Au_2(dppe)(msa)_2\}_2]^{4-}$, in which two octahedral Ni^{II} ions are bridged by two $[Au_2(dppe)(msa)_2]^{4-}$ units (see below).

X-ray structural analysis of Ca_2[**3**] showed the presence of a hexanuclear complex anion, $[Ni_2Au_4(dppe)_2(msa)_4]^{4-}$, two Ca^{2+} cations, and solvated water molecules in the asymmetric unit. The structure is shown in Figure 2-17. The crystallographic data are summarized in Table 2-14, and selected bond distances and angles are listed in Table 2-15. The hexanuclear complex [**3**]$^{4-}$ is composed of two Au^I_2 metalloligands, $[Au_2(dppe)(msa)_2]^{4-}$, and two Ni^{II} ions. Each Ni^{II} ions is coordinated by two msa ligands from different metalloligands to form an octahedral O_4S_2 coordination environment of the Ni^{II} center, while the metalloligands bridges two Ni^{II} centers in a bis(tridentate-*O*,*O*',*S*) mode. Two msa units that coordinate to one Ni^{II} ion possess the same absolute configuration, while the two msa units in the Au^I_2 metalloligand possess opposite absolute configurations. As a result, the *SSRR*-type meso structure is formed in [**3**]$^{4-}$. Each Ni^{II} center has a *cis*-S, *cis*-O_β and *trans*-O_α configuration as found in [**2**]$^{2-}$. The two bridging S atoms that bind to one Ni^{II} center have *R* and *S* configurations for the *RR* and *SS* isomers of $[Ni(msa)_2]^{4-}$ moieties, respectively. The averaged bond distances of Ni–S, Ni–O_α, and Ni–O_β bonds are 2.40 Å, 2.05 Å, and 2.08 Å, respectively, and those of Au–S and Au–P are 2.30 and 2.25 Å, respectively. In [**3**]$^{4-}$, the average intramolecular separation between two Au^I atoms is 3.12 Å, suggestive of the presence of an aurophilic interaction. Ca^{2+} ions are coordinated by two carboxyl groups of msa units and four H_2O molecules, with the bond distances of 2.00-2.59 Å.

In a packing structure, a 2D layer structure is constructed by the infinite connection of neighboring complex anions through C–H···π interactions between phenyl groups. In this 2D structure, msa moieties are oriented toward outside of the layer, forming two hydrophilic surfaces (Figure 2-17). Ca^{2+} cations are existed between two layers through the coordination with carboxyl groups of complex anions and hexanuclear complexes formed 1D infinite chine. Moreover, this 1D chines connected through double hydrogen bonds with coordinated water molecules and carboxylate groups (average O···O = 2.79 Å). As a result, the 2D layers are stacked to form a 3D structure with alternate hydrophobic and hydrophilic layers.

$[Ni_3\{Au_2(dppe)(Hmsa)_2\}\{Au_2(dppe)(msa)_2\}(MeOH)_3]\cdot 4MeOH$ ([4]).

Treatment of [H_4**1**] with 1 molar equiv of $Ni(ClO_4)_2\cdot 6H_2O$ in MeOH, followed by the addition of 3 molar equiv of NaOH, gave a yellowish green solution, from which yellowish

green crystals with a plate-like shape ([**4**]) were obtained. In the IR spectrum, [**4**] gave a strong ν_{CO} band at 1583 cm^{-1} and a weak ν_{CO} band at 1717 cm^{-1}, indicating the presence of both deprotonated and protonated carboxy groups (Figure 2-9). X-ray fluorescence analyses showed that [**4**] contains Ni and Au atoms in a 3:4 ratio. These spectral features are consistent with the result of single-crystal X-ray crystallography, which showed a heptanuclear structure of $[Ni_3\{Au_2(dppe)(Hmsa)_2\}\{Au_2(dppe)(msa)_2\}]$, in which $[Au_2(dppe)(msa)_2]^{4-}$ and $[Au_2(dppe)(Hmsa)_2]^{2-}$ metalloligands each bridges three octahedral Ni^{II} ions (see below).

The structure of [**4**] was established by single-crystal X-ray analysis, which revealed the presence of a neutral complex molecule and MeOH molecules of crystallization in the asymmetric unit, with the lack of any counter ions. The structure is shown in Figure 2-18 and Chart 2-6. The crystallographic data are summarized in Table 2-16, and selected bond distances and angles are listed in Table 2-17. As shown in Figure 2-18, [**4**] consists of one fully deprotonated $[Au_2(dppe)(RR \text{ or } SS\text{-msa})_2]^{4-}$ ($[\mathbf{1}]^{4-}$), one semi-deprotonated $[Au_2(dppe)(RS\text{-Hmsa})_2]^{2-}$ ($[H_2\mathbf{1}]^{2-}$), three Ni^{II} atoms, and three MeOH molecules. The fully deprotonated $[\mathbf{1}]^{4-}$ chelates to Ni1 atom in a pentadentate-O_3S_2 mode (av. Ni–S = 2.388 Å, Ni–O = 2.053 Å) so as to have a pendent deprotonated carboxyl arm. On the other hand, the semi-deprotonated $[H_2\mathbf{1}]^{2-}$ chelates to Ni2 atom in a tetradentate-O_2S_2 mode (av. Ni–S = 2.379 Å, Ni–O = 2.104 Å) so as to have two protonated carboxyl arms. the remaining coordination site of Ni1 center is occupied by a carboxyl O atom from $[H_2\mathbf{1}]^{2-}$ (Ni–O = 2.059(6) Å), while the remaining two coordination sites of Ni2 center are filled with the pendent carboxyl arm (Ni–O = 2.024(6) Å) and the thiolato S atom of $[\mathbf{1}]^{4-}$ (Ni–S = 2.466(3) Å). In addition, two carboxyl groups bound to Ni1 center and one carboxyl group bound to Ni2 center coordinate to Ni3 atom (av. Ni–O = 2.049 Å), together with three MeOH molecules (av. Ni–O = 2.051 Å), completing a unique $Au^{I}_4Ni^{II}_3$ heptanuclear structure in $[Ni_3\{Au_2(dppe)(Hmsa)_2\}\{Au_2(dppe)(msa)_2\}(MeOH)_3]$ that possesses three Ni^{II} centers with *cis*-O_4S_2, *mer*-O_3S_3, and *fac*-$O_3O'_3$ octahedral geometries. The two msa^{3-} ligands bridge three metal centers (one Au^{I} and two Ni^{II}) in a μ_3-κ^1S:κ^3O,O,S:κ^1O mode and four metal centers (one Au^{I} and three Ni^{II}) in a μ_4-κ^1S:κ^2O,S:κ^2O,S:κ^1O mode, while the two $Hmsa^{2-}$ ligands bridge two metal centers (one Au^{I} and one Ni^{II}) in a μ_2-κ^1S:κ^2O,S mode and four metal centers (one Au^{I} and three Ni^{II}) in a μ_4-κ^1S:κ^2O,S:κ^1O:κ^1O mode. It may be interesting to note that in [**4**], the msa^{3-} and $Hmsa^{2-}$ ligands adopts quite versatile coordination modes.

In the crystal packing in [**4**], the heptanuclear complex molecules are connected with each other through intermolecular CH···π (av. C···C = 3.717 Å) and OH···O hydrogen-bonding (av. O···O = 2.539 Å) interactions, constructing a 3D network structure (Figure 2-19).

II-3-2. Structural Control of $Au^{I}Ni^{II}$ Complexes by Counter Cations.

The ESI-mass spectrum of Na_2[**2**] showed three dominant signals corresponding to $\{HNiAu_2(dppe)(msa)_2\}^-$ (m/z = 1144.81), $\{NaNiAu_2(dppe)(msa)_2\}^-$ (m/z = 1166.94), and $\{HKNi_2Au_4(dppe)_2(msa)_4\}^{2-}$ (m/z = 1164.94) (Figure 2-12). This result suggests that the trinuclear $Au^{I}_2Ni^{II}$ species of $[NiAu_2(dppe)(msa)_2]^{2-}$ ([**2**]$^{2-}$) and the hexanuclear $Au^{I}_4Ni^{II}_2$ species of $[Ni_2Au_4(dppe)_2(msa)_4]^{4-}$ ([**3**]$^{4-}$) are in an equilibrium in solution. In both [**2**]$^{2-}$ and [**3**]$^{4-}$, every Ni^{II} centers are coordinated by two *R*-msa^{3-} or by two *S*-msa^{3-}, to form the racemic $[Ni(msa)_2]^{4-}$ unit. However, the stereostructure of the digold(I) metalloligand in these complexes are clearly different from each other. In [**2**]$^{2-}$, the digold(I) metalloligand is the racemic form of [$\mathbf{1}_{RR}$]$^{4-}$ or [$\mathbf{1}_{SS}$]$^{4-}$, and coordinates to one Ni^{II} center in a hexadentate-O_4S_2 coordination mode. In contrast, in [**3**]$^{4-}$, the digold(I) metalloligand is the meso form of [$\mathbf{1}_{RS}$]$^{4-}$, and bridges two Ni^{II} centers with a bis(bidentate-O_2S) coordination mode. Therefore, it was assumed that the interconversion between [**2**]$^{2-}$ and [**3**]$^{4-}$ occurred through the rearrangement of the Au–P and/or Au–S coordination bonds in the digold(I) metalloligands. Similar structural interconversion between trinuclear and hexanuclear structures and the rearrangement of the digold(I) metalloligand have been reported in the relating Au^{I}-Co^{III} system based on $[Au_2(dppe)(pen)_2]^{2-}$.[14]

In this work, the formation of the two $Au^{I}Ni^{II}$ complexes, [**2**]$^{2-}$ and [**3**]$^{4-}$, is successfully controlled in the crystallization process by changing the counter cations. In the case of comparatively small cations (Mg^{2+}, Ni^{2+}, Co^{2+}), the trinuclear complex [**2**]$^{2-}$ was selectively crystallized. In contrast, the bigger cation (Ca^{2+}) led to the crystallization of the hexanuclear complex [**3**]$^{4-}$. For the smaller cations, the cations are fully coordinated by solvents, like $[M(H_2O)_4(MeOH)_2]$, and are accommodated in the hydrophilic spaces of the 2D-layered structure of [**2**]$^{2-}$ through hydrogen bonds. If the bigger $[Ca(solvent)_n]^{2+}$ cations are accommodated in the hydrophilic spaces, the distance between the trinuclear complexes would be getting wider and lead to cleavage of C–H···π interaction. Meanwhile, the larger Ca^{2+} forms double hydrogen bonds through coordination solvent with carboxyl groups. But, if the smaller $[Mg(solvent)_n]^{2+}$ cations are accommodated instead of Ca^{2+} cations, double hydrogen bonds cannot be reached. Therefore, it was assumed that the disadvantageous crystallization of $[Ca(solvent)_n]$[**2**] and $[Mg(solvent)_n]_2$[**3**].

II-3-3. Structural Control of $Au^{I}Ni^{II}$ Complexes by Solution pH.

When [H_4**1**] was reacted with Ni^{II} ion under basic conditions, trinuclear $Au^{I}_2Ni^{II}$ ([**2**]$^{2-}$) and hexanuclear $Au^{I}_4Ni^{II}_2$ complexes ([**3**]$^{4-}$) were isolated. However, similar reaction in an acidic condition gave the heptanuclear $Au^{I}_4Ni^{II}_3$ complex [**4**]. These results suggested that the

pH of the reaction solution is important for the product. To elucidate the pH dependence of this Au^{I}-Ni^{II} system, acid/base titration experiments were carried out. First, a total of 2 equivalent of NaOH was slowly added to an acidic yellowish green solution, which is prepared by mixing of [H_4**1**], NaOH, and $Ni(ClO_4)_2$ in a 1:2:1 ratio in MeOH. The absorption spectrum of the initial yellowish green solution showed a d-d band at around 672 nm (Figure 2-20). According as adding NaOH, the band shifts to a shorter wavelength, and finally the absorption spectrum of the reaction mixture is superimposed with that of Na_2[**2**] when 2 equiv of NaOH was added. Next, 2 equiv of TfOH was added to the solution. According as adding TfOH, the d-d band shifts to a longer wavelength, and finally, the d-d band reaches to 674 nm and the spectrum almost corresponds with that of the initial yellowish green solution. These results indicates the reversible structural change depend on the solution pH. The pH dependent structural conversion was reasonably understood by the following explanation. In a basic condition, msa moieties in the metalloligand fully deprotonated and coordinate to the Ni^{II} center with a tridentate-*O*,*O'*,*S* coordination mode. In contrast, in an acidic condition, msa moieties partly are protonated and some of carboxy groups cannot participate to the coordination to the Ni^{II} center, and therefore, Ni^{II} ions become unsaturated. In order to fill the unsaturated coordination cites, μ_2-thiolato groups of another trinuclear $Ni^{II}Au^{I}_2$ complex further coordinate to the Ni^{II} center to form higher nuclearity structure with μ_3-bridging S atoms.

Based on the structural determination, it was evidenced that the octahedral Ni^{II} center in [**2**]$^{2-}$ is not converted to a square-planar Ni^{II} center with retention of the $Au^{I}_2Ni^{II}$ trinuclear structure under acidic conditions, but a drastic structural transformation from its $Au^{I}_2Ni^{II}$ trinuclear to the $Au^{I}_4Ni^{II}_3$ heptanuclear structure is induced with retention of the octahedral Ni^{II} center. This is in sharp contrast to the previously reported $Au^{I}_2Ni^{II}_2$ coordination system with D-penicillaminate, in which the octahedral-to-square-planar conversion of Ni^{II} centers occurs under acidic conditions with retention of its tetranuclear structure.[23] It is apparent that the ligand field provided by two bidentate-*O*,*S* msa ligands is appreciably weaker than the one provided by two bidentate-*N*,*S* pen ligands. Thus, the weakness of the ligand field is most likely responsible for the present result, considering that a square-planar metal center is commonly stabilized by a strong ligand field.[38]

To evaluate the magnetic properties of [**2**]$^{2-}$ and [**4**], the temperature dependence of the magnetic susceptibilities were measured for polycrystalline samples of Mg[**2**] and [**4**] in the temperature range of 2 K to 300 K (Figure 2-21). For Mg[**2**], the plot of $\chi_M T$ versus T decreases only slightly from 1.27 cm^3 K mol^{-1} at 300 K to 1.17 cm^3 K mol^{-1} at 7 K, and then decreases sharply to 0.96 cm^3 K mol^{-1} at 2 K on lowering the temperature. Since the value at 300 K is close to the spin-only value of 1.00 cm^3 K mol^{-1} for an octahedral Ni^{II} center with a d^8 electronic

configuration, it is assumed that no significant intermolecular magnetic interactions exist between Ni^{II} centers in Mg[**2**]. On the other hand, the plot of $\chi_M T$ versus T for [**4**] increases gradually from 3.77 cm^3 K mol^{-1} at 120 K, which is appreciably larger than the spin-only value of 3.00 cm^3 K mol^{-1} for the magnetically dilute three Ni^{II} centers. The peak value is 4.04 cm^3 K mol^{-1} at 22 K, and then the value decreases sharply to 2.64 cm^3 K mol^{-1} at 2 K on lowering the temperature. The sharp decrease of the $\chi_M T$ values for each of Mg[**2**] and [**4**] at low temperature (< 5 K) is due to the zero-field splitting of S = 1 state of the Ni^{II} center. This magnetic feature is suggestive of the presence of intramolecular ferromagnetic interactions between three Ni^{II} centers in [**4**]. Weiss temperature for [**4**] was estimated to be θ = +1.5 K, which is also consistent with the presence of weak ferromagnetic interactions.

II-4. Conclusion.

In this chapter, a successful example of the improvement of the crystallinity of coordination compounds of H_3msa by the introduction of gold(I)-phenylphosphine complex was described.

First, the new linear digold(I) complex, $[Au_2(dppe)(H_2msa\text{-}S)_2]$ ($[H_4\mathbf{1}]$), in which two H_2msa^- ligands are spanned by a $\{Au_2(dppe)\}^{2+}$ moiety through S atoms, was synthesized by the 1:2 reaction of $[Au_2(dppe)Cl_2]$ with H_3msa in the presence of NaOH. This complex was fully characterized by elemental analyses, together with ^1H NMR and IR spectroscopies. The digold(I) complex, $[Au_2(dppe)(msa)_2]^{4-}$, was partially decomposed to give the monogold(I) complex-cation, $[Au(dppe)]^+$ in basic conditions. The monogold(I) complex cation was co-crystallized with the digold(I) complex-anion, $[Au_2(dppe)(Hmsa)_2]^{2-}$, and its molecular structure was successfully confirmed by single-crystal X-ray analysis.

Second, the coordination behavior of $[H_4\mathbf{1}]$ toword Ni^{II} ions was investigated. As a result, the three Au^I-Ni^{II} complexes ($[\mathbf{2}]^{2-}$, $[\mathbf{3}]^{4-}$, $[\mathbf{4}]$) were successfully isolated from the reactions of $[\mathbf{1}]^{4-}$. These complexes have different nuclearity, trinuclear $[\mathbf{2}]^{2-}$, hexanuclear $[\mathbf{3}]^{4-}$, and heptanuclear $[\mathbf{4}]$, which were controlled by changing counter cations or solution pH. In basic conditions, the use of comparatively small cations (Na^+, Mg^{2+}, Ni^{2+}, Co^{2+}) led to the production of the trinuclear complex $[\mathbf{2}]^{2-}$, while in the case of bigger Ca^{2+} ion, only the hexanuclear complex $[\mathbf{3}]^{4-}$ was readily crystallized. In acidic conditions, the heptanuclear complex $[\mathbf{4}]$ was produced through the partial protonation of the carboxylate groups of msa and the formation of μ_3-S atoms. It should be noted that these heterometallic metal complexes derived from $[\mathbf{1}]^{4-}$ are the first examples of the structurally characterized first-raw transition metal complexes of thiomalic acid. In addition, the tridentate-O_α,O_β,S coordination mode of msa^{3-} in $[\mathbf{2}]^{2-}$ and $[\mathbf{3}]^{4-}$ was found for the first time.

In conclusion, it was found that the introduction of phenyldiphosphine gold units made it easy to crystallize the complex with H_3msa, which was difficult to crystallize in the past. As a result, insights to the coordination behavior of H_3msa was extensively developed by using the single-crystal X-ray analysis. A similar strategy is applicable for the crystallization and structural characterization of other high hydrophilic coordination systems that have Lewis base sites with a high affinity to gold(I) centers.

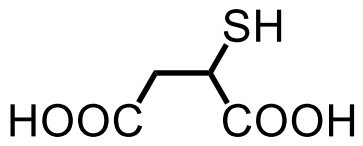

Chart 2-1. Molecular structure of thiomalic acid (H_3msa).

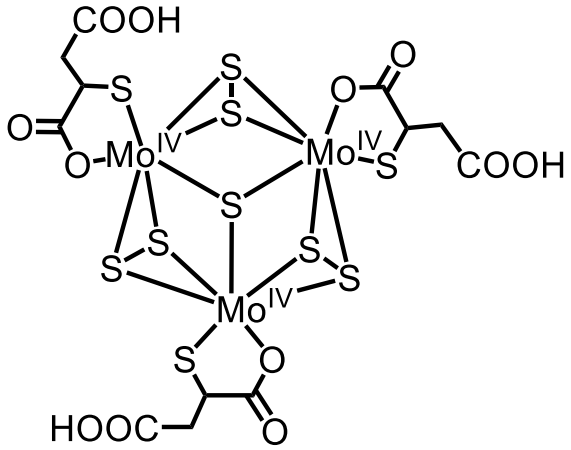

$[Mo^{IV}_3S(S_2)_3(Hmsa\text{-}O,S)_3]^{2-}$ [28]

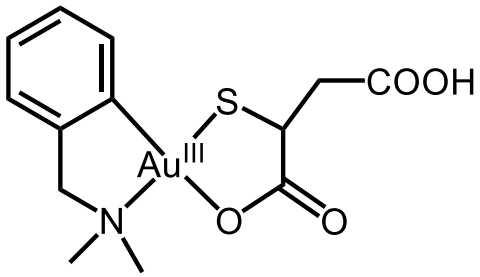

$[Au^{III}(Hmsa\text{-}O,S)(damp)]$ [31]

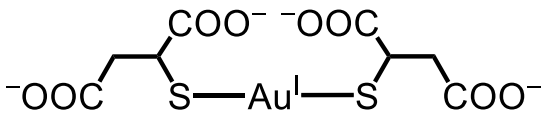

$[Au^{I}(msa\text{-}S)_2]^{5-}$ [29]

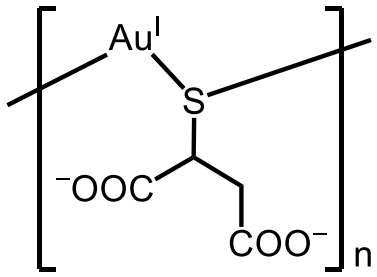

$([Au^{I}(msa\text{-}S)]^{2-})_n$ [30]

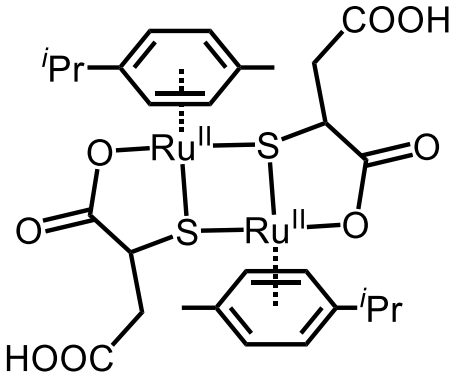

$[Ru^{II}_2(\eta^6\text{-}p\text{-cymene})_2(Hmsa\text{-}O,S)_2]$ [32]

Chart 2-2. Metal complexes of H_3msa that are structurally characterized to date.

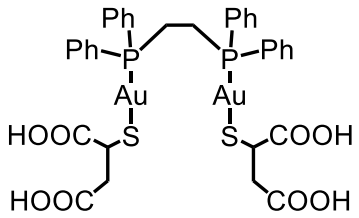

[Au_2(dppe)(H_2msa-*S*)$_2$]

Chart 2-3. Molecular structure of the digold(I) complexes with mixed diphosphine and H_2msa^- ([Au_2(dppe)(H_2msa-*S*)$_2$]).

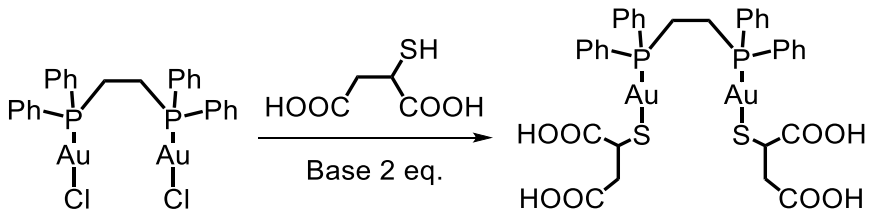

[Au_2(dppe)Cl_2] [Au_2(dppe)(H_2msa-*S*)$_2$]

Scheme 2-1. Synthetic route of [Au_2(dppe)(H_2msa-*S*)$_2$] ([H_4**1**]).

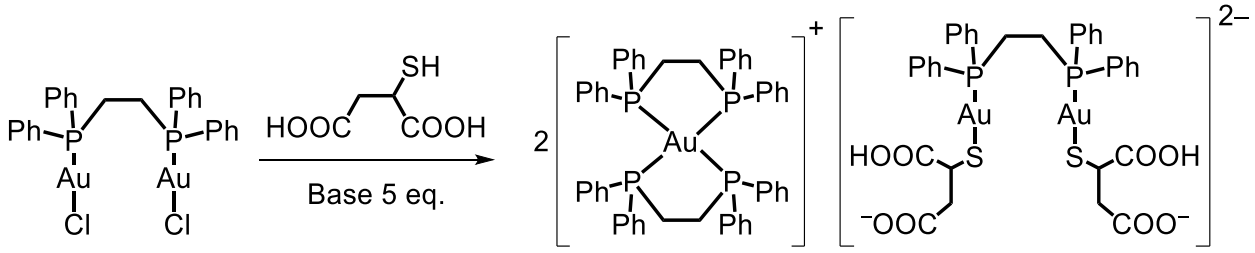

[Au_2(dppe)Cl_2] [Au(dppe)$_2$]$_2$[Au_2(dppe)(Hmsa-*S*)$_2$]

Scheme 2-2. Synthetic route of [Au(dppe)$_2$]$_2$[Au_2(dppe)(Hmsa-*S*)$_2$] ([**1'**]).

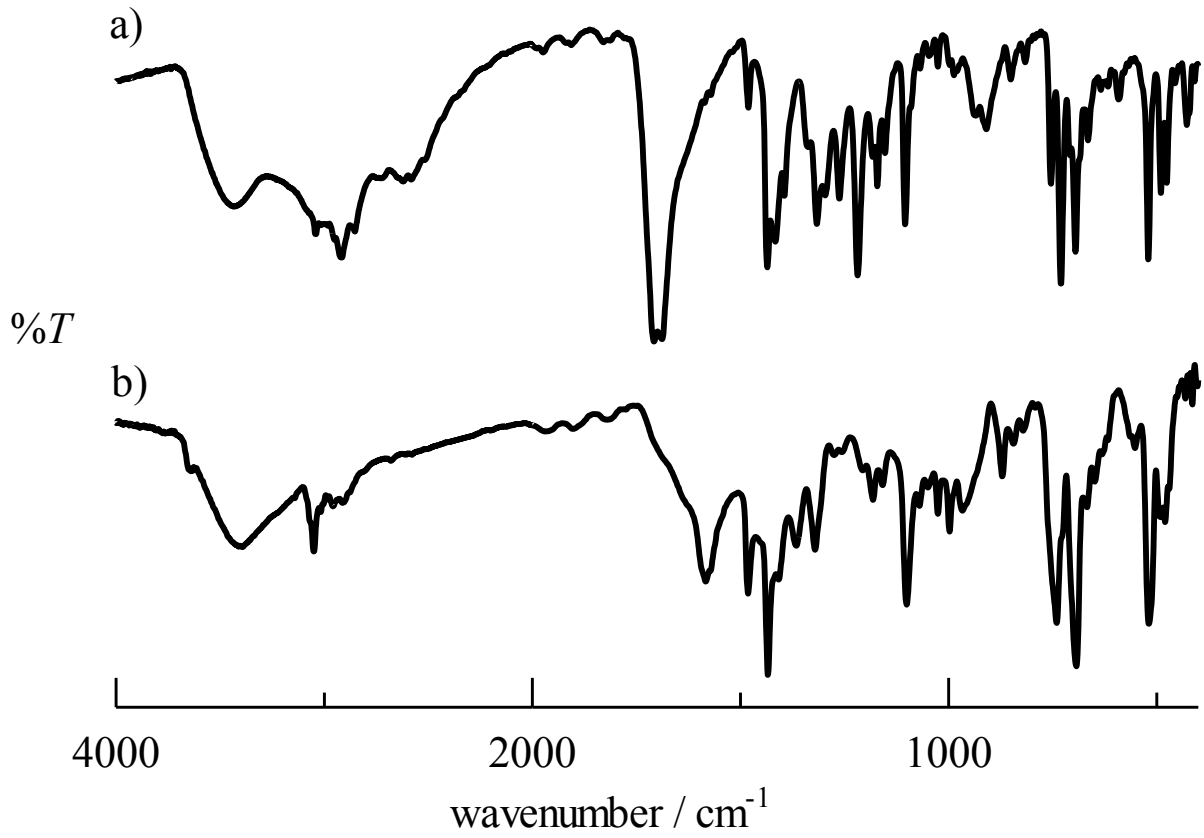

Figure 2-1. IR spectra of (a) $[Au_2(dppe)(rac\text{-}H_2msa)_2]$ ($[H_4\mathbf{1}]$) and (b) $[Au(dppe)_2]_2[Au_2(dppe)(Hmsa)_2]$ ([**1'**]) (KBr disks).

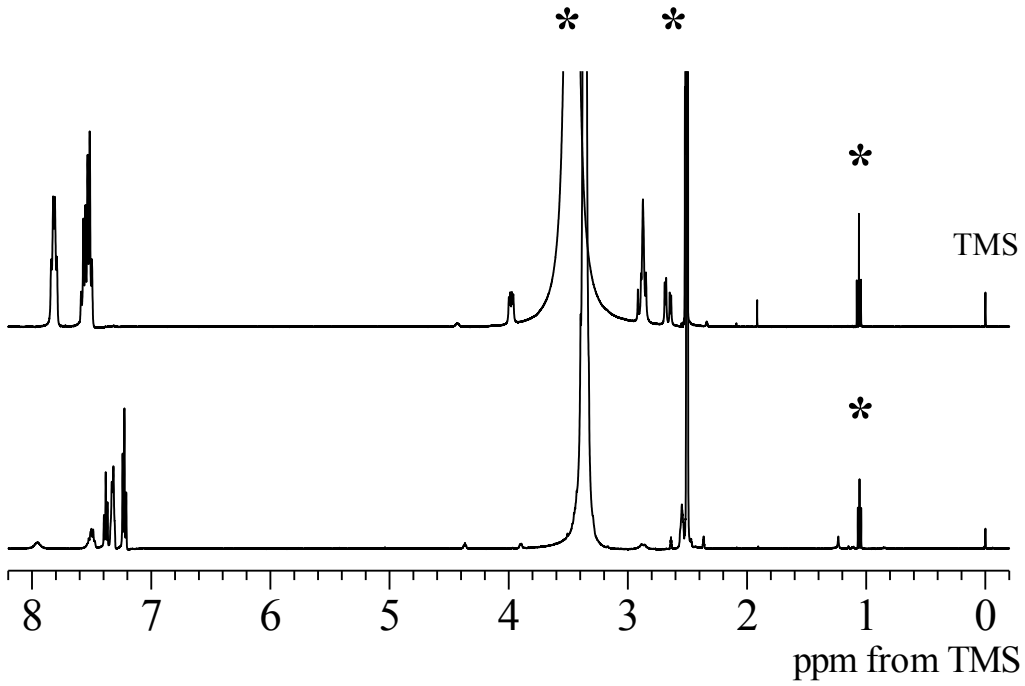

Figure 2-2. ^{1}H NMR spectra of (a) $[Au_2(dppe)(rac\text{-}H_2msa)_2]$ ([H_4**1**]), and (b) $[Au(dppe)_2]_2[Au_2(dppe)(Hmsa)_2]$ ([**1'**]) in DMSO-d_6. (* solvents).

Table 2-1. ^{1}H NMR spectral data for [H_4**1**] in DMSO-d_6.

Compounds	ppm from TMS	integration intensity	assignment*
[H_4**1**]	7.84-7.79 (m)	8H	A
	7.59-7.50 (m)	12H	A
	3.98 (dd)	2H	a
	2.92-2.85 (m)	6H	b + B
	2.66 (dd)	2H	b

* Characterization symbols are shown below.

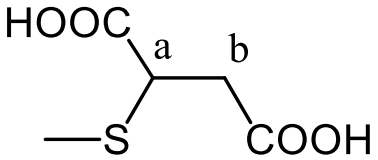

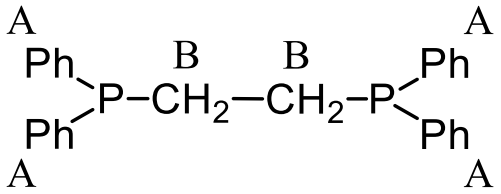

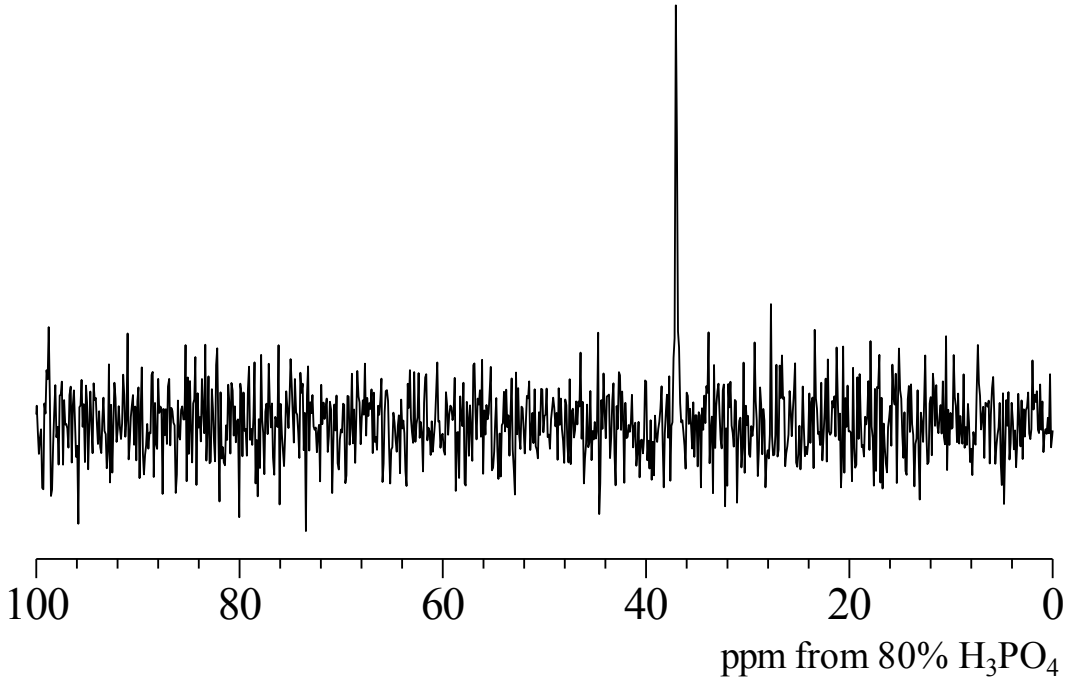

Figure 2-3. ^{31}P NMR spectrum of [H_4**1**] in DMSO-d_6.

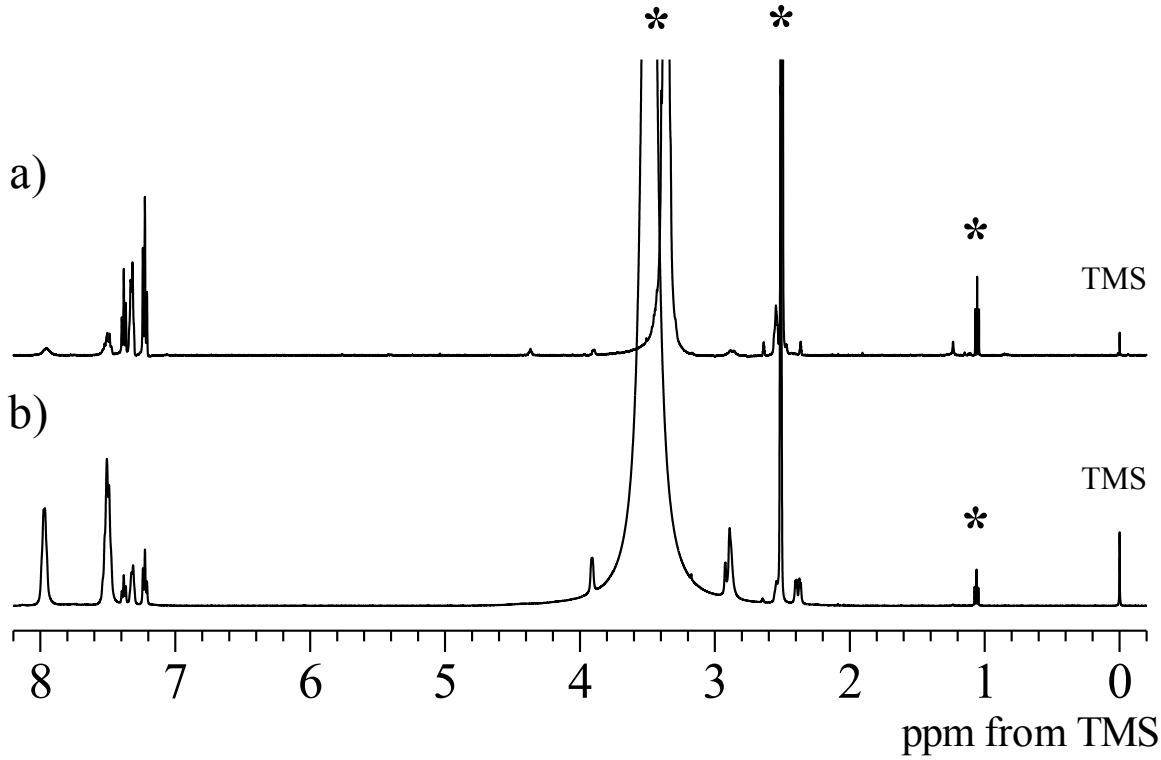

Figure 2-4. ^{1}H NMR spectra of (a) [**1'**] in DMSO-d_6 and (b) the reaction solution containing [Au_2(dppe)(*rac*-H_2msa)$_2$] and 3 molar equiv of KOH in DMSO-d_6 (* solvents).

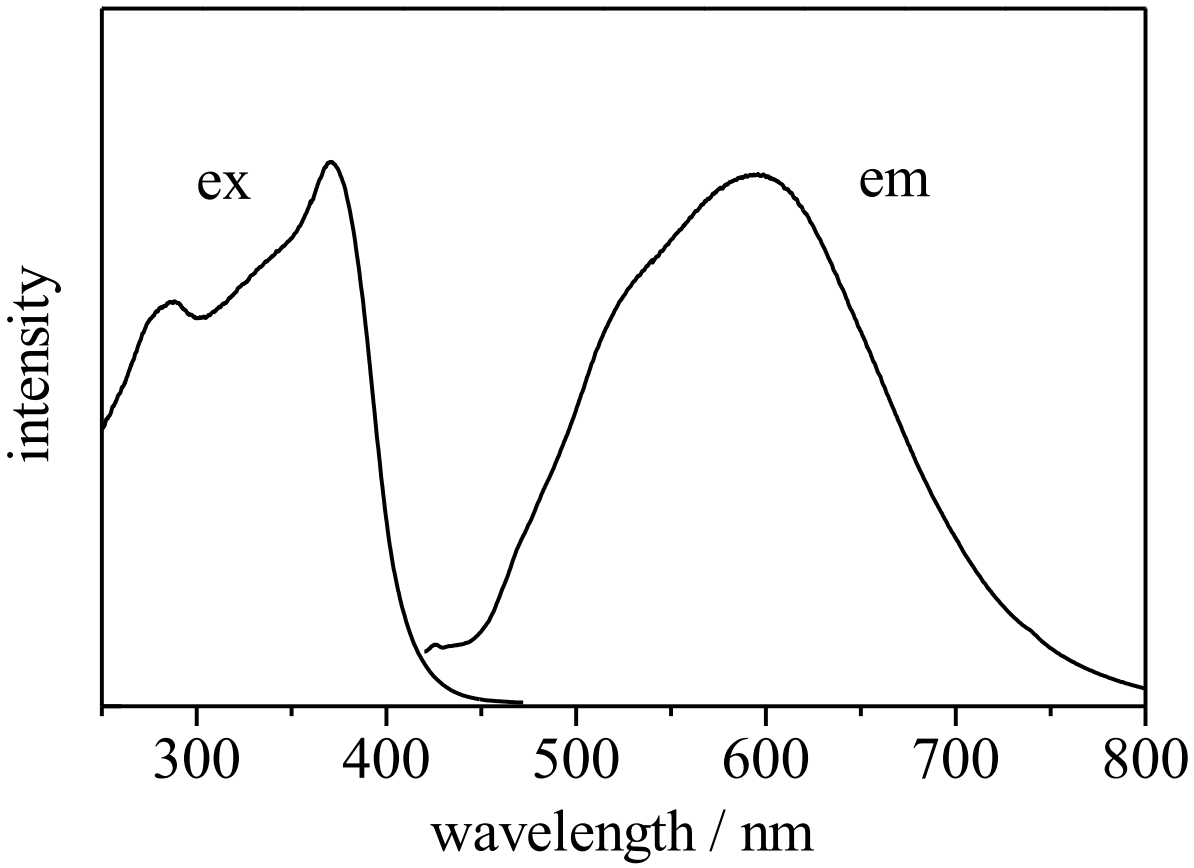

Figure 2-5. Emission (em, λ_{max} = 596 nm) and excitation (ex, λ_{max} = 370 and 288 nm) spectra of [**1'**]·2EtOH at room temperature in the solid state (λ_{ex} = 370 nm, λ_{em} = 600 nm).

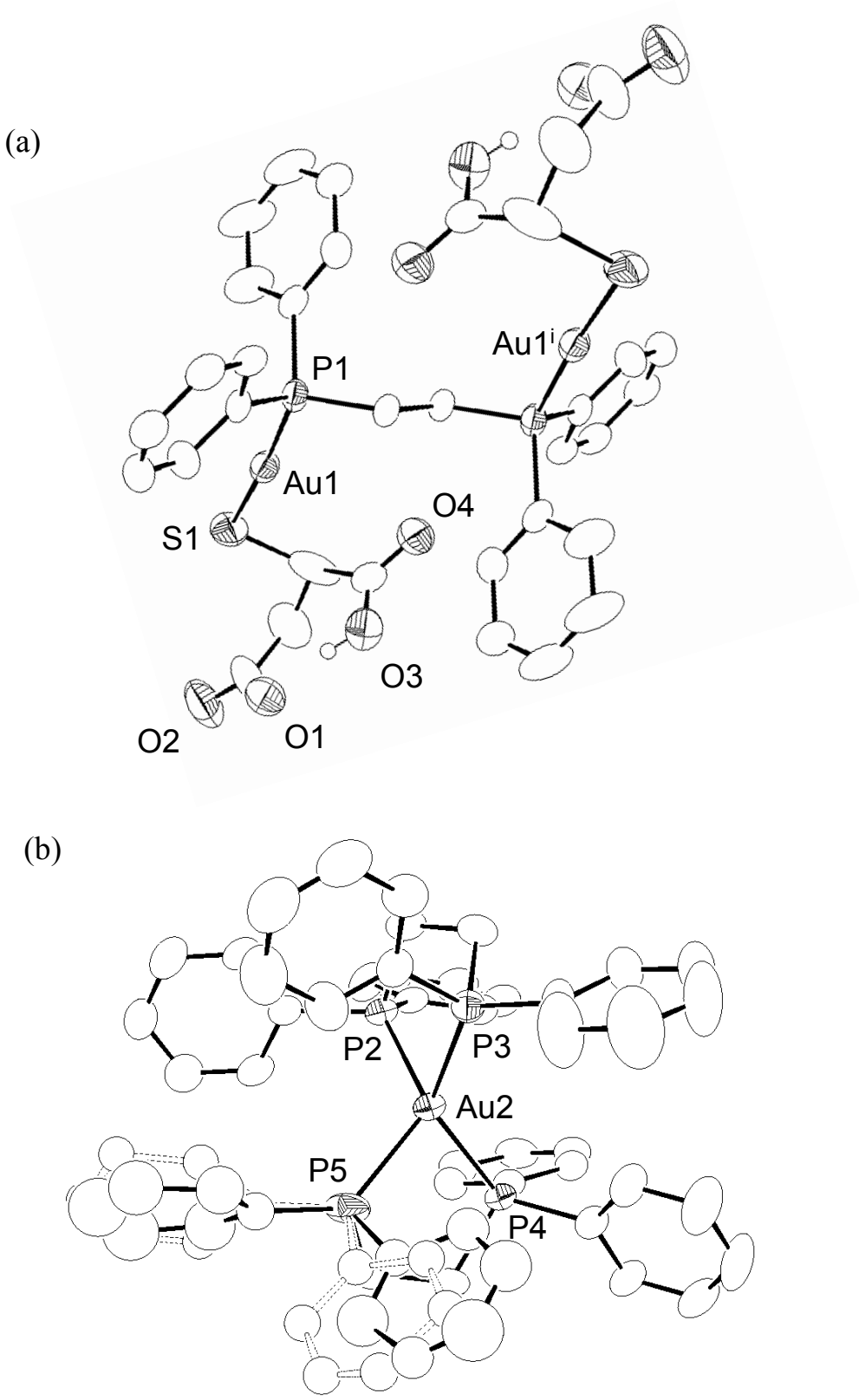

Figure 2-6. Perspective views of (a) the anionic complex and (b) the cationic complex in $[Au(dppe)_2]_2[Au_2(dppe)(Hmsa)_2]\cdot 2EtOH$ ([**1'**]·2EtOH).Thermal ellipsoids were drawn in a 50% level.

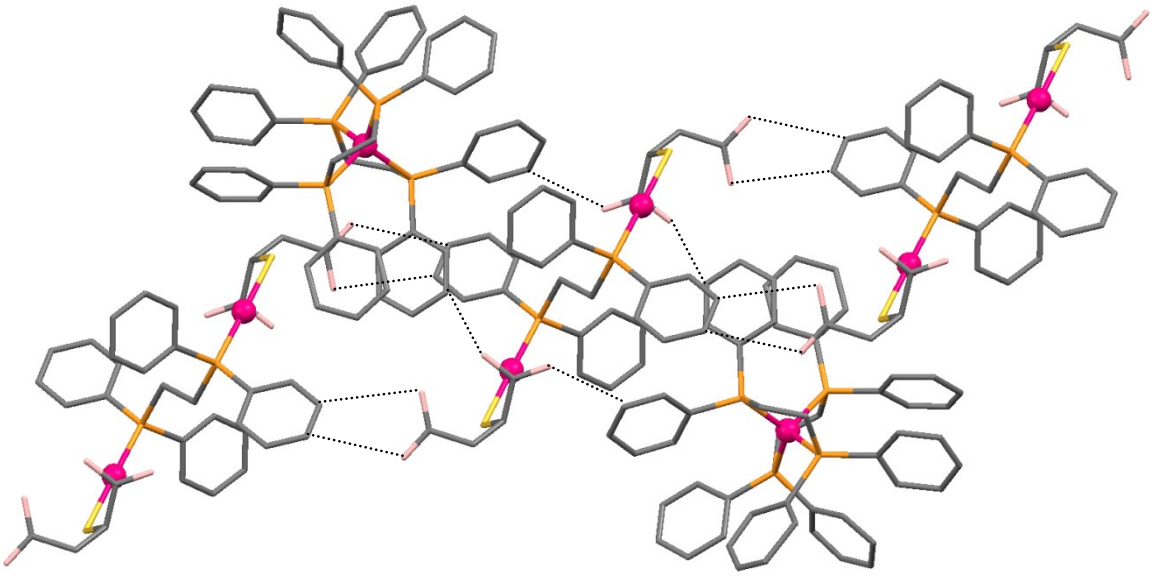

Figure 2-7. Perspective views of a packing structure in [**1'**]·2EtOH.

Table 2-2. Crystallographic data for $[Au(dppe)_2]_2[Au_2(dppe)(Hmsa)_2]\cdot 2EtOH$ ([**1'**]·2EtOH).

Empirical formula	$Au_4C_{142}H_{140}O_{10}P_{10}S_2$
Formula weight	3168.23
Crystal size / mm^3	0.13 × 0.10 × 0.10
Crystal system	Triclinic
Space group	*P*-1
a / Å	13.7732(5)
b / Å	14.1188(5)
c / Å	19.4275(7)
α /°	73.4670(10)
β /°	72.6830(10)
γ /°	67.5380(10)
V / $Å^3$	3269.9(2)
Z	1
T / K	200(2)
ρ_{calcd} / $g\cdot cm^{-3}$	1.609
μ(Mo Kα) /mm^{-1}	4.685
$2\theta_{Max}$	55.0
R(int)	0.0604
GOF	1.055
*R*1 ($I>2\sigma(I)$)[a)]	0.0434
w*R*2 (all data)[b)]	0.1098

a) $R1 = \Sigma||F_o|-|F_c|| / \Sigma|F_o|$.

b) $wR2 = [\Sigma(w(F_o^2-F_c^2)^2) / \Sigma w(F_o^2)^2]^{1/2}$.

Table 2-3. Selected bond lengths[Å] and angles [˚] for [**1'**]·2EtOH.

	Bond lengths		
Au(1)-P(1)	2.2663(14)	Au(2)-P(3)	2.3942(13)
Au(1)-S(1)	2.2866(17)	Au(2)-P(4)	2.3748(13)
Au(2)-P(2)	2.4082(13)	Au(2)-P(5)	2.4233(16)
	Angles		
P(1)-Au(1)-S(1)	175.70(5)	P(3)-Au(2)-P(4)	129.06(5)
P(2)-Au(2)-P(3)	84.82(5)	P(3)-Au(2)-P(5)	123.57(5)
P(2)-Au(2)-P(4)	119.22(5)	P(4)-Au(2)-P(5)	85.63(5)
P(2)-Au(2)-P(5)	118.70(6)		

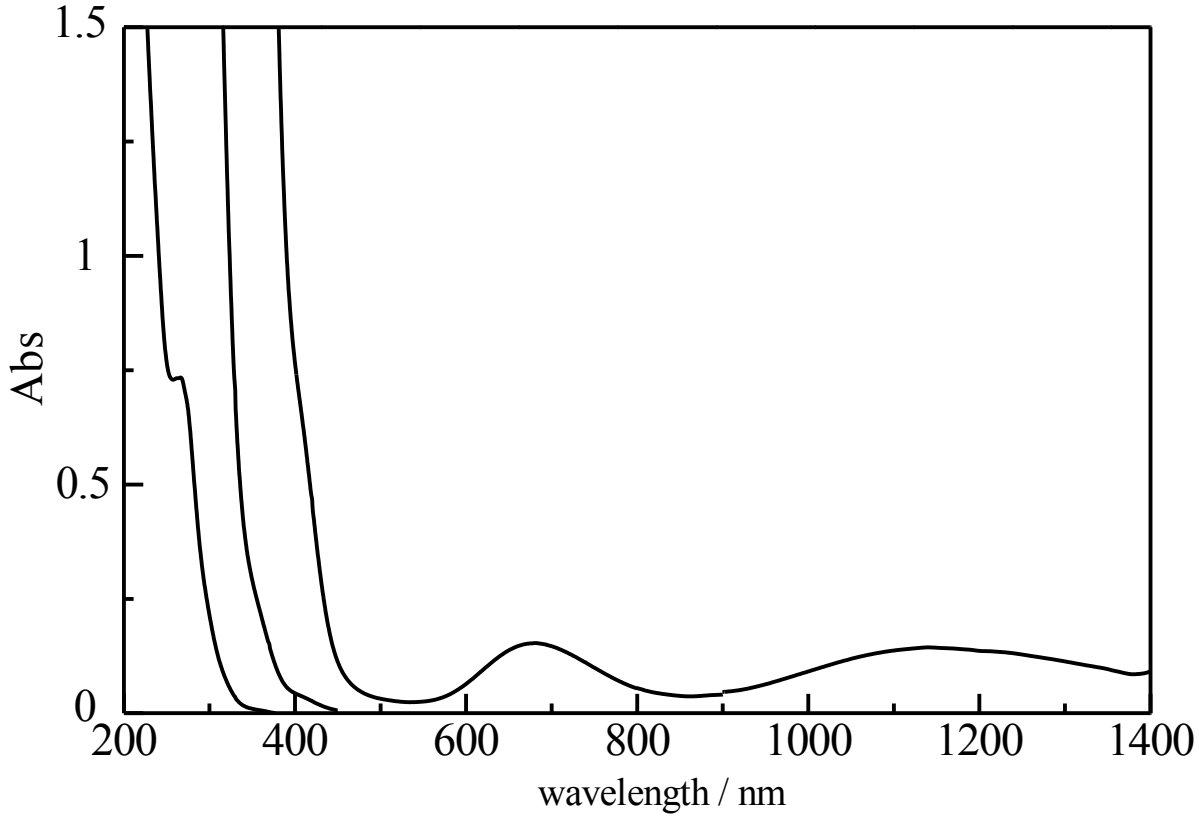

Figure 2-8. Absorption spectrum of the reaction solution containing $[Au_2(dppe)(rac\text{-msa})_2]^{4-}$ ($[\mathbf{1}]^{4-}$) and $Ni(OAc)_2 \cdot 4H_2O$ in MeOH. (λ_{max} / nm = 1136, 647, 267).

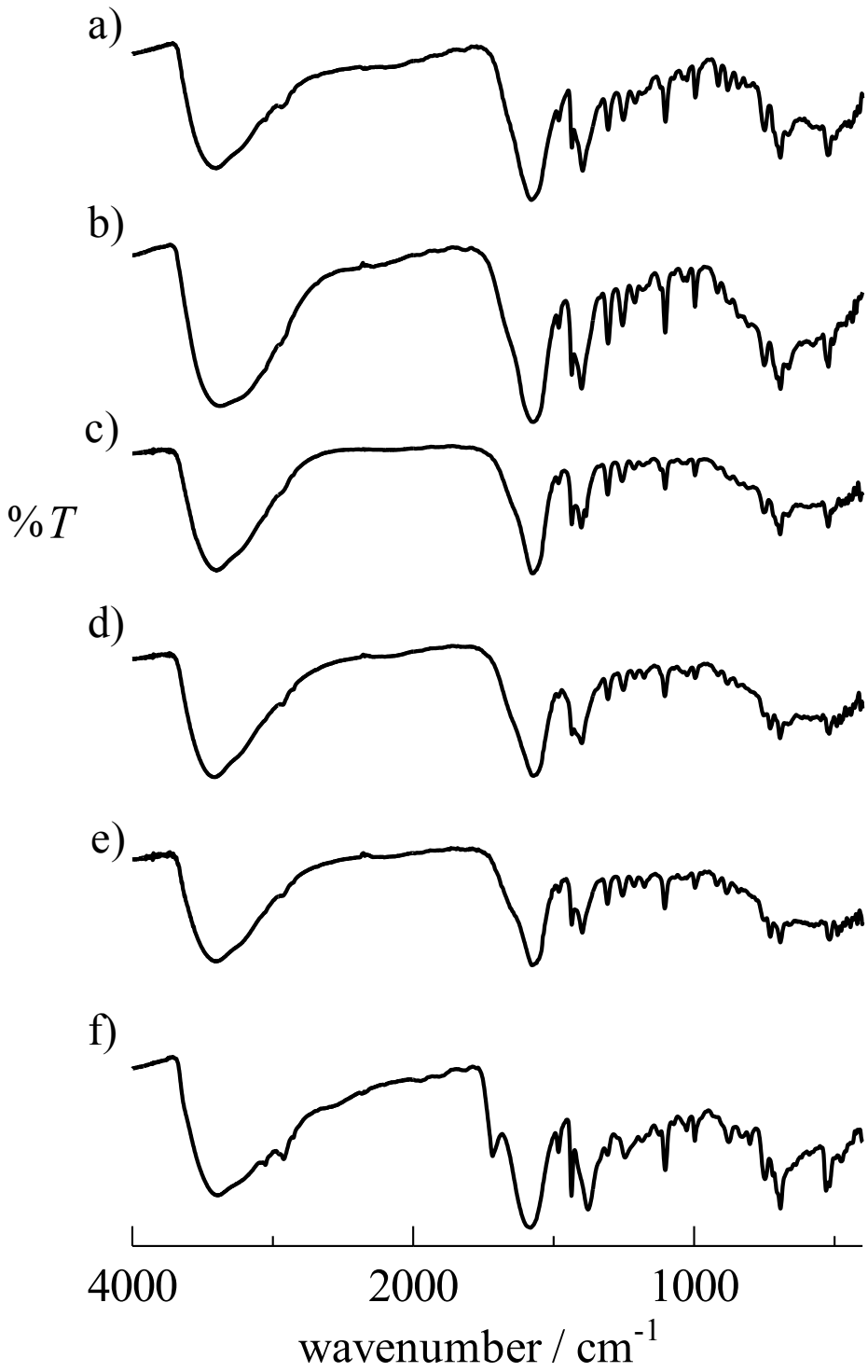

Figure 2-9. IR spectra of (a) $Na_2[Ni\{Au_2(dppe)(msa)_2\}]$ (Na_2[**2**]), (b) $Mg[Ni\{Au_2(dppe)(msa)_2\}]$ (Mg[**2**]), (c) $Ni[Ni\{Au_2(dppe)(msa)_2\}]$ (Ni[**2**]), (d) $Co[Ni\{Au_2(dppe)(msa)_2\}]$ (Co[**2**]), (e) $Ca_2[Ni_2\{Au_2(dppe)(msa)_2\}_2]$ (Ca_2[**3**]), and (f) $[Ni_3\{Au_2(dppe)(Hmsa)_2\}\{Au_2(dppe)(msa)_2\}(MeOH)_3]$ ([**4**]).

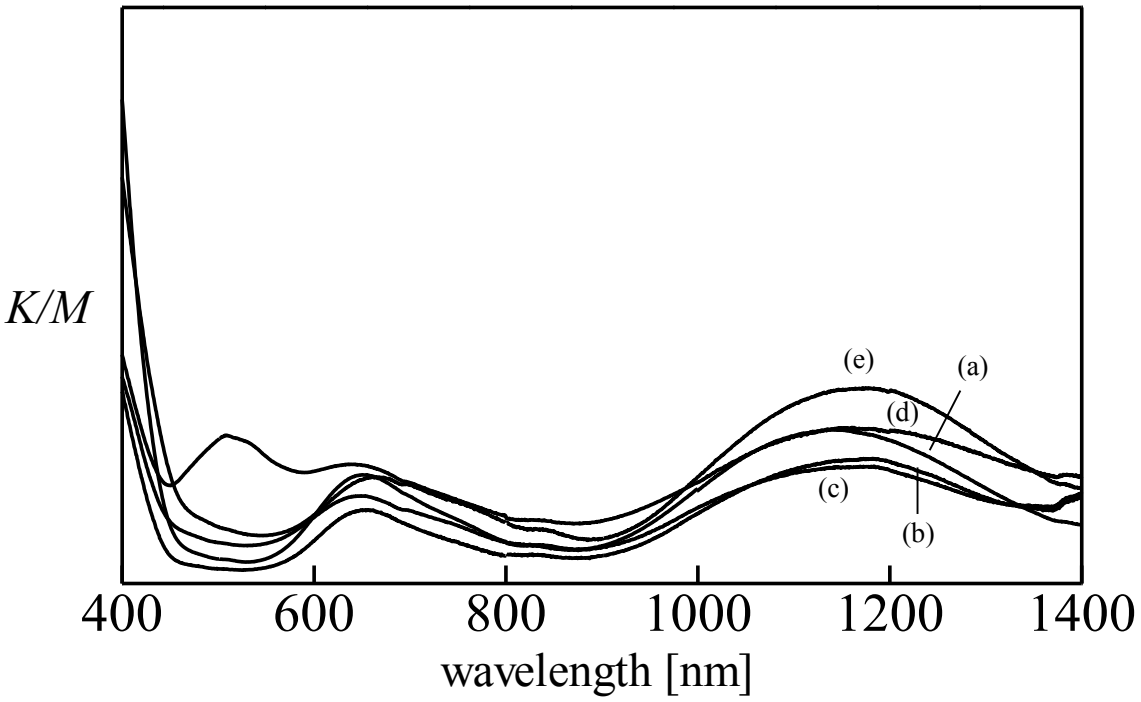

Figure 2-10. Diffuse reflection spectra of (a) $Na_2[Ni\{Au_2(dppe)(msa)_2\}]$ (Na_2[**2**]), (b) $Mg[Ni\{Au_2(dppe)(msa)_2\}]$ (Mg[**2**]), (c) $Ni[Ni\{Au_2(dppe)(msa)_2\}]$ (Ni[**2**]), (d) $Co[Ni\{Au_2(dppe)(msa)_2\}]$ (Co[**2**]), and (e) $Ca_2[Ni_2\{Au_2(dppe)(msa)_2\}_2]$ (Ca_2[**3**]).

Table 2-4. Spectral data of $Na_2[Ni\{Au_2(dppe)(msa)_2\}]$ (Na_2[**2**]) and $Mg[Ni\{Au_2(dppe)(msa)_2\}]$ (Mg[**2**]), $Ni[Ni\{Au_2(dppe)(msa)_2\}]$ (Ni[**2**]), $Co[Ni\{Au_2(dppe)(msa)_2\}]$ (Co[**2**]), and $Ca_2[Ni_2\{Au_2(dppe)(msa)_2\}_2]$ (Ca_2[**3**]) in the solid state.

Compounds	*K/M* maxima: λ / nm
Na_2[**2**]	651, 1041
Mg[**2**]	653, 1182
Ni[**2**]	649, 1184
Co[**2**]	509, 642, 1161
Ca_2[**3**]	665, 1175

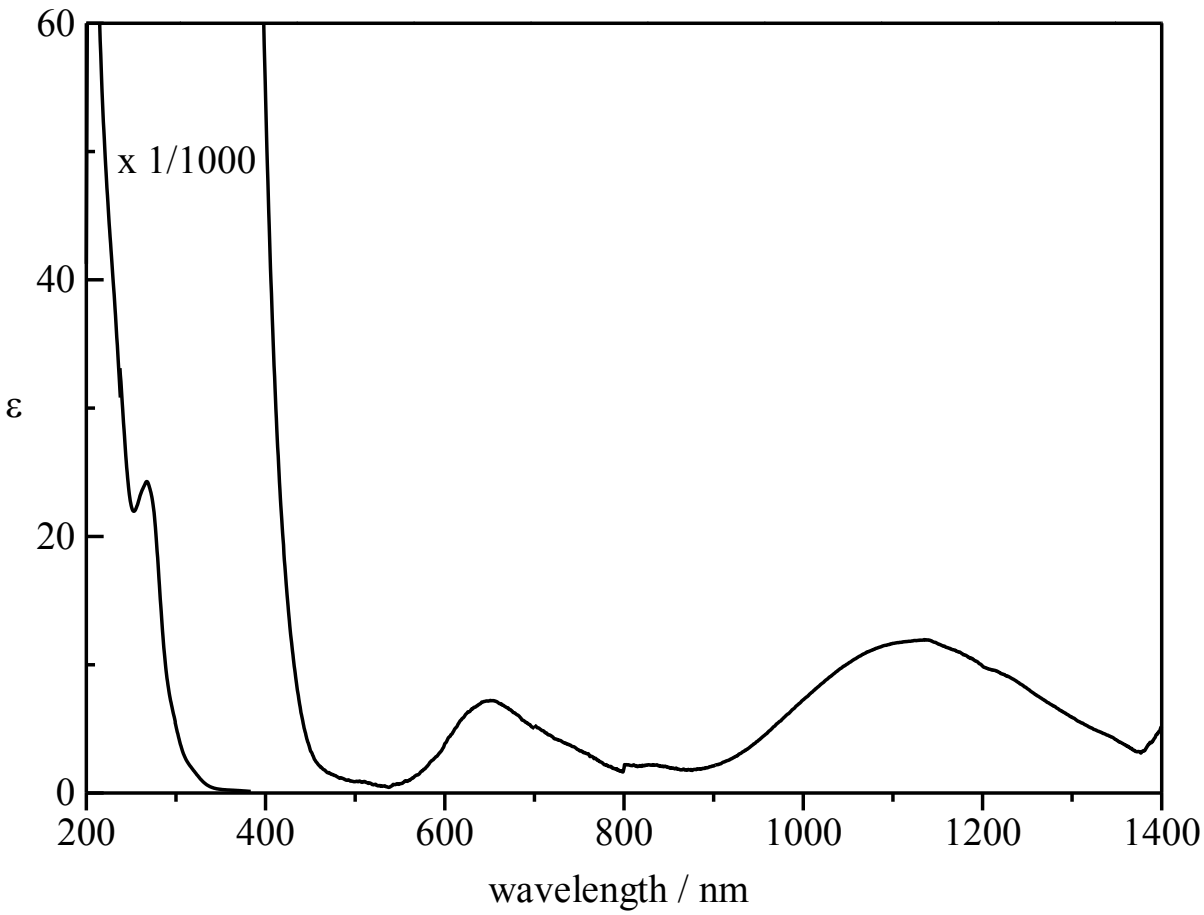

Figure 2-11. Absorption spectrum of $Na_2[Ni\{Au_2(dppe)(msa)_2\}]$ (Na_2[**2**]) in MeOH.

Table 2-5. Absorption spectral data of Na_2[**2**] in MeOH.

abs max: λ / nm	ε / mol^{-1} dm^3 cm^{-1}
1135	12.0
651	7.2
267.5	24000

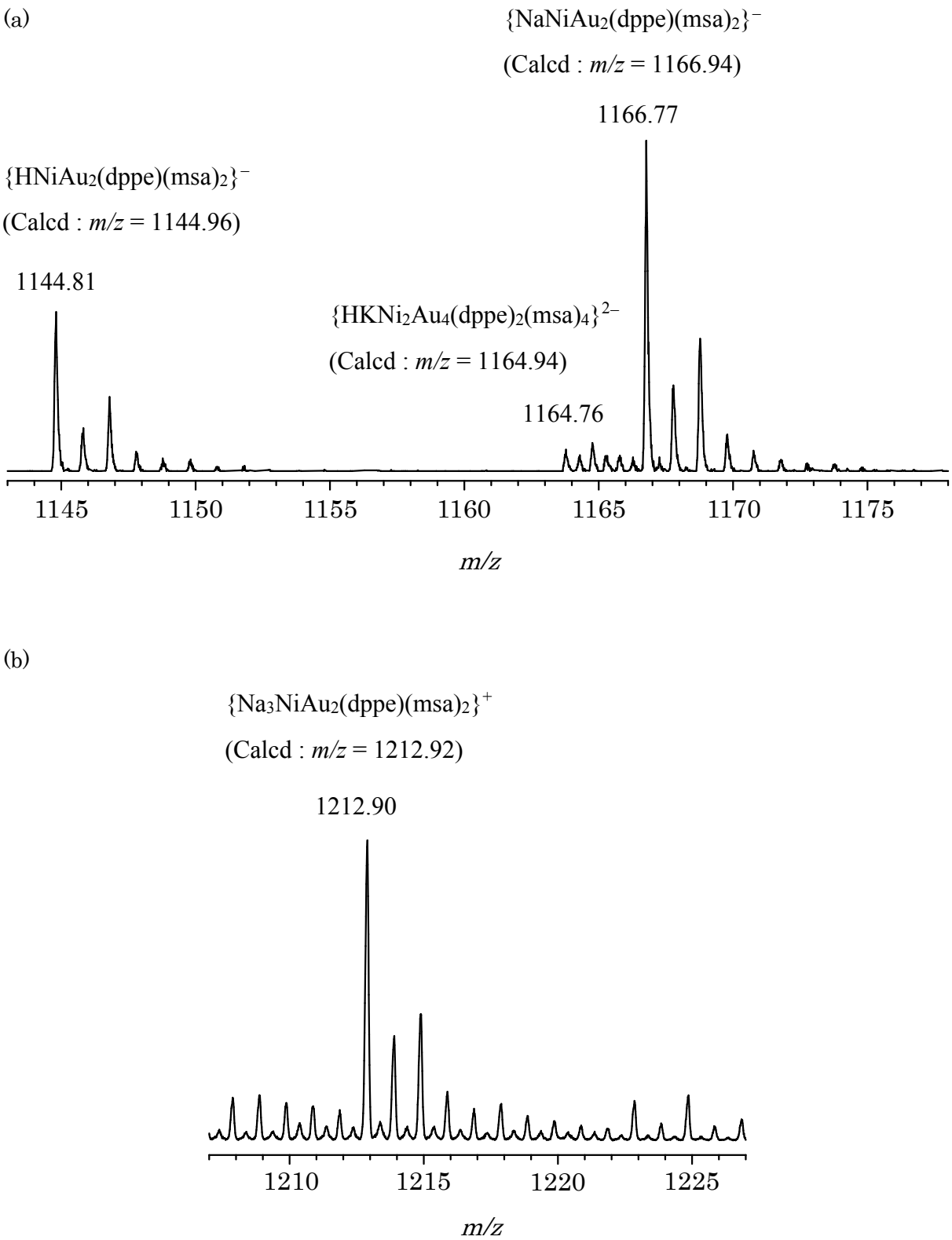

Figure 2-12. ESI-mass spectra of $Na_2[Ni\{Au_2(dppe)(msa)_2\}]$ (Na_2[**2**]) with (a) negative and (b) positive modes in methanol.

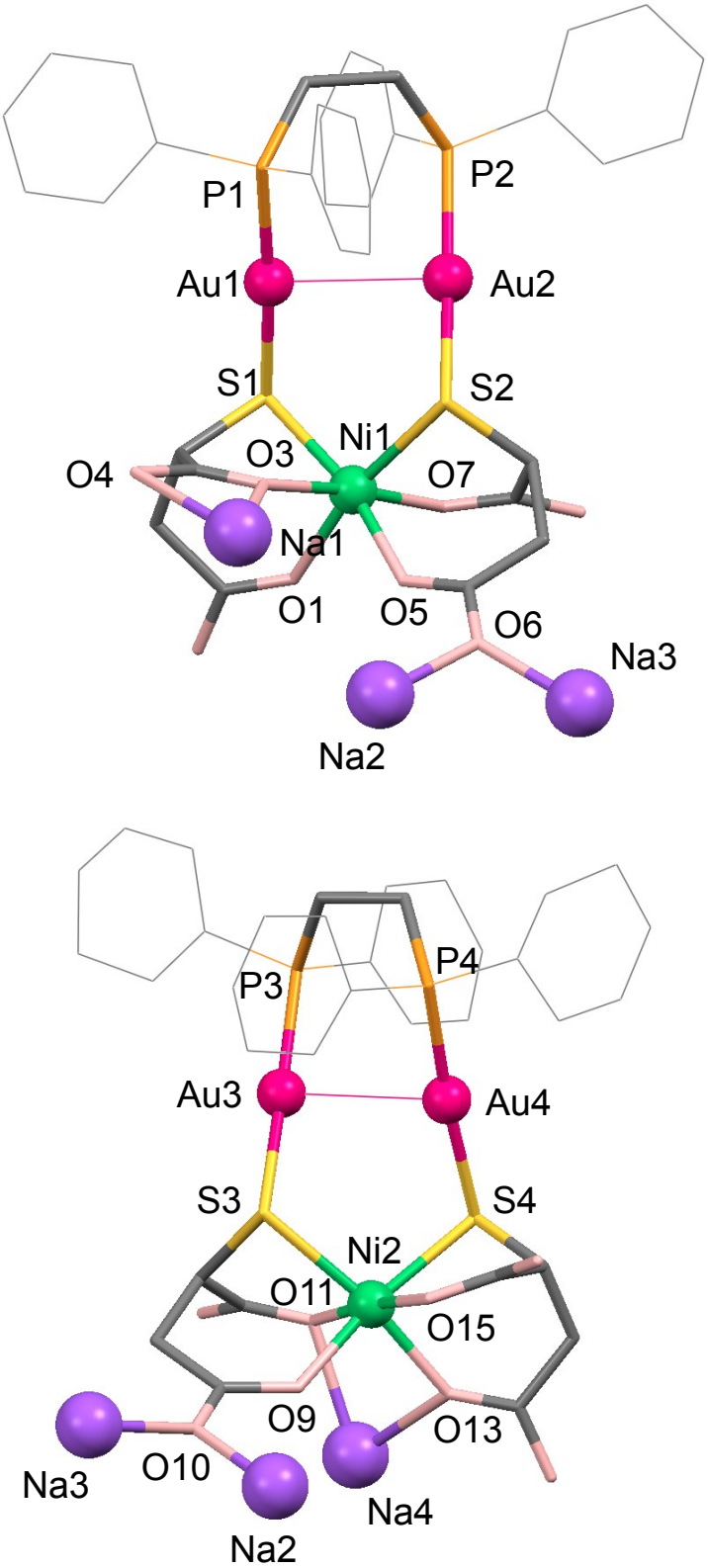

Figure 2-13. Perspective views of two crystallographical independent complex anions in $Na_2[Ni\{Au_2(dppe)(msa)_2\}]$ (Na_2[**2**]).

a)

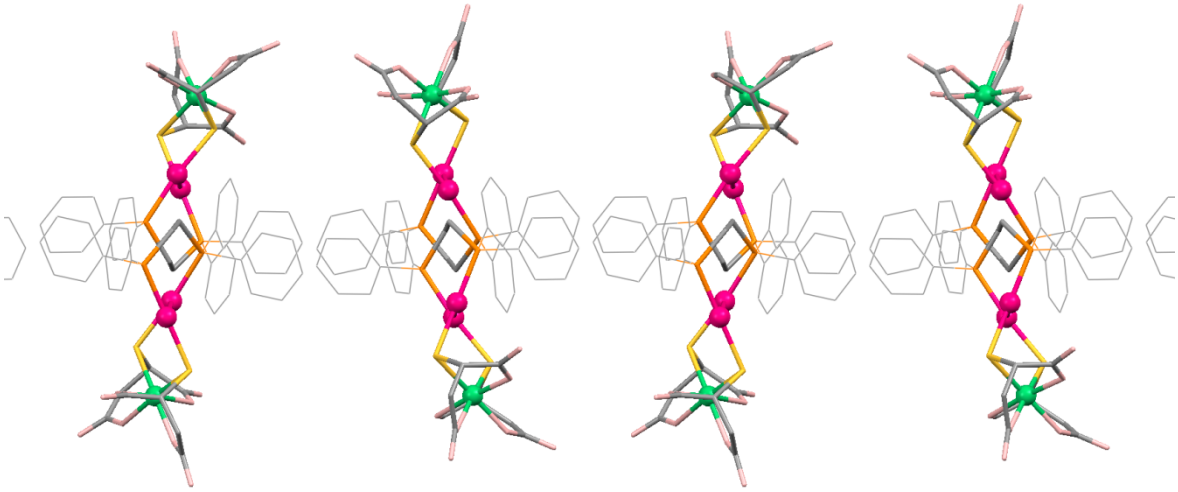

b)

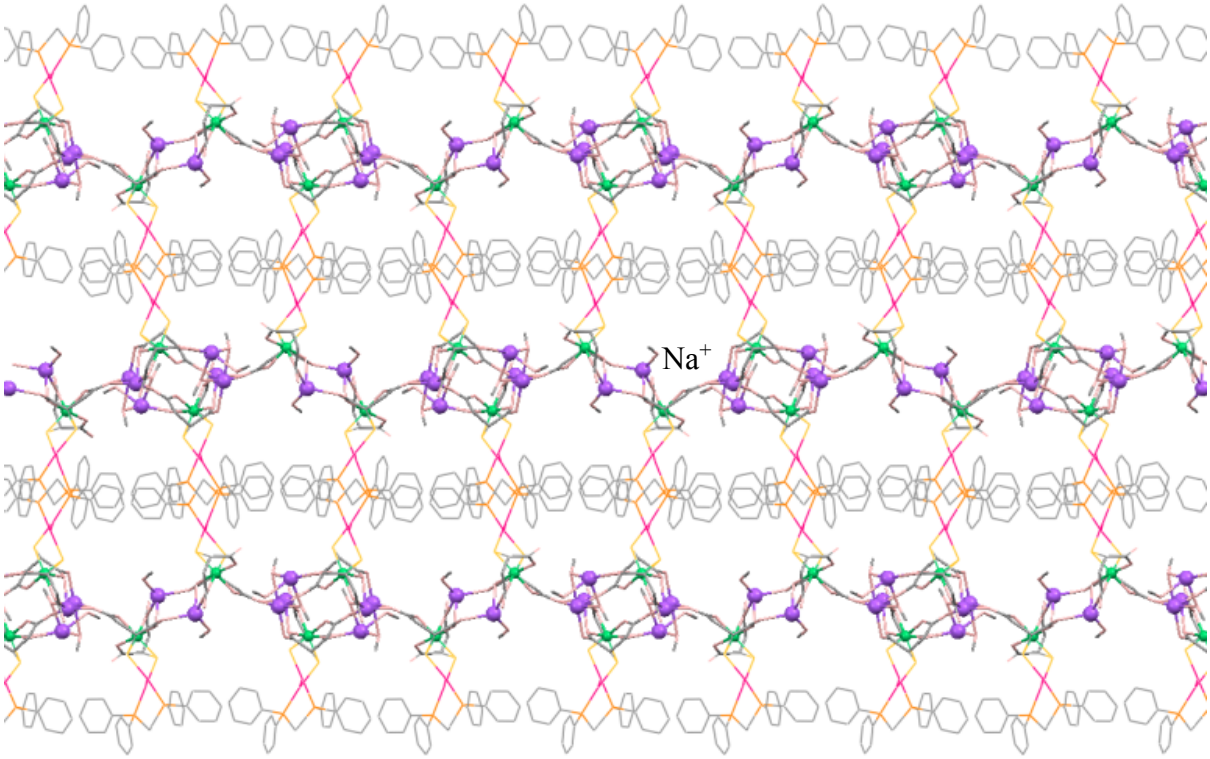

Figure 2-14. (a) A side view of the 2D sheet and (b) a packing structure of $Na_2[Ni\{Au_2(dppe)(msa)_2\}]\cdot 3MeOH$ (Na_2[**2**]·3MeOH).

Table 2-6. Crystallographic data for $Na_2[Ni\{Au_2(dppe)(msa)_2\}]\cdot 3MeOH$ (Na_2[**2**] ·3MeOH).

Empirical formula	$Au_4C_{75}H_{61}Na_4Ni_2O_{24}P_4S_4$
Formula weight	2595.60
Crystal size / mm^3	0.12 × 0.10 × 0.05
Crystal system	Monoclinic
Space group	$P2_1/c$
a / Å	17.848(3)
b / Å	21.586(3)
c / Å	33.891(3)
α /°	90
β /°	106.314(10)
γ /°	90
V / $Å^3$	12532(3)
Z	4
T / K	200(2)
ρ_{calcd} / $g\cdot cm^{-3}$	1.367
μ(Mo Kα) /mm^{-1}	5.141
$2\theta_{Max}$	55.0
R(int)	0.1232
GOF	1.830
$R1$ (I>2σ(I))[a)]	0.1766
w$R2$ (all data)[b)]	0.5264

a) $R1 = \Sigma||F_o|-|F_c|| / \Sigma|F_o|$. b) $wR2 = [\Sigma(w(F_o^2-F_c^2)^2) / \Sigma w(F_o^2)^2]^{1/2}$.

Table 2-7. Bond lengths [Å] and angles [°] for Na_2[**2**] ·3MeOH.

	Bond lengths		
Au(1)-P(1)	2.276(7)	Ni(1)-O(7)	2.074(16)
Au(3)-P(3)	2.275(6)	Ni(2)-O(15)	2.073(17)
Au(1)-S(1)	2.304(7)	Ni(2)-S(3)	2.427(7)
Au(3)-S(3)	2.321(7)	Ni(2)-S(4)	2.412(7)
Au(2)-P(2)	2.290(6)	Ni(2)-O(9)	2.019(18)
Au(4)-P(4)	2.248(7)	Ni(2)-O(11)	2.09(2)
Au(2)-S(2)	2.303(6)	Ni(2)-O(13)	2.068(19)
Au(4)-S(4)	2.321(7)	Ni(2)-O(15)	2.073(17)
Au(1)-Au(2)	2.9687(13)	Na(1)-O(3)	2.37(2)
Au(3)-Au(4)	2.9568(14)	Na(3)-O(1)#1	2.364(17)
Au(3)-P(3)	2.275(6)	Na(1)-O(4)	2.62(3)
Au(3)-S(3)	2.321(7)	Na(3)-O(6)	2.29(2)
Au(4)-P(4)	2.248(7)	Na(2)-O(6)	2.359(19)
Au(4)-S(4)	2.321(7)	Na(3)-O(10)	2.34(2)
Au(3)-Au(4)	2.9568(14)	Na(2)-O(8)#1	2.41(2)
Ni(1)-S(1)	2.428(7)	Na(4)-O(11)	2.41(2)
Ni(2)-S(3)	2.427(7)	Na(2)-O(10)	2.40(2)
Ni(1)-S(2)	2.410(7)	Na(4)-O(12)#2	2.41(2)
Ni(2)-S(4)	2.412(7)	Na(3)-O(1)#1	2.364(17)
Ni(1)-O(1)	2.070(16)	Na(3)-O(6)	2.29(2)
Ni(2)-O(9)	2.019(18)	Na(3)-O(10)	2.34(2)
Ni(1)-O(3)	2.041(16)	Na(4)-O(11)	2.41(2)
Ni(2)-O(11)	2.09(2)	Na(4)-O(12)#2	2.41(2)
Ni(1)-O(5)	2.049(17)	Na(4)-O(13)	2.45(2)
Ni(2)-O(13)	2.068(19)		
	Angles		
P(1)-Au(1)-S(1)	175.9(2)	S(1)-Ni(1)-O(5)	167.9(5)
P(2)-Au(2)-S(2)	174.0(2)	S(1)-Ni(1)-O(7)	87.1(6)
P(3)-Au(3)-S(3)	174.2(2)	S(2)-Ni(1)-O(1)	168.3(5)
P(4)-Au(4)-S(4)	175.8(2)	S(2)-Ni(1)-O(3)	96.0(5)
S(1)-Ni(1)-S(2)	103.5(2)	S(2)-Ni(1)-O(5)	85.5(5)
S(1)-Ni(1)-O(1)	85.3(5)	S(2)-Ni(1)-O(7)	87.1(6)
S(1)-Ni(1)-O(3)	83.3(5)	O(1)-Ni(1)-O(3)	92.7(6)

Table 2-7. (continued).

Angles			
O(1)-Ni(1)-O(5)	87.1(7)	S(4)-Ni(2)-O(9)	171.1(6)
O(1)-Ni(1)-O(7)	83.7(7)	S(4)-Ni(2)-O(11)	98.8(6)
O(3)-Ni(1)-O(5)	87.7(7)	S(4)-Ni(2)-O(13)	84.4(6)
O(3)-Ni(1)-O(7)	174.8(7)	S(4)-Ni(2)-O(15)	84.5(6)
O(5)-Ni(1)-O(7)	88.3(7)	O(9)-Ni(2)-O(11)	86.5(8)
S(3)-Ni(2)-S(4)	102.7(3)	O(9)-Ni(2)-O(13)	88.6(8)
S(3)-Ni(2)-O(9)	85.0(5)	O(9)-Ni(2)-O(15)	89.8(7)
S(3)-Ni(2)-O(11)	83.8(6)	O(11)-Ni(2)-O(13)	88.5(8)
S(3)-Ni(2)-O(13)	170.3(6)	O(11)-Ni(2)-O(15)	175.0(8)
S(3)-Ni(2)-O(15)	99.1(5)	O(13)-Ni(2)-O(15)	88.1(7)

Symmetry transformations used to generate equivalent atoms:

#1 -x+1,-y+1,-z+2 #2 -x+1,-y+2,-z+2

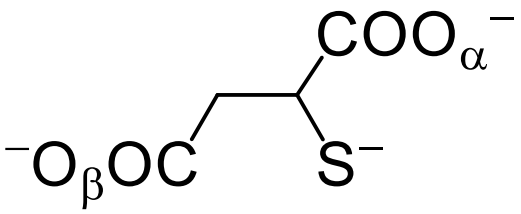

Chart 2-4. Definition of O_α and O_β atoms in msa^{3-}.

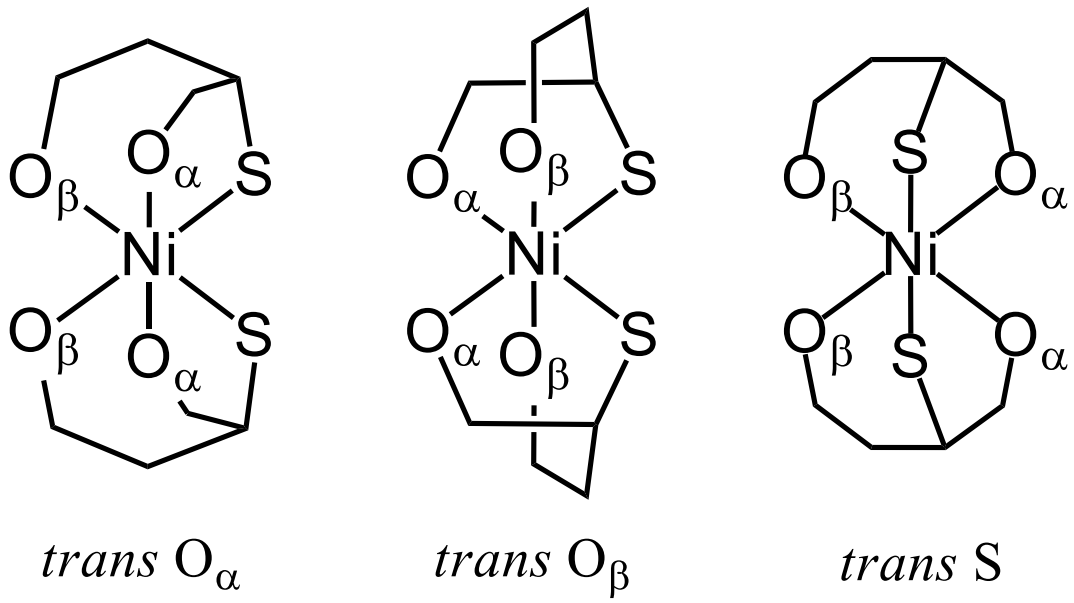

Chart 2-5. Possible coordination modes of $[Ni(R\text{-msa-}O_\alpha,O_\beta,S)_2]^{4-}$ unit.

a)

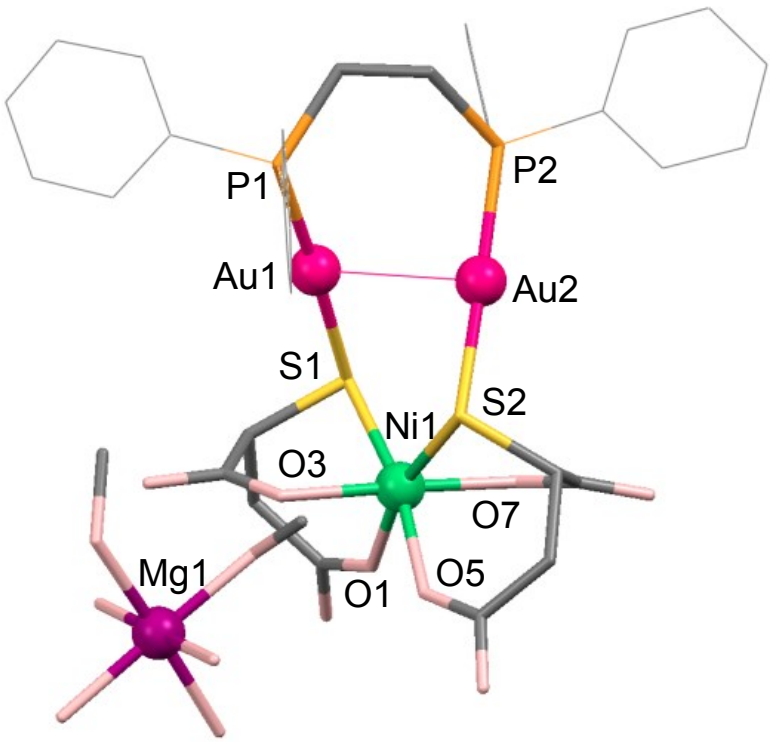

b)

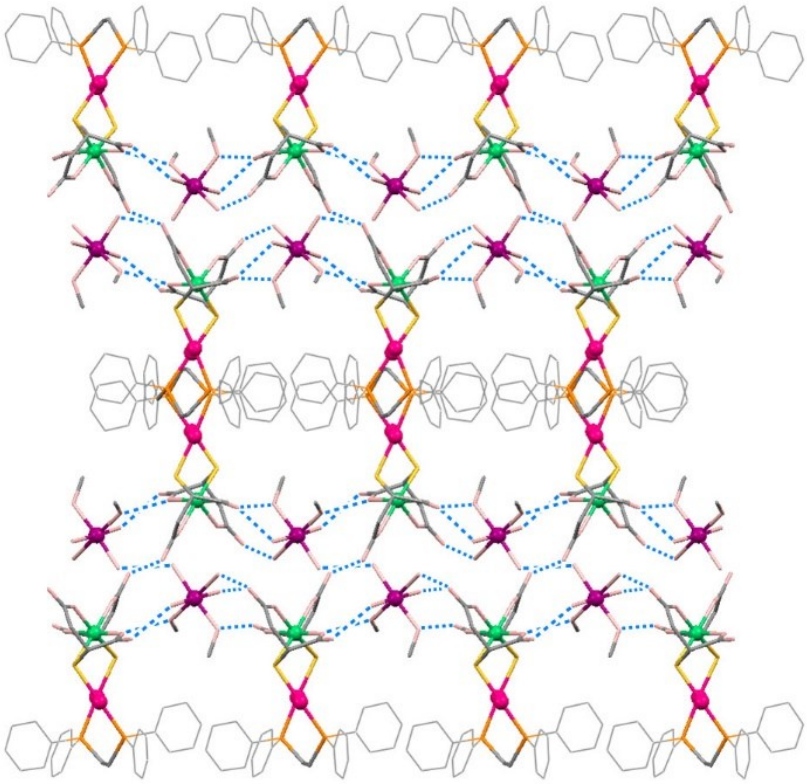

Figure 2-15. Perspective views of (a) the asymmetric unit and (b) a packing structure viewed from *c* axis in *rac*-$[Mg(H_2O)_4(MeOH)_2][Ni\{Au_2(dppe)(msa)_2\}]$ (Mg[**2**]). Dashed lines indicate OH…O hydrogen bonds.

Table 2-8. Crystallographic data for $[Mg(H_2O)_4(MeOH)_2][Ni\{Au_2(dppe)(msa)_2\}]\cdot 6H_2O$ ($Mg[\mathbf{2}]\cdot 6H_2O$).

Empirical formula	$Au_2C_{36}H_{46}MgNiO_{14}P_2S_2$
Formula weight	1391.66
Crystal size / mm^3	0.25 × 0.10 × 0.10
Crystal system	Monoclinic
Space group	$P2_1/c$
a / Å	10.6713(7)
b / Å	36.214(2)
c / Å	18.2046(13)
α /°	90
β /°	103.435(7)
γ /°	90
V / $Å^3$	6842.7(8)
Z	4
T / K	200(2)
ρ_{calcd} / $g\cdot cm^{-3}$	1.267
μ(Mo Kα) /mm^{-1}	4.707
$2\theta_{Max}$	55.0
R(int)	0.0652
GOF	1.045
$R1$ ($I>2\sigma(I)$)[a)]	0.0695
w$R2$ (all data)[b)]	0.2039

a) $R1 = \Sigma||F_o|-|F_c|| / \Sigma|F_o|$. b) $wR2 = [\Sigma(w(F_o^2-F_c^2)^2) / \Sigma w(F_o^2)^2]^{1/2}$.

Table 2-9. Bond lengths [Å] and angles [°] for Mg[**2**]·6H_2O.

	Bond lengths		
Au(1)-P(1)	2.259(3)	Ni(1)-O(5)	2.048(10)
Au(1)-S(1)	2.314(3)	Ni(1)-O(7)	2.032(11)
Au(2)-P(2)	2.269(4)	Mg(1)-O(9)	2.071(12)
Au(2)-S(2)	2.303(4)	Mg(1)-O(10)	2.052(13)
Au(1)-Au(2)	2.9296(7)	Mg(1)-O(11)	2.062(16)
Ni(1)-S(1)	2.388(4)	Mg(1)-O(12)	2.096(13)
Ni(1)-S(2)	2.403(4)	Mg(1)-O(13)	2.038(15)
Ni(1)-O(1)	2.078(10)	Mg(1)-O(14)	2.080(13)
Ni(1)-O(3)	2.034(10)		
	Angles		
P(1)-Au(1)-S(1)	177.61(12)	O(5)-Ni(1)-O(7)	92.8(4)
P(2)-Au(2)-S(2)	176.65(13)	O(9)-Mg(1)-O(10)	91.5(6)
S(1)-Ni(1)-S(2)	105.05(14)	O(9)-Mg(1)-O(11)	85.7(6)
S(1)-Ni(1)-O(1)	85.6(3)	O(9)-Mg(1)-O(12)	90.4(5)
S(1)-Ni(1)-O(3)	84.9(3)	O(9)-Mg(1)-O(13)	91.8(6)
S(1)-Ni(1)-O(5)	168.1(4)	O(9)-Mg(1)-O(14)	176.4(5)
S(1)-Ni(1)-O(7)	94.6(3)	O(10)-Mg(1)-O(11)	90.7(6)
S(2)-Ni(1)-O(1)	166.5(3)	O(10)-Mg(1)-O(12)	177.7(6)
S(2)-Ni(1)-O(3)	99.1(3)	O(10)-Mg(1)-O(13)	90.3(5)
S(2)-Ni(1)-O(5)	85.0(3)	O(10)-Mg(1)-O(14)	91.3(5)
S(2)-Ni(1)-O(7)	84.1(3)	O(11)-Mg(1)-O(12)	90.8(6)
O(1)-Ni(1)-O(3)	89.9(4)	O(11)-Mg(1)-O(13)	177.3(6)
O(1)-Ni(1)-O(5)	85.5(4)	O(11)-Mg(1)-O(14)	92.0(6)
O(1)-Ni(1)-O(7)	86.8(4)	O(12)-Mg(1)-O(13)	88.3(6)
O(3)-Ni(1)-O(5)	87.1(4)	O(12)-Mg(1)-O(14)	86.9(5)
O(3)-Ni(1)-O(7)	176.7(4)	O(13)-Mg(1)-O(14)	90.5(6)

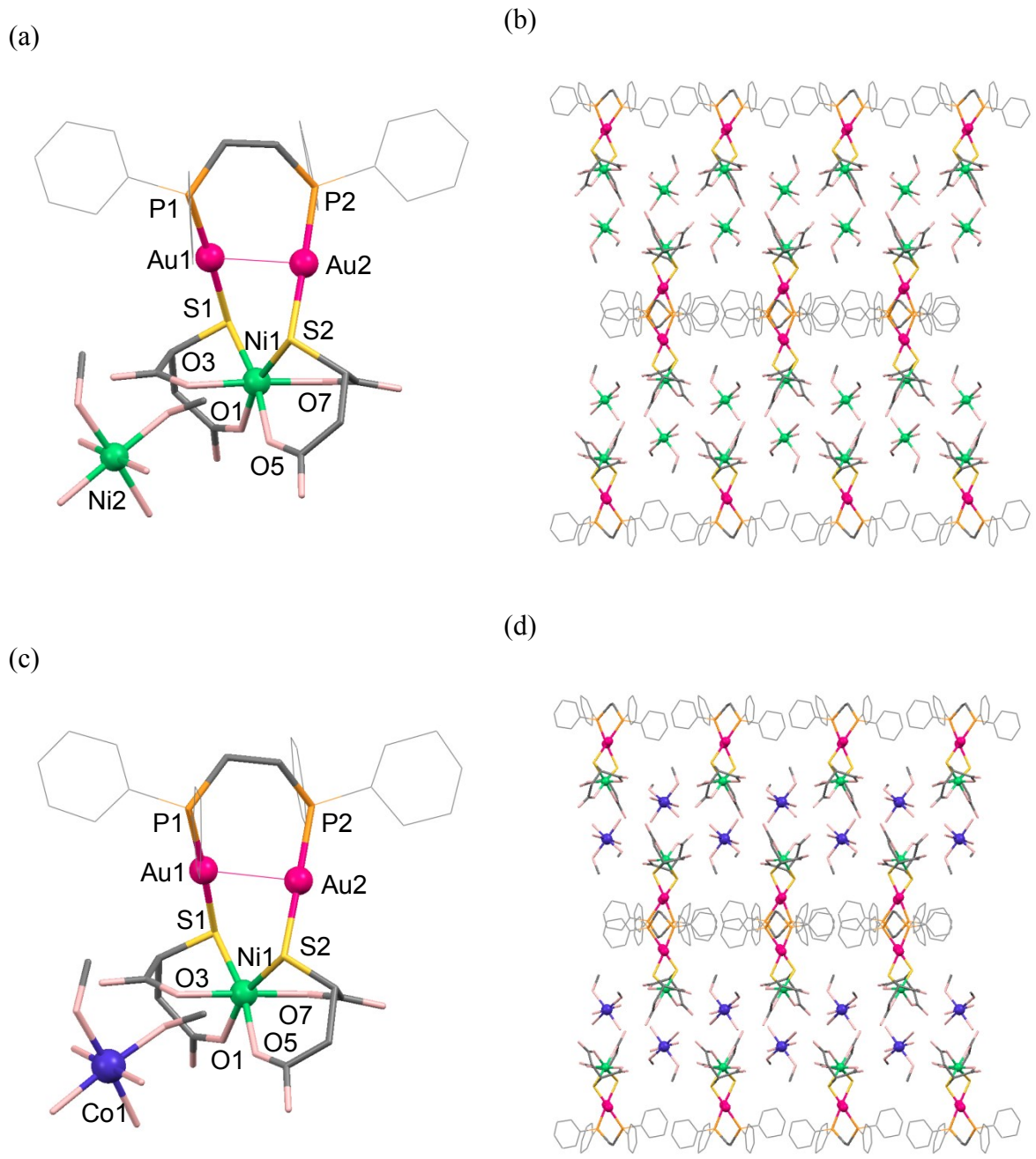

Figure 2-16. Perspective views of (a) the asymmetric unit and (b) a packing structure viewed from *c* axis in *rac*-[Ni(H_2O)$_4$($MeOH$)$_2$][Ni{Au$_2$(dppe)(msa)$_2$}] (Ni[**2**]) and (c) the asymmetric unit and (d) a packing structure viewed from *c* axis in *rac*-[Co(H_2O)$_4$($MeOH$)$_2$][Ni{Au$_2$(dppe)(msa)$_2$}] (Co[**2**]).

Table 2-10. Crystallographic data for $[Ni(H_2O)_4(MeOH)_2][Ni\{Au_2(dppe)(msa)_2\}]\cdot 6H_2O$ ($Ni[\mathbf{2}]\cdot 6H_2O$).

Empirical formula	$C_{36}H_{36}Au_2Cu_2Ni_2O_{23}P_2S_2$
Formula weight	1474.06
Crystal size / mm^3	0.25 × 0.10 × 0.03
Crystal system	Monoclinic
Space group	$P\,2_1/c$
a / Å	10.6970(3)
b / Å	36.3525(8)
c / Å	18.3551(4)
α /°	90
β /°	103.322(7)
γ /°	90
V / $Å^3$	6945.5(3)
Z	4
T / K	200(2)
ρ_{calcd} / $g\cdot cm^{-3}$	1.410
μ(Mo Kα) /mm^{-1}	4.907
$2\theta_{Max}$	55.0
R(int)	0.0375
GOF	1.047
$R1$ ($I>2\sigma(I)$)[a)]	0.0524
w$R2$ (all data)[b)]	0.1676

a) $R1 = \Sigma||F_o|-|F_c|| / \Sigma|F_o|$. b) $wR2 = [\Sigma(w(F_o^2-F_c^2)^2) / \Sigma w(F_o^2)^2]^{1/2}$.

Table 2-11. Bond lengths [Å] and angles [°] for

$[Ni(H_2O)_4(MeOH)_2][Ni\{Au_2(dppe)(msa)_2\}]\cdot 6H_2O$ (Ni[**2**]·$6H_2O$).

	Bond lengths		
Au(1)-P(1)	2.2656(19)	Ni(1)-O(5)	2.062(5)
Au(1)-S(1)	2.3179(19)	Ni(1)-O(7)	2.019(5)
Au(2)-P(2)	2.277(2)	Ni(2)-O(9)	2.056(6)
Au(2)-S(2)	2.316(2)	Ni(2)-O(10)	2.038(7)
Au(1)-Au(2)	2.9486(4)	Ni(2)-O(11)	2.078(7)
Ni(1)-S(1)	2.399(2)	Ni(2)-O(12)	2.047(6)
Ni(1)-S(2)	2.407(2)	Ni(2)-O(13)	2.055(7)
Ni(1)-O(1)	2.071(6)	Ni(2)-O(14)	2.090(6)
Ni(1)-O(3)	2.040(5)		
	Angles		
P(1)-Au(1)-S(1)	177.61(6)	O(5)-Ni(1)-O(7)	92.1(2)
P(2)-Au(2)-S(2)	176.27(7)	O(9)-Ni(2)-O(10)	92.3(3)
S(1)-Ni(1)-S(2)	104.82(8)	O(9)-Ni(2)-O(11)	87.9(3)
S(1)-Ni(1)-O(1)	86.18(16)	O(9)-Ni(2)-O(12)	89.2(3)
S(1)-Ni(1)-O(3)	85.10(15)	O(9)-Ni(2)-O(13)	90.0(3)
S(1)-Ni(1)-O(5)	168.24(18)	O(9)-Ni(2)-O(14)	176.6(2)
S(1)-Ni(1)-O(7)	94.76(18)	O(10)-Ni(2)-O(11)	90.1(3)
S(2)-Ni(1)-O(1)	165.75(16)	O(10)-Ni(2)-O(12)	178.2(3)
S(2)-Ni(1)-O(3)	99.62(16)	O(10)-Ni(2)-O(13)	90.4(3)
S(2)-Ni(1)-O(5)	85.32(18)	O(10)-Ni(2)-O(14)	91.0(3)
S(2)-Ni(1)-O(7)	84.45(18)	O(11)-Ni(2)-O(12)	90.8(3)
O(1)-Ni(1)-O(3)	90.2(2)	O(11)-Ni(2)-O(13)	177.9(3)
O(1)-Ni(1)-O(5)	84.8(2)	O(11)-Ni(2)-O(14)	91.4(3)
O(1)-Ni(1)-O(7)	85.6(2)	O(12)-Ni(2)-O(13)	88.7(3)
O(3)-Ni(1)-O(5)	87.4(2)	O(12)-Ni(2)-O(14)	87.5(2)
O(3)-Ni(1)-O(7)	175.8(2)	O(13)-Ni(2)-O(14)	90.6(3)

Table 2-12. Crystallographic data for $[Co(H_2O)_4(MeOH)_2][Ni\{Au_2(dppe)(msa)_2\}]\cdot 4H_2O$ ($Co[\mathbf{2}]\cdot 4H_2O$).

Empirical formula	$C_{36}H_{36}Au_2CoNiO_{19}P_2S_2$
Formula weight	1410.28
Crystal size / mm^3	0.15 × 0.15 × 0.02
Crystal system	Monoclinic
Space group	$P2_1/c$
a / Å	10.7246(9)
b / Å	36.850(3)
c / Å	18.376(3)
α /°	90
β /°	103.772(9)
γ /°	90
V / $Å^3$	7053.4(14)
Z	4
T / K	200(2)
ρ_{calcd} / $g\cdot cm^{-3}$	1.328
μ(Mo Kα) /mm^{-1}	4.793
$2\theta_{Max}$	55.0
R(int)	0.2246
GOF	1.125
$R1$ ($I>2\sigma(I)$)[a)]	0.1446
w$R2$ (all data)[b)]	0.4517

a) $R1 = \Sigma||F_o|-|F_c|| / \Sigma|F_o|$. b) $wR2 = [\Sigma(w(F_o^2-F_c^2)^2) / \Sigma w(F_o^2)^2]^{1/2}$.

Table 2-13. Bond lengths [Å] and angles [°] for Co[**2**]·4H_2O.

		Bond lengths	
Au(1)-P(1)	2.264(6)	Ni(1)-O(5)	2.078(18)
Au(1)-S(1)	2.300(5)	Ni(1)-O(7)	2.069(15)
Au(2)-P(2)	2.282(6)	Co(1)-O(9)	2.129(16)
Au(2)-S(2)	2.342(6)	Co(1)-O(10)	2.091(19)
Au(1)-Au(2)	2.9473(11)	Co(1)-O(11)	2.046(18)
Ni(1)-S(1)	2.400(6)	Co(1)-O(12)	2.131(16)
Ni(1)-S(2)	2.388(7)	Co(1)-O(13)	2.087(18)
Ni(1)-O(1)	2.066(16)	Co(1)-O(14)	2.120(17)
Ni(1)-O(3)	2.061(13)		
		Angles	
P(1)-Au(1)-S(1)	176.87(19)	O(5)-Ni(1)-O(7)	93.6(7)
P(2)-Au(2)-S(2)	176.8(2)	O(9)-Co(1)-O(10)	94.4(7)
S(1)-Ni(1)-S(2)	105.6(2)	O(9)-Co(1)-O(11)	91.5(7)
S(1)-Ni(1)-O(1)	88.1(5)	O(9)-Co(1)-O(12)	89.5(6)
S(1)-Ni(1)-O(3)	84.7(4)	O(9)-Co(1)-O(13)	87.3(6)
S(1)-Ni(1)-O(5)	168.0(6)	O(9)-Co(1)-O(14)	175.8(7)
S(1)-Ni(1)-O(7)	94.0(4)	O(10)-Co(1)-O(11)	89.1(7)
S(2)-Ni(1)-O(1)	163.9(5)	O(10)-Co(1)-O(12)	176.1(7)
S(2)-Ni(1)-O(3)	100.2(4)	O(10)-Co(1)-O(13)	91.0(7)
S(2)-Ni(1)-O(5)	84.6(5)	O(10)-Co(1)-O(14)	89.8(7)
S(2)-Ni(1)-O(7)	83.2(5)	O(11)-Co(1)-O(12)	91.4(7)
O(1)-Ni(1)-O(3)	89.2(6)	O(11)-Co(1)-O(13)	178.8(7)
O(1)-Ni(1)-O(5)	82.9(7)	O(11)-Co(1)-O(14)	88.1(7)
O(1)-Ni(1)-O(7)	87.5(6)	O(12)-Co(1)-O(13)	88.7(6)
O(3)-Ni(1)-O(5)	87.2(6)	O(12)-Co(1)-O(14)	86.4(7)
O(3)-Ni(1)-O(7)	176.5(6)	O(13)-Co(1)-O(14)	93.1(7)

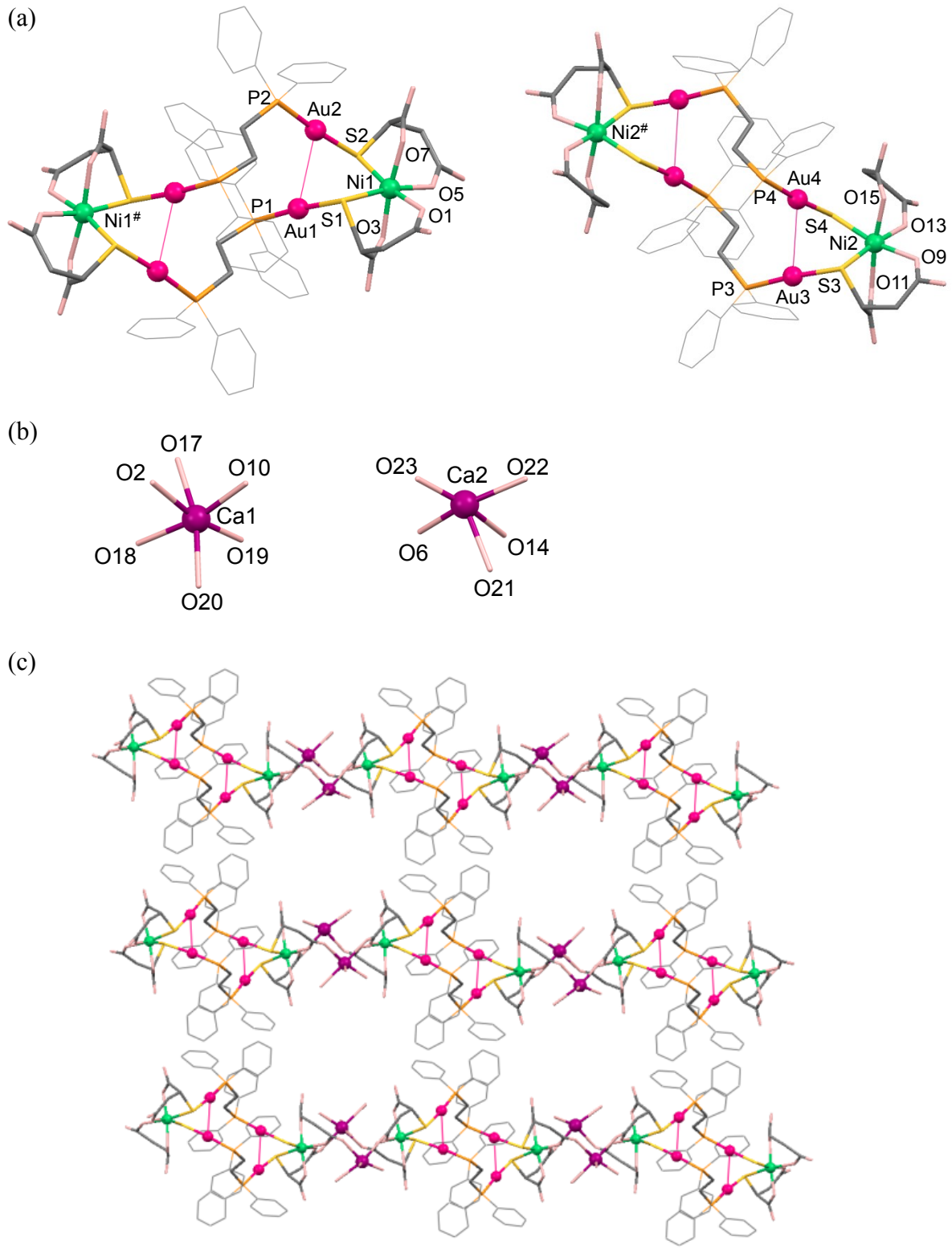

Figure 2-17. Perspective views of (a) two complex anions, (b) two Ca^{II} units, and (c) a packing structure viewed from *a* axis in *meso*-$[Ca_2(H_2O)_7][Ni_2\{Au_2(dppe)(msa)_2\}_2]$ (Ca[**3**]).

Table 2-14. Crystallographic data for $Ca_2[Ni_2\{Au_2(dppe)(msa)_2\}_2]\cdot 12H_2O$ (Ca_2[**3**]$\cdot 12H_2O$).

Empirical formula	$C_{68}H_{68}Au_4Ca_2Ni_2O_{28}P_4S_4$
Formula weight	2570.79
Crystal size / mm^3	0.10 × 0.10 × 0.10
Crystal system	Triclinic
Space group	*P*-1
a / Å	11.2822(16)
b / Å	21.004(3)
c / Å	24.057(3)
α /°	76.607(5)
β /°	81.979(6)
γ /°	86.057(6)
V / $Å^3$	5487.7(14)
Z	2
T / K	200(2)
ρ_{calcd} / $g\cdot cm^{-3}$	1.556
μ(Mo Kα) /mm^{-1}	5.949
$2\theta_{Max}$	52.7
R(int)	0.0339
GOF	1.490
*R*1 (I>2σ(I))[a)]	0.0981
w*R*2 (all data)[b)]	0.2824

a) $R1 = \Sigma||F_o|-|F_c|| / \Sigma|F_o|$. b) $wR2 = [\Sigma(w(F_o^2-F_c^2)^2) / \Sigma w(F_o^2)^2]^{1/2}$.

Table 2-15. Bond lengths [Å] and angles [°] for Ca_2[**3**]·$12H_2O$.

Bond lengths			
Au(1)-P(1)	2.247(4)	Ni(2)-S(4)	2.398(6)
Au(1)-S(1)	2.303(5)	Ni(2)-O(9)	2.121(15)
Au(2)-P(2)	2.258(4)	Ni(2)-O(11)	2.050(13)
Au(2)-S(2)	2.314(4)	Ni(2)-O(13)	2.185(16)
Au(1)-Au(2)	3.1148(8)	Ni(2)-O(15)	2.037(14)
Au(3)-P(3)	2.256(4)	Ca(1)-O(2)	2.50(2)
Au(3)-S(3)	2.307(4)	Ca(1)-O(10)	2.39(2)
Au(4)-P(4)	2.245(4)	Ca(1)-O(17)	2.34(2)
Au(4)-S(4)	2.294(5)	Ca(1)-O(18)	2.482(17)
Au(3)-Au(4)	3.1334(9)	Ca(1)-O(19)	2.12(2)
Ni(1)-S(1)	2.388(6)	Ca(1)-O(20)	2.59(2)
Ni(1)-S(2)	2.413(5)	Ca(2)-O(6)	2.13(2)
Ni(1)-O(1)	2.073(16)	Ca(2)-O(14)	2.43(4)
Ni(1)-O(3)	2.068(13)	Ca(2)-O(21)	2.50(3)
Ni(1)-O(5)	2.086(16)	Ca(2)-O(22)	2.42(2)
Ni(1)-O(7)	2.025(13)	Ca(2)-O(23)	2.00(4)
Ni(2)-S(3)	2.398(5)		
Angles			
P(1)-Au(1)-S(1)	175.12(15)	O(1)-Ni(1)-O(7)	87.2(6)
P(2)-Au(2)-S(2)	175.63(15)	O(3)-Ni(1)-O(5)	85.3(6)
P(3)-Au(3)-S(3)	175.27(16)	O(3)-Ni(1)-O(7)	172.9(5)
P(4)-Au(4)-S(4)	174.89(16)	O(5)-Ni(1)-O(7)	90.2(6)
S(1)-Ni(1)-S(2)	98.28(17)	S(3)-Ni(2)-S(4)	99.25(18)
S(1)-Ni(1)-O(1)	87.4(5)	S(3)-Ni(2)-O(9)	87.7(4)
S(1)-Ni(1)-O(3)	86.4(4)	S(3)-Ni(2)-O(11)	83.3(4)
S(1)-Ni(1)-O(5)	170.4(5)	S(3)-Ni(2)-O(13)	172.7(4)
S(1)-Ni(1)-O(7)	97.7(4)	S(3)-Ni(2)-O(15)	101.4(4)
S(2)-Ni(1)-O(1)	171.0(5)	S(4)-Ni(2)-O(9)	169.4(4)
S(2)-Ni(1)-O(3)	100.1(4)	S(4)-Ni(2)-O(11)	99.2(4)
S(2)-Ni(1)-O(5)	87.9(5)	S(4)-Ni(2)-O(13)	82.1(5)
S(2)-Ni(1)-O(7)	85.1(4)	S(4)-Ni(2)-O(15)	85.4(5)
O(1)-Ni(1)-O(3)	87.2(6)	O(9)-Ni(2)-O(11)	89.5(5)
O(1)-Ni(1)-O(5)	87.4(6)	O(9)-Ni(2)-O(13)	92.1(6)

Table 2-15. (continued).

Angles			
O(9)-Ni(2)-O(15)	85.3(6)	O(17)-Ca(1)-O(20)	165.6(8)
O(11)-Ni(2)-O(13)	89.4(5)	O(18)-Ca(1)-O(19)	100.9(8)
O(11)-Ni(2)-O(15)	172.8(5)	O(18)-Ca(1)-O(20)	86.6(6)
O(13)-Ni(2)-O(15)	85.8(6)	O(19)-Ca(1)-O(20)	86.9(8)
O(2)-Ca(1)-O(10)	83.1(8)	O(6)-Ca(2)-O(14)	80.9(12)
O(2)-Ca(1)-O(17)	68.6(9)	O(6)-Ca(2)-O(21)	89.7(9)
O(2)-Ca(1)-O(18)	88.8(7)	O(6)-Ca(2)-O(22)	166.3(10)
O(2)-Ca(1)-O(19)	167.7(9)	O(6)-Ca(2)-O(23)	78.9(12)
O(2)-Ca(1)-O(20)	101.2(8)	O(14)-Ca(2)-O(21)	66.1(12)
O(10)-Ca(1)-O(17)	86.0(9)	O(14)-Ca(2)-O(22)	85.5(12)
O(10)-Ca(1)-O(18)	168.3(8)	O(14)-Ca(2)-O(23)	156.4(15)
O(10)-Ca(1)-O(19)	86.1(8)	O(21)-Ca(2)-O(22)	86.3(9)
O(10)-Ca(1)-O(20)	103.2(8)	O(21)-Ca(2)-O(23)	125.6(14)
O(17)-Ca(1)-O(18)	83.2(8)	O(22)-Ca(2)-O(23)	114.0(12)
O(17)-Ca(1)-O(19)	104.9(9)		

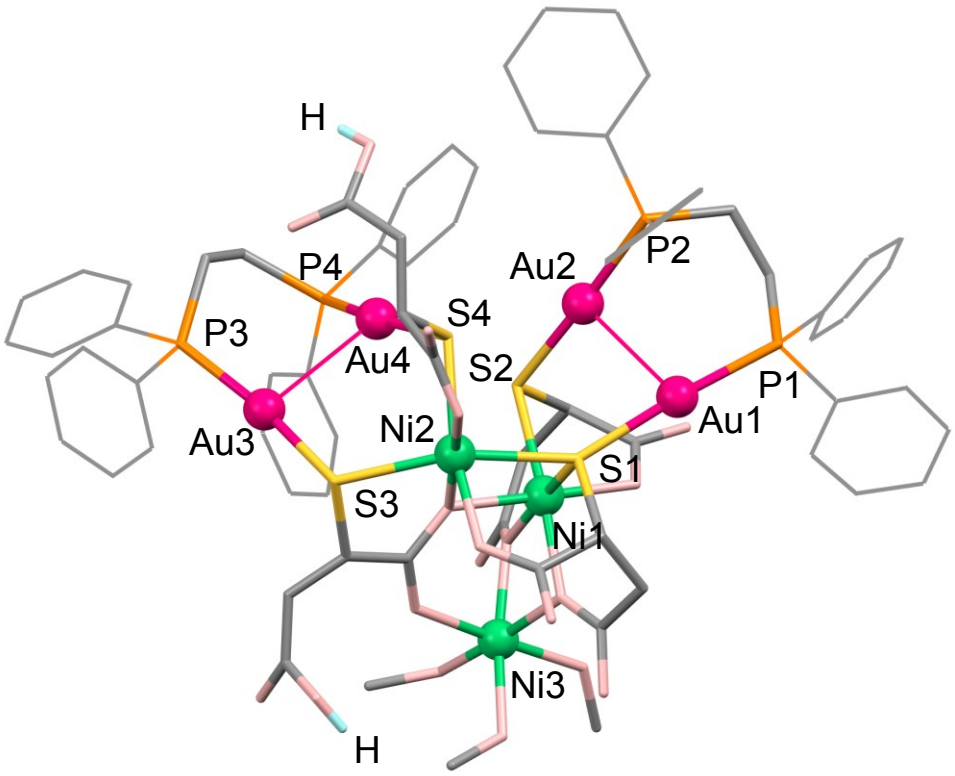

Figure 2-18. A perspective view of the asymmetric unit in $[Ni_3\{Au_2(dppe)(Hmsa)_2\}\{Au_2(dppe)(msa)_2\}(MeOH)_3]\cdot 4MeOH$ ([**4**]).

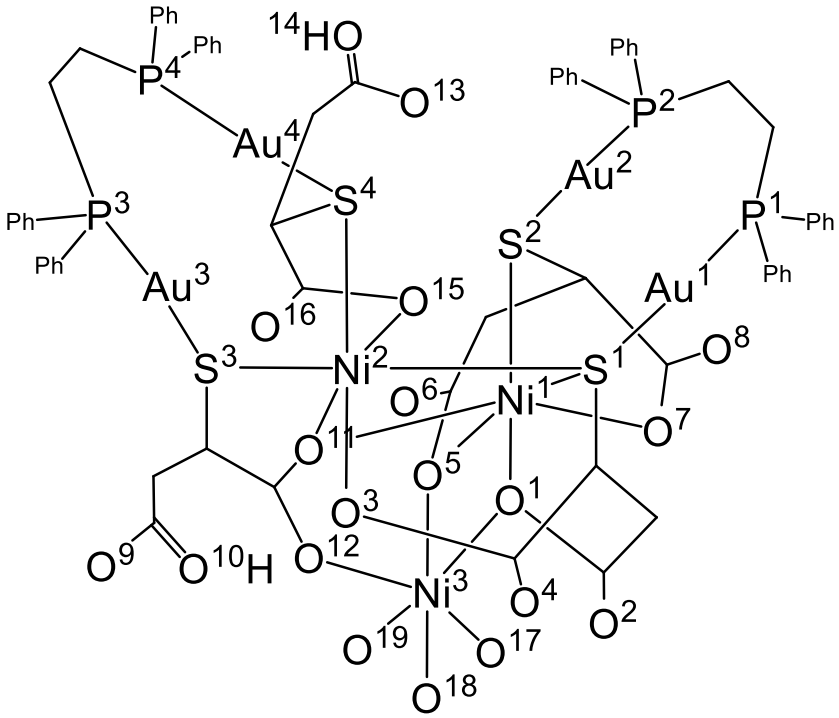

Chart 2-6. A drawing of $[Ni_3\{Au_2(dppe)(Hmsa)_2\}\{Au_2(dppe)(msa)_2\}(MeOH)_3]\cdot 4MeOH$. ([**4**]) with the atomic labelling scheme.

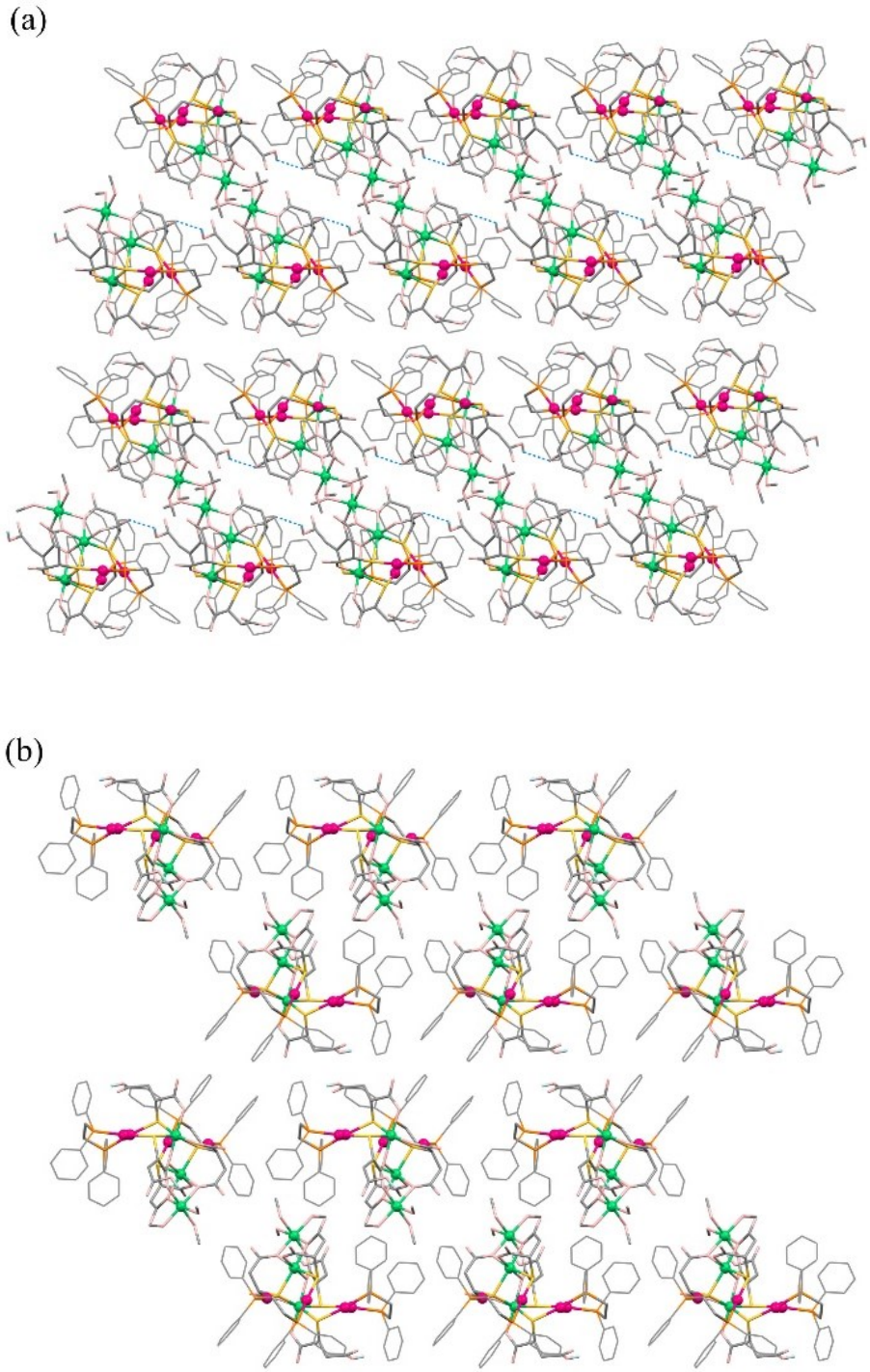

Figure 2-19. Packing structures viewed from (a) *b* axis and (b) *a* axis in $[Ni_3\{Au_2(dppe)(Hmsa)_2\}\{Au_2(dppe)(msa)_2\}(MeOH)_3]\cdot 4MeOH$ ([**4**]·4MeOH).

Table 2-16. Crystallographic data for

$[Ni_3\{Au_2(dppe)(Hmsa)_2\}\{Au_2(dppe)(msa)_2\}(MeOH)_3]\cdot 4MeOH$ ([**4**]).

Empirical formula	$C_{76}H_{93}Au_4Ni_3O_{24}P_4S_4$
Formula weight	2606.61
Crystal size / mm^3	0.10 × 0.01 × 0.01
Crystal system	Triclinic
Space group	*P*-1
a / Å	11.8932(5)
b / Å	16.9404(7)
c / Å	23.2709(9)
α /°	84.250(6)
β /°	78.433(5)
γ /°	71.558(5)
V / $Å^3$	4354.0(3)
Z	2
T / K	200(2)
ρ_{calcd} / $g\cdot cm^{-3}$	2.022
μ(Mo Kα) /mm^{-1}	7.716
$2\theta_{Max}$	55.0
R(int)	0.0606
GOF	1.050
*R*1 (I>2σ(I))[a)]	0.0683
w*R*2 (all data)[b)]	0.1266

a) $R1 = \Sigma||F_o|-|F_c|| / \Sigma|F_o|$. b) $wR2 = [\Sigma(w(F_o^2-F_c^2)^2) / \Sigma w(F_o^2)^2]^{1/2}$.

Table 2-17. Bond lengths [Å] and angles [°] for [**4**].

Bond lengths			
Au(1)-P(1)	2.272(3)	Ni(1)-O(7)	2.059(7)
Au(1)-S(1)	2.332(3)	Ni(1)-O(11)	2.073(7)
Au(2)-P(2)	2.288(3)	Ni(2)-S(1)	2.478(3)
Au(2)-S(2)	2.335(3)	Ni(2)-S(3)	2.413(3)
Au(1)-Au(2)	3.0530(7)	Ni(2)-S(4)	2.373(3)
Au(3)-P(3)	2.282(3)	Ni(2)-O(3)	2.031(7)
Au(3)-S(3)	2.336(3)	Ni(2)-O(11)	2.151(8)
Au(4)-P(4)	2.255(3)	Ni(2)-O(15)	2.059(9)
Au(4)-S(4)	2.302(3)	Ni(3)-O(1)	2.055(8)
Au(3)-Au(4)	3.0135(6)	Ni(3)-O(5)	2.068(7)
Ni(1)-S(1)	2.405(3)	Ni(3)-O(12)	2.051(8)
Ni(1)-S(2)	2.396(3)	Ni(3)-O(17)	2.058(8)
Ni(1)-O(1)	2.072(7)	Ni(3)-O(18)	2.091(8)
Ni(1)-O(5)	2.073(8)	Ni(3)-O(19)	2.053(9)
Angles			
P(1)-Au(1)-S(1)	175.41(11)	O(1)-Ni(1)-O(5)	79.6(3)
P(2)-Au(2)-S(2)	176.90(10)	O(1)-Ni(1)-O(7)	93.6(3)
P(3)-Au(3)-S(3)	169.68(11)	O(1)-Ni(1)-O(11)	87.6(3)
P(4)-Au(4)-S(4)	170.08(11)	O(5)-Ni(1)-O(7)	87.9(3)
S(1)-Ni(1)-S(2)	97.33(11)	O(5)-Ni(1)-O(11)	90.4(3)
S(1)-Ni(1)-O(1)	92.8(2)	O(7)-Ni(1)-O(11)	177.7(3)
S(1)-Ni(1)-O(5)	170.2(2)	S(1)-Ni(2)-S(3)	158.99(13)
S(1)-Ni(1)-O(7)	98.9(2)	S(1)-Ni(2)-S(4)	92.06(10)
S(1)-Ni(1)-O(11)	83.0(2)	S(1)-Ni(2)-O(3)	80.4(2)
S(2)-Ni(1)-O(1)	169.8(2)	S(1)-Ni(2)-O(11)	79.7(2)
S(2)-Ni(1)-O(5)	90.2(2)	S(1)-Ni(2)-O(15)	102.0(3)
S(2)-Ni(1)-O(7)	85.3(2)	S(3)-Ni(2)-S(4)	98.76(11)
S(2)-Ni(1)-O(11)	93.2(2)	S(3)-Ni(2)-O(3)	92.5(2)

Table 2-17. (continued).

Angles			
S(3)-Ni(2)-O(11)	80.1(2)	O(1)-Ni(3)-O(19)	172.0(3)
S(3)-Ni(2)-O(15)	97.5(3)	O(5)-Ni(3)-O(12)	88.7(3)
S(4)-Ni(2)-O(3)	165.3(3)	O(5)-Ni(3)-O(17)	89.4(3)
S(4)-Ni(2)-O(11)	105.2(2)	O(5)-Ni(3)-O(18)	172.2(4)
S(4)-Ni(2)-O(15)	80.9(2)	O(5)-Ni(3)-O(19)	92.6(3)
O(3)-Ni(2)-O(11)	86.0(3)	O(12)-Ni(3)-O(17)	177.9(3)
O(3)-Ni(2)-O(15)	88.4(3)	O(12)-Ni(3)-O(18)	94.6(3)
O(11)-Ni(2)-O(15)	173.7(3)	O(12)-Ni(3)-O(19)	93.7(3)
O(1)-Ni(3)-O(5)	80.2(3)	O(17)-Ni(3)-O(18)	87.2(3)
O(1)-Ni(3)-O(12)	89.6(3)	O(17)-Ni(3)-O(19)	87.4(4)
O(1)-Ni(3)-O(17)	89.1(3)	O(18)-Ni(3)-O(19)	94.2(4)
O(1)-Ni(3)-O(18)	92.8(3)		

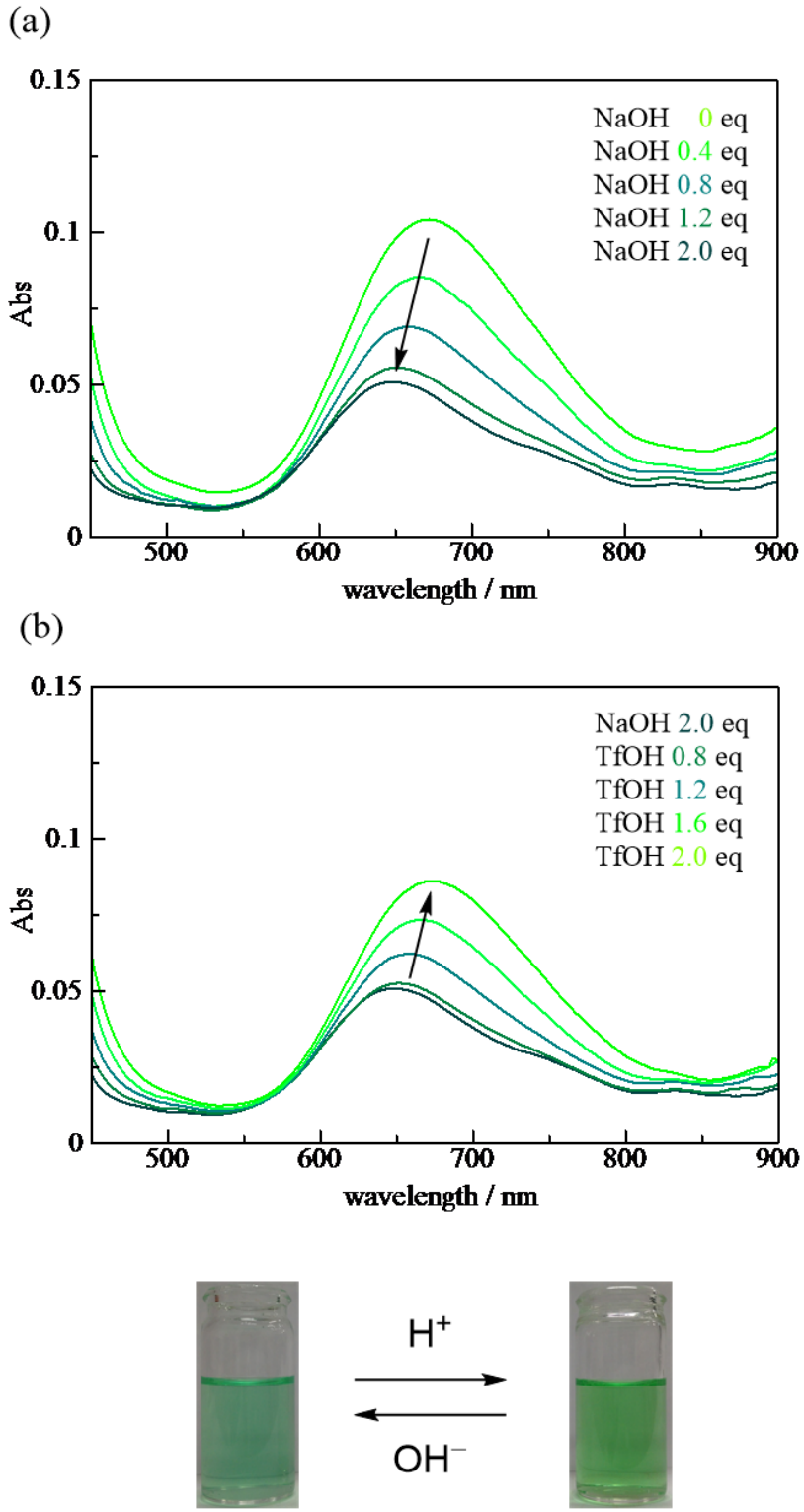

Figure 2-20. (a) UV-vis absorbance spectral change of a reaction mixture containing [H_4**1**], $Ni(ClO_4)_2$, and NaOH in a 1 : 1 : 2 ratio titrated with NaOH (from 0 to 2 equiv.) in MeOH, and (b) that after titration with TfOH (from 0 to 2 equiv.) in MeOH.

(a)

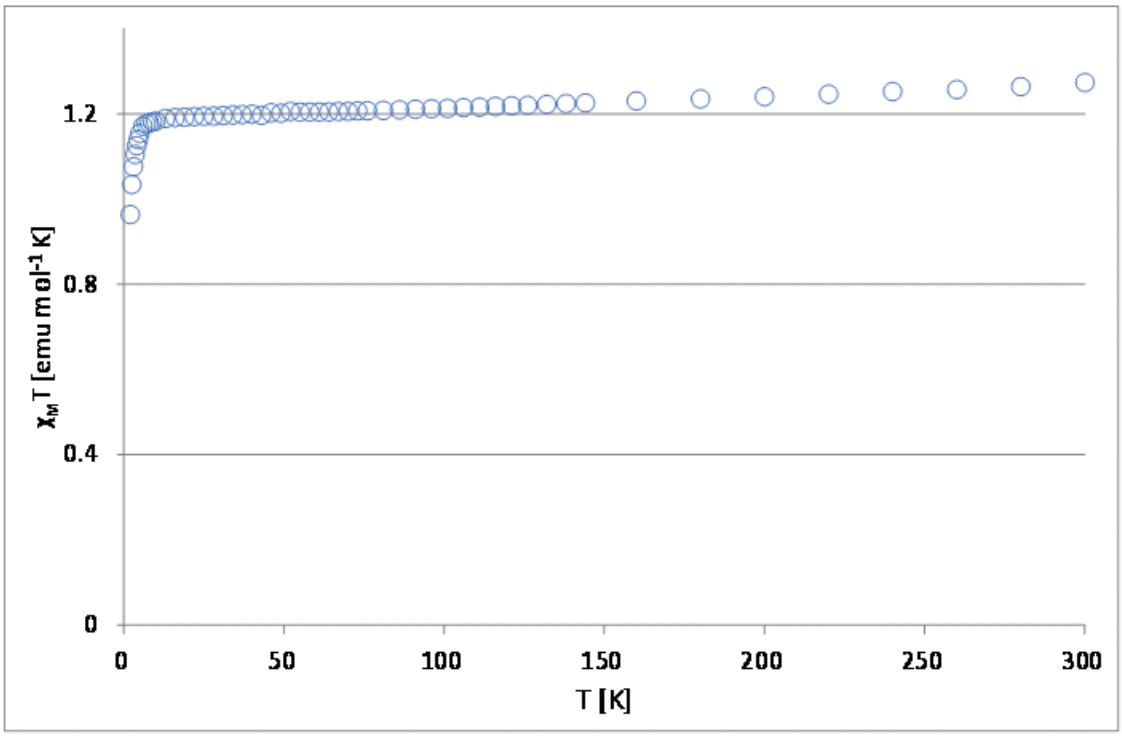

(b)

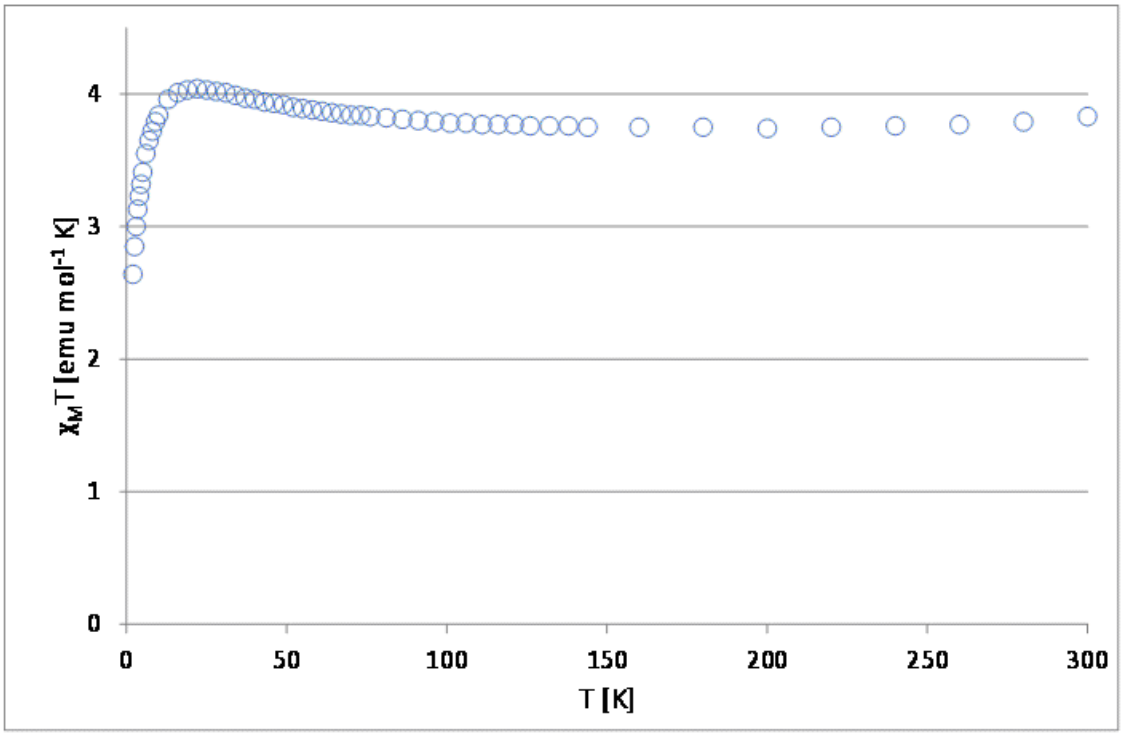

Figure 2-21. The $\chi_M T$ vs T plots of (a) Mg[**2**] and (b) [**4**].

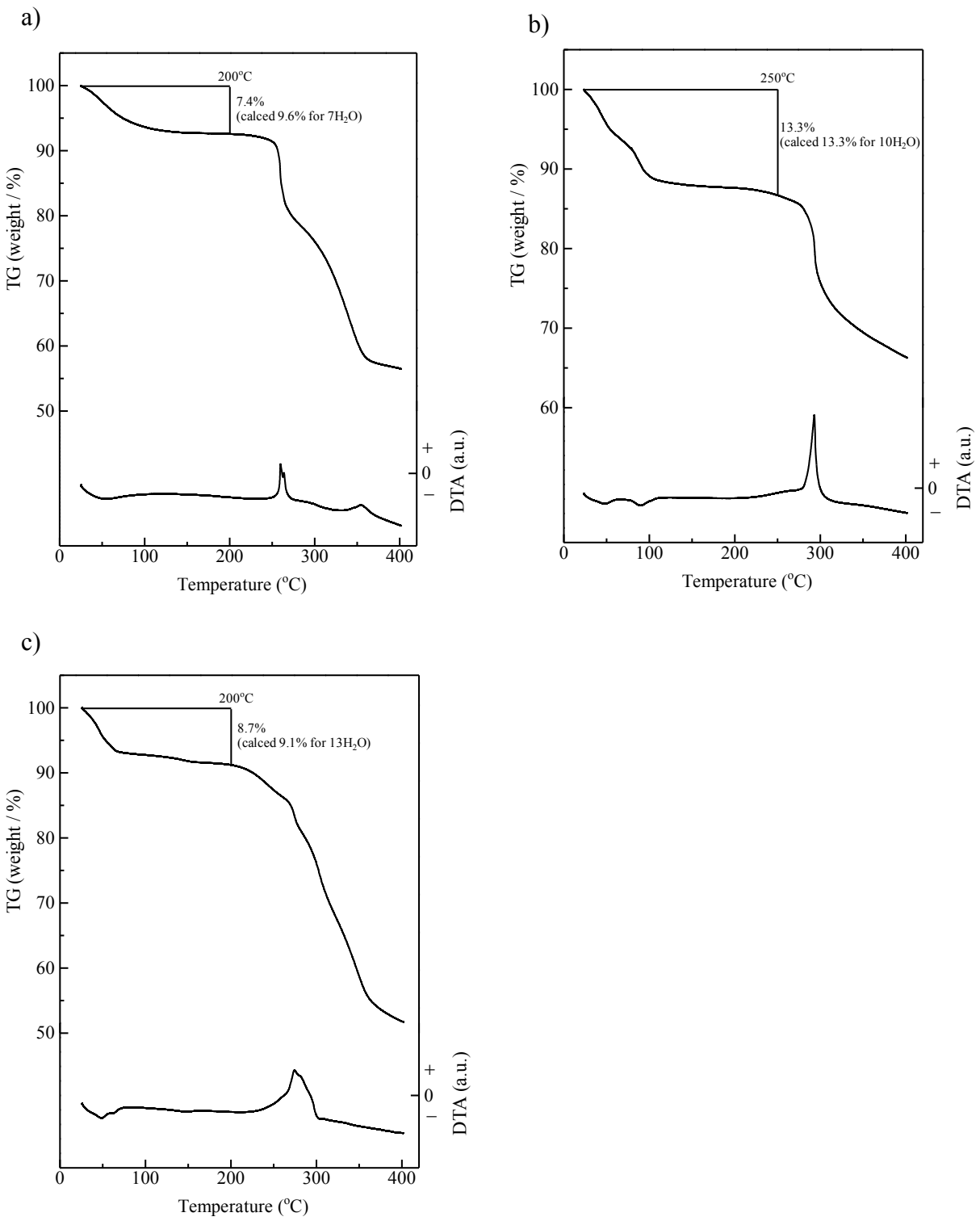

Figure 2-22. Thermogravimetric (TG) and differential thermal analysis (DTA) curves of (a) Na_2[**2**], (b) Mg[**2**], and (c) [**4**].

Chapter III. Cage-type Digold(I) Complexes with Bis(diphenylphosphino)methane

III-1. Introduction

Chromic luminescent compounds whose emission energies and intensities change in response to external stimuli have received increasing attention because of their potential applications as chemical/biological probes and organic light-emitting diodes.[39] These compounds often involve Au^I ions as a metal component,[40-45] in which their photo-luminescence is highly sensitive to the change in intramolecular and intermolecular Au···Au aurophilic interactions.[16] Thus far, organic vapors,[40] solvents,[41] counter anions,[42] metal ions,[12b] temperature,[43] and mechanical force[44] have been used as triggers to change the emission colors and intensities of gold(I) compounds. Generally, each Au^I center of these compounds has a 2-coordinated linear geometry.[5a, 17, 45] This geometry enables them to form an effective Au···Au interaction and to accept another donor that exists as a counter ion or solvent molecule to their vacant coordination sites. In contrast, the chromic behavior has not been reported for those containing 3-coordinated, trigonal-planar Au^I centers.[46] This is surprising because 3-coordinated gold(I) species are expected to show a stronger photo-luminescence due to the steric crowdedness around each Au^I center, which can inhibit non-radiative processes.[47] In this context, the investigation of the photo-luminescent properties of a typical digold(I) complex, $[Au_2(dppm)_3]^{2+}$ (dppm = bis(diphenylphosphino)metane, $[\mathbf{5}]^{2+}$), in which two Au^I centers are triply bridged by three dppm ligands, was started. This complex was prepared and isolated as bromide and perchlorate salts by McAuliffe and coworkers in 1985, who proposed that each Au^I center in $[\mathbf{5}]^{2+}$ has a trigonal-planar geometry based on the ^{31}P NMR spectroscopic and elemental analytical results.[18] However, its crystal structure and emission property have not yet been investigated.

In this study, the crystallization and structural characterization of the chloride and trifluoromethanesulfonate (OTf^-) salts of $[\mathbf{5}]^{2+}$ were successfully carried out. In the solid state, both salts exhibit a quite brilliant emission, green for the chloride salt, and yellow-green for the OTf^-salt, with a quantum yield of >95%. More remarkably, a reversible, two-step emission color change from green to blue via yellow, induced by the loss of water molecules of crystallization with the subsequent loss of one of three bridging dppm ligands to form $[Au_2(dppm)_2]^{2+}$ ($[\mathbf{6}]^{2+}$), was detected for the chloride salt in the solid state (Scheme 3-1). To our knowledge, such a fascinating chromic luminescence has never been reported for gold(I) compounds with trigonal-planer Au^I centers.

III-2. Experimental section.

III-2-1. Materials.

A digold(I) complex, $[Au_2(dppm)Cl_2]$, was prepared according to literature method.[34] All reagents and solvents used in synthetic studies were commercially available and used as supplied without further purification.

III-2-2. Synthesis of $[Au_2(dppm)_3]Cl_2 \cdot 8.5H_2O$ ($[5]Cl_2 \cdot 8.5H_2O$).

To a white suspension containing 50 mg (0.059 mmol) of $[Au_2(dppm)Cl_2]$ in MeOH (5 mL) was added a solid sample of dppm (46 mg, 0.12 mmol). The mixture was sonicated for 1 min, producing a clear yellow solution. H_2O (2 mL) was added to the yellow solution, which was allowed to stand at room temperature for 5 days. The resulting pale yellow block crystals suitable for X-ray analysis were collected via filtration. Yield: 88 mg (85%). Anal. Found: C, 50.88; H, 4.65%. Calcd for $[Au_2(dppm)_3]Cl_2 \cdot 8.5H_2O = C_{75}H_{83}O_{8.5}P_6Au_2Cl_2$: C, 50.86; H, 4.72%. IR spectrum (cm^{-1}, KBr disk): 1436 (ν_{Ph}), 1097, 784, and 694 (ν_{P-Ph}). ^1H NMR spectrum (ppm from TMS, CD_3OD): 7.52–7.39 (m, 8H), 7.36 (t, 4H, J = 7.4 Hz), 7.19 (t, 8H, J = 7.6 Hz). ^{31}P NMR spectrum (ppm from 80% H_3PO_4, CD_3OD): 28.476.

III-2-3. Synthesis of $[Au_2(dppm)_3](OTf)_2 \cdot H_2O$ ($[5](OTf)_2 \cdot H_2O$).

To a white suspension containing 50 mg (0.059 mmol) of $[Au_2(dppm)Cl_2]$ in MeOH (5 mL) was added a solid sample of dppm (46 mg, 0.12 mmol). The mixture was sonicated for 1 min, producing a clear yellow solution. A solution containing 25 mg (0.145 mmol) of NaOTf in a mixture of H_2O (1 mL) and MeOH (7 mL) was added to the yellow solution, followed by allowing it to stand at room temperature for 2 days. The resulting pale-yellow plate crystals suitable for X-ray analysis were collected via filtration. Yield: 97 mg (88%). Anal. Found: C, 49.86; H, 3.69%. Calcd for $[Au_2(dppm)_3](OTf)_2 \cdot H_2O = C_{77}H_{68}O_7S_2P_6Au_2F_6$: C, 49.64; H, 3.68%. IR spectrum (cm^{-1}, KBr disk): 1436 (ν_{Ph}), 1260 (ν_{SO3}), 1097, 775, and 693 (ν_{P-Ph}).

III-2-4. Thermal conversion of $[5]Cl_2 \cdot 8.5H_2O$.

A pale yellow crystalline powder of [**5**]$Cl_2 \cdot 8.5H_2O$ was heated at 373 K for 30 min under vacuum to produce a dehydrated sample of [**5**]Cl_2. During heating, the color of the powder changed from pale-yellow to yellow. The dehydrated sample of [**5**]Cl_2 was further heated at 399 K for 30 min. During the second heating, the color of the powder changed from yellow to white ([**6**]Cl_2). The samples thus obtained were used for the emission and powder X-ray diffraction measurements at ambient temperature.

III-2-5. Physical measurements.

The IR spectra were recorded on a JASCO FT/IR-4100 infrared spectrophotometer using KBr disks at room temperature. The elemental analysis (C, H) was performed at Osaka University using YANACO CHN coda MT-5 or MT-6. The ^{1}H and ^{31}P NMR spectra in solution were measured on a JEOL EX-500 spectrometer at the probe temperature, using tetramethylsilane (TMS, δ 0.0 ppm) as the internal standard for ^{1}H NMR measurements and triphenyl phosphate (δ −17.6 ppm) as the external standard for ^{31}P NMR measurements. The MAS ^{31}P NMR spectra in solid state were measured on a Chemagnetics CMX300 spectrometer at the probe temperature and spin at 7 kHz for [**5**]$Cl_2 \cdot 8.5H_2O$, and at 6 kHz for [**5**]Cl_2 and [**6**]Cl_2, using triphenyl phosphate as the external standard. Thermal gravity (TG) and differential thermal analysis (DTA) measurements were measured on a SHIMADZU DTG-60 analyzer. The powder X-ray diffraction pattern were recorded on BRUKER D2 PHASER room temperature. High quality powder X-ray diffraction pattern for structural determination were recorded at room temperature, in transmission mode [synchrotron radiation λ = 1.3 Å; 2θ range = 0–78°; step width = 0.01°; data collection time = 5 min] on a diffractometer equipped with a blue imaging plate detector at SPring-8 BL19B2 beamline with the approval of the Japan Synchrotron Radiation Research Institute (JASRI) (Proposal No. 2014B1022). The crystals were put into 0.3 mm glass capillary tubes. The samples were rotated during the measurements. The diffraction patterns were collected with a large Debye−Scherrer camera. The powder simulation patterns were generated from the single-crystal X-ray structures using Mercury 3.0.

III-2-6. Luminescence measurements.

The luminescence spectra were recorded by a JASCO FP-8500 spectrometer at room temperature in the solid state or in solution, using a Xe lamp as the light source. The internal emission quantum yields (Φ) were obtained via the absolute measuring method using an integrating sphere unit (JASCO ILFC-847), the internal surface of which was coated with highly reflective Spectralon. The ESC-842 Calibrated light source (WI) and the ESC-843 Calibrated light source (D2) were used to calibrate the emission intensities to measure the absolute quantum yields. The accuracy of this instrument was confirmed using a Rhodamine B ethylene glycol solution. The measurement was performed according to the following protocol. First, nothing was set on the sample cell holder in the integrating sphere, and then, the spectrum of the incident light was measured. The observed peak area was defined as the area from incident light, A_0 (equivalent number of photons in the incident light). Second, the sample on the sample holder was set in the integrating sphere, and the emission spectra of the sample were measured. The obtained excitation wavelength peak area was defined as the area scattered from

the sample, A_1 (equivalent number of photons that were not absorbed), and peak area in the emission wavelength range was defined as the area emitted from the sample, A_2. Finally, the internal emission quantum yields (Φ) were calculated using the following equation: $\Phi = A_2/(A_0 - A_1)$. The Φ values for more than 10 samples of [**5**]$Cl_2 \cdot 8.5H_2O$ or [**5**]$(OTf)_2 \cdot H_2O$ have been measured. As a result, the observed Φ values varied in the range of 99–104% for [**5**]$Cl_2 \cdot 8.5H_2O$ and 99–101% for [**5**]$(OTf)_2 \cdot H_2O$. The fluctuations in the Φ values (maximum of 5%) should be regarded as the random error of measurements. In addition, the absolute quantum yields of Quinine sulfate in a degassed 0.5 M H_2SO_4 using the same instrument and the same sample cell have been measured in order to evaluate the accuracy of the absolute quantum yields observed by the instrument. The observed quantum yield values of 55–57% were in good agreement with the reported value of 55%.[48] Considering aforementioned results, the observed Φ values contain 5% error. Emission lifetime measurements were recorded using a Hamamatsu Photonics, C4334 system equipped with a streak camera as a photo detector and a nitrogen laser for the 337 nm excitation. The data of the emission data are summarized in Table 3-1.

III-2-7. X-ray structural determinations.

The single crystal X-ray diffraction measurements.

The single crystal X-ray diffraction measurements were performed using a Rigaku FR-E Superbright rotating-anode X-ray source with Mo-target (λ = 0.71075 Å), equipped with a Rigaku RAXIS VII imaging plate as a detector, at 200 K. The intensity data were collected via the ω-scan technique and empirically corrected for absorption. The structures of the complexes were solved by direct methods using SHELXS201425. The structure refinements were carried out using full matrix least-squares (SHELXL2014).[49] The data are summarized in Table 3-2.

For [**5**]$Cl_2 \cdot 8.5H_2O$, one third of the $[Au_2(dppm)_3]^{2+}$ cation, two thirds of the Cl^- anion, and two and five sixths of the H_2O molecules were crystallographically independent. All dppm ligands in the crystal were disordered at two positions, with an occupancy factor of 0.5. All of the benzene rings of dppm ligands were treated using AFIX 66 constraints and SIMU restraints. Some EADP restraints were applied to model the disordered chlorine and water molecules. All non-hydrogen atoms, except water molecules, were refined anisotropically. Hydrogen atoms were included in the calculated positions, except those of H_2O molecules. For [**5**]$(OTf)_2 \cdot H_2O$, two $[Au_2(dppm)_3]^{2+}$ cations, four OTf^- anions, and two water molecules were crystallographically independent. All of the benzene rings of dppm ligands were treated using AFIX 66 constraints. All non-hydrogen atoms, except one OTf^- anion, one benzene ring, and one water molecule, which were disordered into two parts with occupancy factors of 0.5, were refined anisotropically. Hydrogen atoms were included in the calculated positions. Three of the

four OTf^- anions were modeled to adopt ideal conformations using FRAG commands. These anions were treated using EADP or DELU restraints.

Ab Initio crystal structure determination of [6]Cl_2

A high-quality PXRD pattern of [**6**]Cl_2 was recorded at 298 K in transmission mode [0.3 mm capillary; synchrotron radiation $\lambda = 1.3$ Å; 2θ range, 0.00 to 78.09°; step size, 0.01°; data collection time, 25 min] using a diffractometer equipped with a blue imaging plate detector at the BL19B2 beam line, SPring-8.

The PXRD pattern of [**6**]Cl_2 was indexed using the program DICVOL[50] to produce a monoclinic unit cell ($a = 20.588$ Å, $b = 18.129$ Å, $c = 12.988$ Å, $\beta = 98.892°$, $V = 4789.27$ Å^3) with good figure of merit. The space group was assigned based on systematic absences as $P2_1/n$. Unit cell and profile refinement were carried out using the Pawley method and led to a good fit ($\chi^2 = 3.87$) for these lattice parameters and the space group. The structure solution was obtained using the simulated annealing method with the program DASH[51]. Two rigid groups: [$Au_2(dppm)_2$], in which P-C phenyl were allowed to rotate, and two Cl^- molecules, in asymmetric units and $Z = 4$ for space group $P2_1/n$, were introduced using a constrained Z-matrix description. During annealing, 26 runs of 1 × 107 Monte Carlo moves were performed. The best structure obtained (Profile $\chi^2 = 24.45$) was taken as the starting structural model for Rietveld refinement. The Rietveld refinement[52] of [**6**]Cl_2 was performed using the programs RIETAN-FP[53] and VESTA[54], introducing disorder for each Cl^- anion. Restraints but no constraints for all bond lengths were employed to maintain the molecular geometry. Atomic displacement parameters were refined isotopically. Absorption collection was applied using the RIETAN-FP Program. Final Rietveld refinement result: $a = 20.5723(6)$ Å, $b = 18.1157(5)$ Å, $c = 12.975(3)$ Å, $\beta = 98.900(2)°$, $V = 4777.5(2)$ Å^3, $R_{wp} = 8.860\%$ ($R_e = 10.850\%$), $R_p = 6.403\%$, $R_B = 6.775\%$, $R_F = 6.605\%$; 5,801 profile points (2θ range, 2 to 60°); 282 refined variables. The result is shown in Figure 3-17.

Ab Initio crystal structure determination of [$Au_2(dppm)_2Cl_2$]

A high-quality PXRD pattern of [$Au_2(dppm)_2Cl_2$], which was prepared from [$Au_2(dppm)_2Cl_2$]·(acetone) after being heated at 399 K, was recorded at 298 K in transmission mode [0.3 mm capillary; synchrotron radiation $\lambda = 1.3$ Å; 2θ range, 0.00 to 78.09°; step size, 0.01°; data collection time, 20 min] using a diffractometer equipped with a blue imaging plate detector at the BL19B2 beam line, SPring-8.

The PXRD pattern of [$Au_2(dppm)_2Cl_2$] was indexed using the program DICVOL[50] to produce a triclinic unit cell ($a = 20.481$ Å, $b = 14.008$ Å, $c = 11.237$ Å, $\alpha = 66.65°$, $\beta = 109.83°$,

$\gamma = 125.98°$, $V = 2370.44$ Å^3) with good a figure of merit. The space group was assigned as *P*-1 based on systematic absences. Unit cell and profile refinement were carried out using the Pawley method and led to a good fit ($\chi^2 = 3.10$) for these lattice parameters and the space group. The structure solution was carried out using the simulated annealing method with the program DASH.[51] Two rigid groups: [Au(dppm)]Cl, in which P-C phenyl were allowed to rotate in an asymmetric unit and $Z = 2$ for space group *P*-1, were introduced using a constrained Z-matrix description. During annealing, 26 runs of 1 × 107 Monte Carlo moves were performed. The best structure obtained (Profile $\chi^2 = 20.92$) was taken as the starting structural model for Rietveld refinement. Absorption collection was applied using the RIETAN-FP Program. The Rietveld refinement[52] of $[Au_2(dppm)_2Cl_2]$ was performed using the programs RIETAN-FP[53] and VESTA[54]. Restraints but no constraints for all bond lengths were employed to maintain the molecular geometry. Atomic displacement parameters were refined isotopically. Final Rietveld refinement result: $a = 20.4758(0)$ Å, $b = 14.0049(0)$ Å, $c = 11.2323(0)$ Å, $\alpha = 66.63(0)°$, $\beta = 109.68(0)°$, $\gamma = 125.96(0)°$, $V = 2368.42(0)$ Å^3, $R_{wp} = 5.150\%$ ($R_e = 10.504\%$), $R_p = 3.908\%$, $R_B = 1.505\%$, $R_F = 0.794\%$; 5,701 profile points (2θ range, 3 to 60°); 242 refined variables. The result is shown in Figure 3-18.

III-2-8. DFT calculations.

DFT calculations for the [**5**]$Cl_2 \cdot H_2O$ system were performed using the Gaussian 09 program[55] with the PBE0 functional. The def2-tzvppd basis set was applied for Au and P atoms in [**5**]$^{2+}$. 6–311G(d) basis sets were applied for bridging C atoms between two P atoms in [**5**]$^{2+}$, and 6–31G and STO-3G basis sets were applied for C and H atoms in phenyl rings in [**5**]$^{2+}$, respectively. Additionally, 6–311+G* basis sets for Cl^- and H_2O molecules were used. The single-point and time-dependent DFT calculations were carried out for [**5**]$Cl_2 \cdot H_2O$. The initial structural parameters were taken from the single-crystal X-ray structure of [**5**]$Cl_2 \cdot 8.5H_2O$. The contour plots of HOMO-12, HOMO-11 and LUMO are shown in Figure 3-8. The calculated absorption spectrum of [**5**]$Cl_2 \cdot H_2O$ is illustrated in Figure 3-9. The major components in the calculated absorption spectrum were summarized in Table 3-3. The optimized molecular structures in the singlet ground state and triplet excitation state are demonstrated in Supplementary Figure 3-13.

III-3. Results and Discussion.

III-3-1. Synthesis and Characterization of Complexes

a) $[Au^I_2(dppm)_3]Cl_2 \cdot 8.5H_2O$ ([5]$Cl_2 \cdot 8.5H_2O$).

Treatment of $[Au_2(dppm)Cl_2]$ with dppm at a 1:2 ratio in $MeOH/H_2O$ produced a clear yellow solution, from which the chloride salt of $[\mathbf{5}]^{2+}$ ([**5**]$Cl_2 \cdot 8.5H_2O$) was isolated as pale yellow block crystals at a high yield. The elemental and thermogravimetric (TG) analytical data implied that freshly prepared crystals of the chloride salts contained 8.5 water molecules per one complex cation (Figure 3-1). The presence of water molecules was confirmed by IR spectroscopy, showing a broad band at approximately 3400 cm^{-1} (Figure 3-2).[37] The ^1H NMR spectrum of [**5**]Cl_2 in metanol-d_4 showed a multiplet signal derived from phenyl groups at δ 7.52-7.39, a triplet signal at δ 7.36 (J = 7.4 Hz), and a triplet signal at δ 7.19 (J = 7.6 Hz) in an integral intensity ratio of 8:4:8 (Figure 3-3). The ^{31}P NMR spectrum in metanol-d_4 showed a singlet signal at δ 28.476 (Figure 3-4).

Single-crystal X-ray crystallography indicated that [**5**]$Cl_2 \cdot 8.5H_2O$ is crystallized in a cubic space group *Pa*-3, consisting of one third of the complex cation of $[\mathbf{5}]^{2+}$, two thirds of chloride anions, and two and five sixths of water molecules of crystallization in the asymmetric unit. The entire complex cation contains two Au^I ions that are triply bridged by three dppm ligands, forming a digold(I) structure in $[Au_2(dppm)_3]^{2+}$ (Figure 3-5). Each Au^I ion, which lies on a crystallographic C_3 axis, is coordinated by three P atoms from three different dppm ligands in an ideal trigonal-planar geometry (av. Au–P = 2.41 Å and P–Au–P = 120°). This triply bridged structure in $[\mathbf{5}]^{2+}$ is reminiscent of that found in the corresponding disilver(I) complex, $[Ag_2(dppm)_3]^{2+}$.[56] The intramolecular separation between two Au^I centers in [**5**]$Cl_2 \cdot 8.5H_2O$ is 3.03 Å, suggestive of the presence of an aurophilic interaction. In crystal, there exist intermolecular CH···π interactions between complex cations (C···Ph = 3.07-3.50 Å). Moreover, two Cl^- counter anions and water molecules of crystallization are located around each complex cation, forming CH···Cl (C···Cl = 3.56-3.81 Å) and OH···Cl (O···Cl = 2.91-2.96 Å) interactions.

b) $[Au^I_2(dppm)_3](OTf)_2 \cdot H_2O$ ([5]$(OTf)_2 \cdot H_2O$).

The OTf^- salt of $[\mathbf{5}]^{2+}$ ([**5**]$(OTf)_2 \cdot H_2O$) was also obtained as pale yellow platelet crystals by adding NaOTf to the reaction solution of [**5**]Cl_2. The elemental and thermogravimetric (TG) analytical data implied that freshly prepared crystals of OTf^- salts also contained one water molecule per one complex cation (Figure 3-1). The presence of water molecules was confirmed by IR spectroscopy, showing a broad band at approximately 3400 cm^{-1} (Figure 3-2).

Single-crystal X-ray analysis indicated that [**5**]$(OTf)_2 \cdot H_2O$ is crystallized in a monoclinic space group $P2_1/n$, consisting of two complex cations of $[\mathbf{5}]^{2+}$ (av. Au–P = 2.39 Å and av. P–Au–P = 120°), four OTf^- anions, and two water molecules of crystallization in the asymmetric unit. The digold(I) structure of each complex cation in this compound is nearly the same as that found in [**5**]$Cl_2 \cdot 8.5H_2O$ (Figure 3-5). The intramolecular separations between two Au^I centers in the two complex cations are 2.97 and 2.99 Å, which are slightly shorter than the separation in [**5**]$Cl_2 \cdot 8.5H_2O$ (3.03 Å). The relatively strong CH···O/F (C···O = 3.06-3.30 Å, C···F = 3.18-3.58 Å) interactions between a complex cation and OTf^- anion, as well as intermolecular CH···π interactions between complex cations (C···Ph = 3.17-3.61 Å), are found in [**5**]$(OTf)_2 \cdot H_2O$.

III-3-2. Photoluminescence behavior of [5]$Cl_2 \cdot 8.5H_2O$ and [5]$(OTf)_2 \cdot H_2O$.

Under UV light irradiation at room temperature, solid samples of [**5**]$Cl_2 \cdot 8.5H_2O$ and [**5**]$(OTf)_2 \cdot H_2O$ showed strong green and yellow-green emissions, respectively (Figure 3-6). In the emission spectra, [**5**]$Cl_2 \cdot 8.5H_2O$ and [**5**]$(OTf)_2 \cdot H_2O$ showed broad bands centered at 413 and 440 nm, respectively. The emission lifetimes for [**5**]$Cl_2 \cdot 8.5H_2O$ and [**5**]$(OTf)_2 \cdot H_2O$ were estimated to be 4.51 μs and 4.15 μs, respectively (Figure 3-7), indicative of the phosphorescent character of emission for both compounds. Time-dependent density functional theory (TD-DFT) calculations of [**5**]$Cl_2 \cdot H_2O$ showed intense absorption at 325.6 and 324.8 nm, which involved one-electron transitions from HOMO-11 to LUMO and HOMO-12 to LUMO, respectively. These MOs possessed a large contribution from the Au···Au core (Figures 3-8, 9). Moreover, the DFT calculations confirmed that the luminescence of this compound has a phosphorescent character due to an intersystem crossing from the lowest singlet excited (S_1) state to the lowest triplet excited (T) state; the calculated emission wavelength (511 nm) of the luminescence was highly similar to the experimental one. From these calculations, the emission was assigned to the transition in the Au···Au core. Notably, the internal luminescence quantum yields (Φ) for both salts were estimated to be more than 95% based on the absolute method using an integrating sphere. This value is considerably greater than that for the corresponding doubly bridged digold(I) complex, $[Au_2(dppm)_2Cl_2]$;[5a] the quantum yield of this complex was estimated to be 69% (λ_{em} = 480 nm) under the same conditions. Moreover, the quantum yields in the solid state of the other reported 2-coordinated gold(I) complexes, $[Au_2(dpephos)_2](BF_4)_2$ (dpephos = bis(2-diphenylphosphino)phenyl ether, λ_{em} = 558 nm, Φ = 19%),[45a] $[Au_3(dpmp)_2](PF_6)_3$ (dpmp = bis(diphenylphosphinomethyl)phenylphosphine, λ_{em} = 460 nm, Φ = 64%),[45b] and $[Au_4(rac\text{-dpmppm})_2](BF_4)_4$ (dpmppm = bis[(diphenylphosphinomethyl)phenylphosphino]methane, λ_{em} = 494 nm, Φ = 85%),[45c] are

also lower than that of [**5**]Cl_2 (Chart 3-1). The molecular rigidity of [**5**]$^{2+}$ owing to the triply bridged structure is assumed to lead to the improvement of the emission intensity compared with doubly bridged analogs. The emission band of [**5**]$Cl_2 \cdot 8.5H_2O$ and [**5**]$(OTf)_2 \cdot H_2O$ shifted slightly (by 10–15 nm) to longer wavelength when the temperature was lowered to 77 K, indicative of a stronger Au···Au interaction in the excitation state at lower temperature (Figure 3-11). In addition, the emission lifetime (ca. 5 μs) observed at 77 K was nearly the same as that (ca. 4 μs) observed at room temperature (Figure 3-7), and the quantum yields of [**5**]$Cl_2 \cdot 8.5H_2O$ and [**5**]$(OTf)_2 \cdot H_2O$ were still very high at 77 K. [**5**]$Cl_2 \cdot 8.5H_2O$ and [**5**]$(OTf)_2 \cdot H_2O$ dissolved in methanol showed a weak yellow emission (λ_{em} = 592 nm, Φ < 1%, Figure 3-12), presumably because of the equilibrium between the triply bridged structure in [**5**]$^{2+}$ and the doubly bridged structure in $[Au_2(dppm)_2]^{2+}$ ([**6**]$^{2+}$) in the solution.[57]

The crystallization and structural characterization of [**5**]$Cl_2 \cdot 8.5H_2O$ and [**5**]$(OTf)_2 \cdot H_2O$, in which two trigonal-planar Au^I centers are triply bridged by dppm ligands were succeeded. Solids [**5**]$Cl_2 \cdot 8.5H_2O$ and [**5**]$(OTf)_2 \cdot H_2O$ exhibited brilliant green and yellow-green emissions, which were attributed to phosphorescence. The difference in the emission wavelengths between [**5**]$Cl_2 \cdot 8.5H_2O$ and [**5**]$(OTf)_2 \cdot H_2O$ (ca. 30 nm) was likely due to the slight but appreciable difference in their Au···Au distances (3.03 Å for [**5**]$Cl_2 \cdot 8.5H_2O$ vs. 2.98 Å for [**5**]$(OTf)_2 \cdot H_2O$). Remarkably, the phosphorescence for both [**5**]$Cl_2 \cdot 8.5H_2O$ and [**5**]$(OTf)_2 \cdot H_2O$ was found to have an excellent quantum yield of more than 95%. This high quantum yield appears to be due to the molecular rigidity around two Au^I ions tightly bridged by three dppm ligands, together with the multiple intermolecular interactions in crystal, which completely prevented a nonradiative deactivation. The molecular rigidity was supported by the DFT calculations, which revealed a quite small structural difference between the ground singlet (S_0) and triplet excited (T) states in the optimized molecular structure in [**5**]Cl_2 (Figure 3-13). The emission color change dependent on the counter anions has also been observed in 2-coordinated gold(I) complexes, $[Au_2(xantphos)_2]X_2$ (X = Cl, OTf, PF_6, BF_4) [45d] and $[Au_4(rac\text{-dpmppm})_2]X_4$ (X = Cl, OTf, PF_6, BF_4) [45c] (Chart 3-2). Unlike the case of [**5**]X_2, which involve 3-coordinated Au^I centers, the emission quantum yield of $[Au_4(rac\text{-dpmppm})_2]X_4$, which involve 2-coordinated Au^I centers, was varied depending on the counter anions (Chart 3-2).[45c]

III-3-3. Two-step thermal transformation and emission color change of [5]$Cl_2 \cdot 8.5H_2O$.

The TG analysis of [**5**]$Cl_2 \cdot 8.5H_2O$ indicated that a gradual weight loss of 8.0%, which corresponds to the loss of 8.5 water molecules, occurred until 373 K to give a dehydrated form, followed by its decomposition at 573 K (Figure 3-1). Although no weight loss was observed between 373 and 473 K, the differential scanning calorimetry (DSC) showed an exothermal

peak at 399 K, indicative of the occurrence of an endothermal reaction at this temperature. In parallel with the dehydration reaction and subsequent endothermal reactions, dramatic changes in the original emission color were recognized; the emission color changed from green to yellow when a solid sample of [**5**]$Cl_2 \cdot 8.5H_2O$ was heated at 373 K, and further heating to 399 K caused the color change to blue (Figure 3-14). In the emission spectra, the sample heated at 373 K showed an emission band at 596 nm with a quantum yield of 52%, whereas the sample heated at 399 K showed an emission band at 470 nm with a quantum yield of 55%.

A solid-state ^{31}P NMR spectroscopy and powder X-ray diffraction (PXRD) study were carried out to characterize the two species formed by heating at 373 and 399 K. The ^{31}P NMR spectrum of an original solid sample of [**5**]$Cl_2 \cdot 8.5H_2O$ showed a signal centered at δ 18 ppm (Figure 3-15), which was assigned to P donors bound to Au^I centers. The same NMR spectral feature was observed for the sample heated at 373 K, indicative of the retention of the digold(I) structure in $[\mathbf{5}]^{2+}$ by dehydration. In contrast, the sample heated at 399 K exhibited a new signal at δ –44 ppm. Because the signal at δ –44 ppm corresponds well with that observed for a solid sample of dppm, the heating of [**5**]Cl_2 at 399 K causes the dissociation of a part of dppm ligands in $[\mathbf{5}]^{2+}$. In the PXRD, the diffraction pattern of a solid sample of [**5**]$Cl_2 \cdot 8.5H_2O$ was consistent with that simulated from its single-crystal X-ray data (Figure 3-16). In contrast, no notable diffractions were observed for a sample heated at 373 K. This is indicative of the collapse of the non-covalent intermolecular interactions due to the removal of water molecules of crystallization, thus converting them to an amorphous solid. Remarkably, the PXRD for a sample heated until 399 K exhibited sharp diffractions that were distinct from those for [**5**]$Cl_2 \cdot 8.5H_2O$. The structure of this new crystalline phase was successfully determined by the high-resolution powder X-ray diffraction using synchrotron radiation (λ = 1.30 Å) (Figure 3-17), which revealed the presence of a complex cation of $[Au_2(dppm)_2]^{2+}$ ($[\mathbf{6}]^{2+}$) and two chloride ions in the asymmetric unit. This complex cation contains two linear Au^I ions that are bridged by two dppm ligands, and each Au^I center has a diagonal P-Au^I-P geometry (av. Au–P = 2.34 Å and P–Au–P = 159°), with an Au···Au separation of 2.97 Å. In this structure, Cl^- ions are not involved in the coordination (Au···Cl > 3.6 Å) but act as a counter anion with the formation of CH···Cl interactions with neighboring complex cations. This structure is in sharp contrast to the previously reported structure in $[Au_2(dppm)_2Cl_2]$·acetone,[58] in which each Cl^- ion weakly coordinates to an Au^I center (av. Au–Cl = 2.77 Å) to form a *T*-shaped coordination geometry (Figure 3-18). Moreover, complex cations are connected to each other through multiple CH···π or π···π interactions, forming a closely packed lattice structure. Whereas non-coordinating dppm molecules are not accommodated in this crystal lattice, the elemental analytical data and the solid-state ^{31}P NMR spectrum implied that the dppm molecules were not sublimated to air

but were still contaminated as an amorphous solid in the sample heated at 399 K.

When a blue-emissive crystalline powder of [**6**]Cl_2 was manually ground in an agate mortar, a yellow-emissive amorphous powder of [**5**]Cl_2 was produced. Moreover, the continuous grinding of the powder of [**5**]Cl_2 after adding water produced a green-emissive crystalline powder of [**5**]$Cl_2 \cdot 8.5H_2O$. The assignment of these powders was made using their emission spectra and PXRD profiles (Figures 3-19, 20), thus indicating the reverse conversion from [**6**]Cl_2 to [**5**]Cl_2 and then to [**5**]$Cl_2 \cdot 8.5H_2O$.

Here, no significant change in the emission color was observed for [**5**]$(OTf)_2 \cdot H_2O$, even when its sample was heated to 473 K. Furthermore, the emission spectrum and PXRD pattern of a sample heated at 473 K were essentially identical to those of the original sample (Figures 3-21, 22), illustrating that its thermal stability is considerably higher than that of the OTf^- salt of $[\mathbf{5}]^{2+}$.

Remarkably, [**5**]$Cl_2 \cdot 8.5H_2O$ showed a two-step thermal transformation from its green-emissive crystalline phase to the blue-emissive crystalline phase ([**6**]Cl_2) via the yellow-emissive amorphous phase ([**5**]Cl_2), which was induced by the loss of water molecules of crystallization and the subsequent dissociation of a dppm ligand. The reverse conversion from [**6**]Cl_2 to [**5**]$Cl_2 \cdot 8.5H_2O$ by mechanical grinding in the presence of water via [**5**]Cl_2 was also recognized. To our knowledge, this is the first phosphorescent system with a high quantum yield of >95% that illustrates a reversible, crystalline-amorphous-crystalline thermal transformation accompanied by drastic emission color changes. Such a thermal transformation was not observed for [**5**]$(OTf)_2 \cdot H_2O$, which possesses a rigid crystalline framework, sustained by multiple cation-cation and cation-anion interactions without the mediation of water molecules. Thus, it is reasonable to consider that the water-molecule-mediated crystal structure in [**5**]$Cl_2 \cdot 8.5H_2O$, which was converted to the loosely packed amorphous structure in [**5**]Cl_2 via the removal of water molecules, together with the formation of the closely packed, non-hydrated crystal structure in [**6**]Cl_2 via the removal of a dppm ligand, is responsible for this unique thermal transformation. Finally, the present study demonstrated that trigonal-planar Au^I species are highly available for the future design and creation of functional luminescent materials.

III-4. Conclusion

In this chapter, the cage-type digold(I) complexes with three dppm ligands were prepared, and their emission behavior and pyrolysis were investigated.

The 1:2 reactions of $[Au_2(dppm)Cl_2]$ with dppm gave the digold(I) complex, $[Au_2(dppm)_3]Cl_2$ ([**5**]Cl_2), which was fully characterized by elemental analyses, ^{1}H NMR and IR spectroscopies, and single crystal X-ray diffraction analysis. Single crystal X-ray crystallography revealed that this molecule has the cage-like structure as proposed by previous spectroscopic report.[18] Note that [**5**]Cl_2 shows an extremely strong emission ($\Phi > 0.95$), which is higher than the ring-like analog, $[Au_2(dppm)_2]Cl_2$ ($\Phi = 0.69$). The molecular rigidity of $[\mathbf{5}]^{2+}$ is assumed to lead the improvement of the emission intensity.

The counter anions effect was also investigated in [**5**]X_2. Triflate salt of $[\mathbf{5}]^{2+}$ ([**5**]$(OTf)_2$) was successfully isolated from the reaction of [**5**]Cl_2 with NaOTf. The solid state emission color was varied depending on the counter anions (Cl = green, vs OTf = yellow green), owing to the difference in the Au···Au distance (Au···Au = 3.02 Å ([**5**]Cl_2) vs 2.98 Å ([**5**]$(OTf)_2$)).

Moreover, the thermal transformation of each complex was also investigated. Of particular note is the thermal crystalline-amorphous-crystalline transformation for the Cl salt, which is accompanied by drastic emission color changes. Single-crystal and powder X-ray diffractions demonstrated that the two-step transformation is induced by the loss of water molecules of crystallization with the subsequent removal of a dppm ligand to form $[\mathbf{5}]^{2+}$, which is mechanically reverted back to $[\mathbf{6}]^{2+}$. In addition, it was found that the thermal stability is varied dependent on the counter anions (Cl <OTf). It is assumed that the more hydrated crystal of [**5**]$Cl_2 \cdot 8.5H_2O$ is easy to collapse its crystal structure after the dehydration by heating.

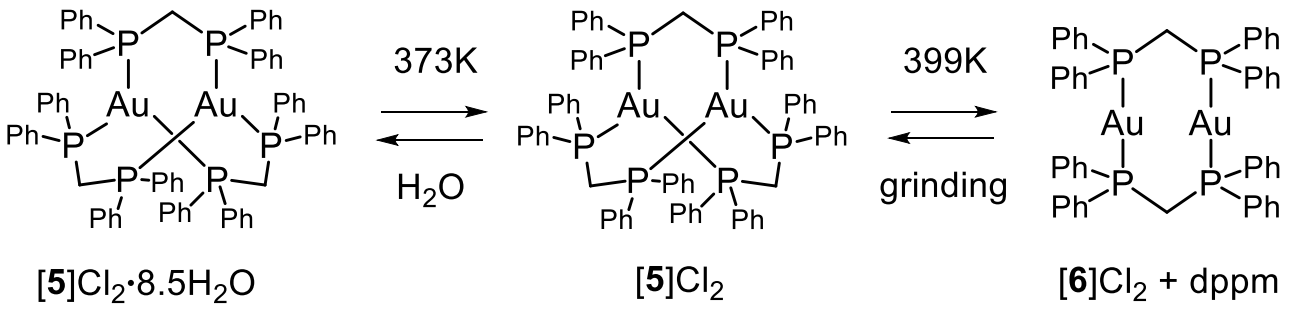

Scheme 3-1. Reversible two-step conversion of [**5**]$Cl_2 \cdot 8.5H_2O$.

Table 3-1. Emission (em) data in the solid state.

compounds	em: λ_{max}/ nm [a]	Φ [b]	τ / μs [c]
[**5**]$Cl_2 \cdot 8.5H_2O$ [d]	513	>0.95	4.51
[**5**]$Cl_2 \cdot 8.5H_2O$ [e]	523	>0.95	5.71
[**5**]Cl_2 [d]	590	0.52	*f*
[**6**]Cl_2 [d]	473	0.55	*f*
[**5**]$(OTf)_2 \cdot H_2O$ [d]	540	>0.95	4.15
[**5**]$(OTf)_2 \cdot H_2O$ [e]	555	>0.95	5.02
$[Au_2(dppm)_2Cl_2]$ [d,g]	480	0.69	*f*

a The excitation wavelength was set to 390 nm. *b* Error ± 5%. *c* Determined with excitation at 337 nm. *d* Measured at ambient temperature. *e* Measured at 77 K. *f* Not measured. *g* Heated sample of $[Au_2(dppm)_2Cl_2] \cdot$(acetone).

Table 3-2. Crystallographic data of [**5**]$Cl_2 \cdot 8.5H_2O$ and [**5**]$(OTf)_2 \cdot H_2O$.

	[5]$Cl_2 \cdot 8.5H_2O$	**[5]$(OTf)_2 \cdot H_2O$**
Formula	$C_{75}H_{66}Au_2Cl_2O_{8.5}P_6$	$C_{154}H_{132}Au_4F_{12}O_{14}P_{12}S_4$
Color, form	Pale yellow, block	Pale yellow, plate
Mw	1753.93	3722.33
Crystal system	Cubic	Monoclinic
Space group	*Pa*-3	$P2_1/n$
a/ Å	24.7728(9)	23.6242(4)
b/ Å	24.7728(9)	26.5462(5)
c/ Å	24.7728(9)	23.9188(4)
α (°)	90	90
β (°)	90	101.304(7)
γ (°)	90	90
V/ $Å^3$	15202.9(10)	14709.3(4)
Z	8	4
T/ K	200(2)	200(2)
F(000)	6928	7344
ρ calcd/ g· cm^{-3}	1.533	1.878
μ(Mo Kα)/ mm^{-1}	4.104	4.242
Crystal size /mm^3	0. 20×0.20×0.20	0.10×0.05×0.05
Limiting indices	$-29 \le h \le 32$,	$-30 \le h \le 30$,
	$-31 \le k \le 32$,	$-34 \le k \le 34$,
	$-29 \le l \le 32$	$-29 \le l \le 30$
R1 (I>2σ(I))[a)]	0.1282	0.0817
wR2 (all data) [b)]	0.2697	0.1666
GOF	1.332	1.071

a) $R1 = \Sigma||F_o|-|F_c|| / \Sigma|F_o|$.

b) $wR2 = [\Sigma(w(F_o^2-F_c^2)^2) / \Sigma w(F_o^2)^2]^{1/2}$.

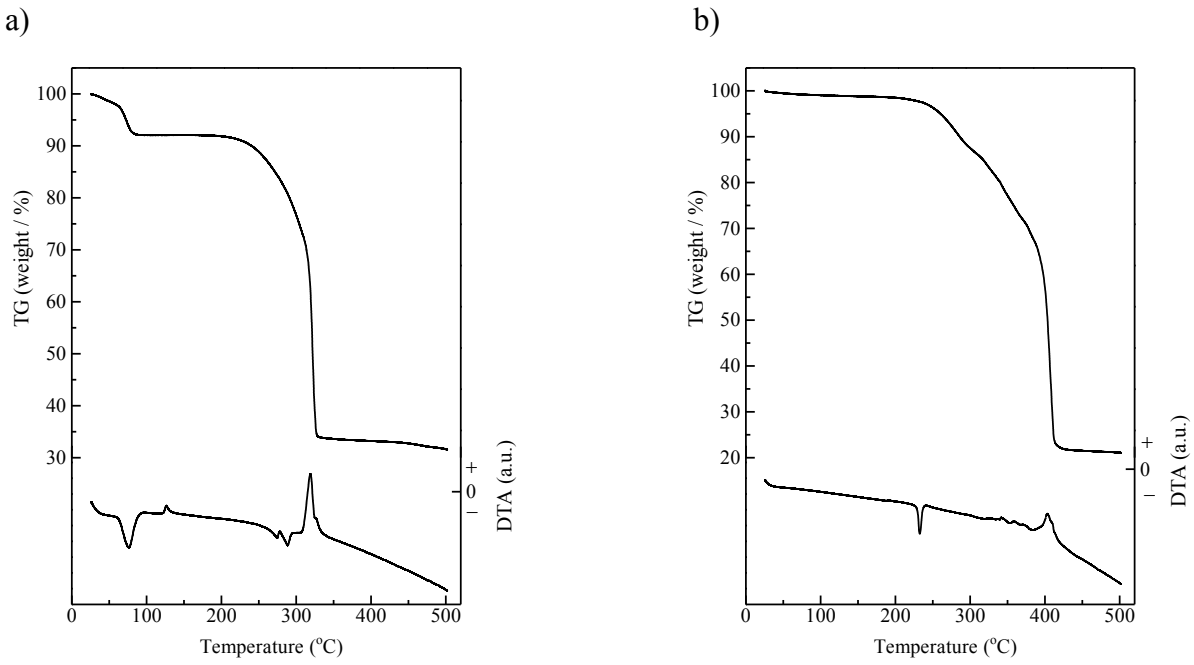

Figure 3-1. Thermogravimetric (TG) and differential thermal analysis (DTA) curves of (a) $[Au_2(dppm)_3]Cl_2 \cdot 8.5H_2O$ ([**5**]$Cl_2 \cdot 8.5H_2O$) and (b) $[Au_2(dppm)_3](OTf)_2 \cdot H_2O$ ([**5**]$(OTf)_2 \cdot H_2O$).

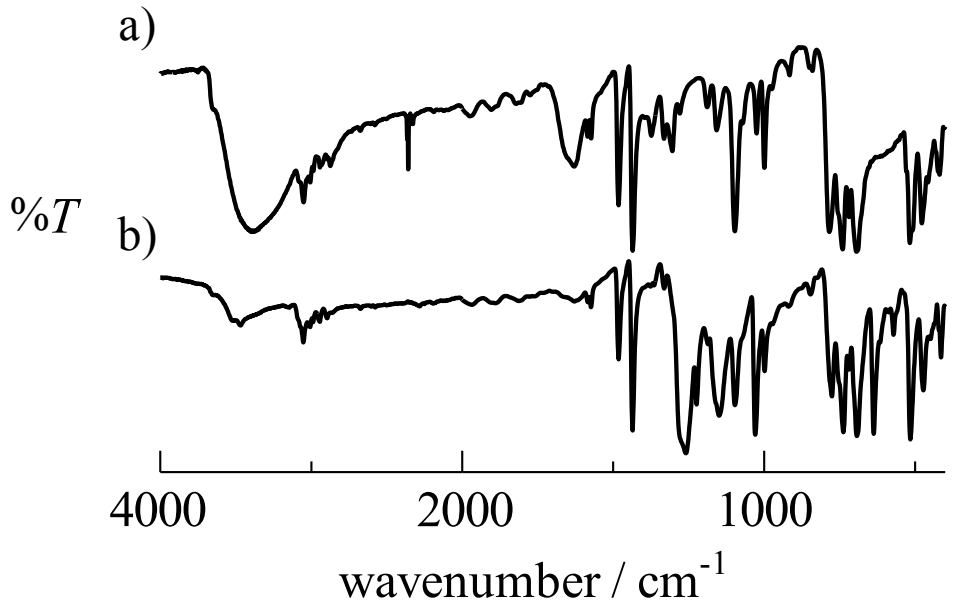

Figure 3-2. IR spectra of (a) [**5**]$Cl_2 \cdot 8.5H_2O$ and (b) [**5**]$(OTf)_2 \cdot H_2O$.

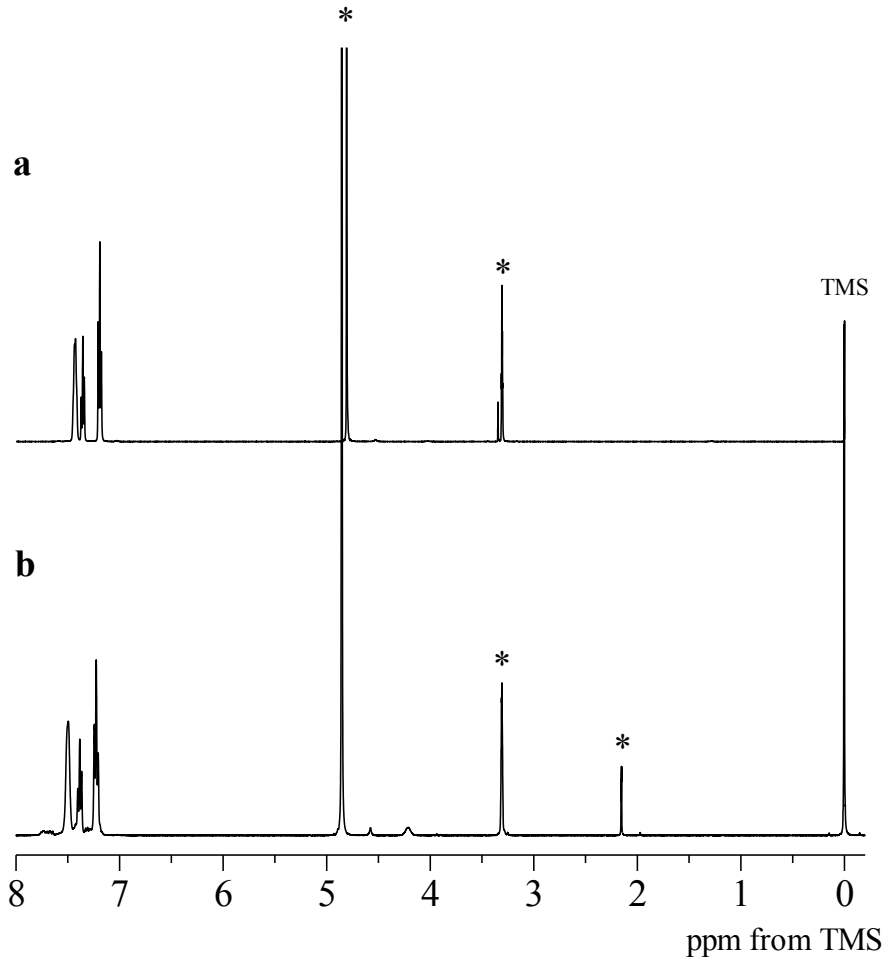

Figure 3-3. ^{1}H NMR spectrum of a) [**5**]$Cl_2 \cdot 8.5H_2O$ and b) [**5**]Cl_2 in CD_3OD. The symbol (*) indicates solvents.

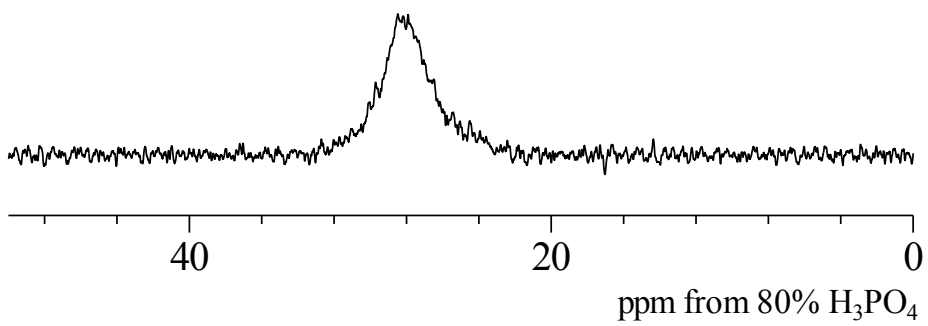

Figure 3-4. ^{31}P NMR spectrum of [**5**]$Cl_2 \cdot 8.5H_2O$ in CD_3OD.

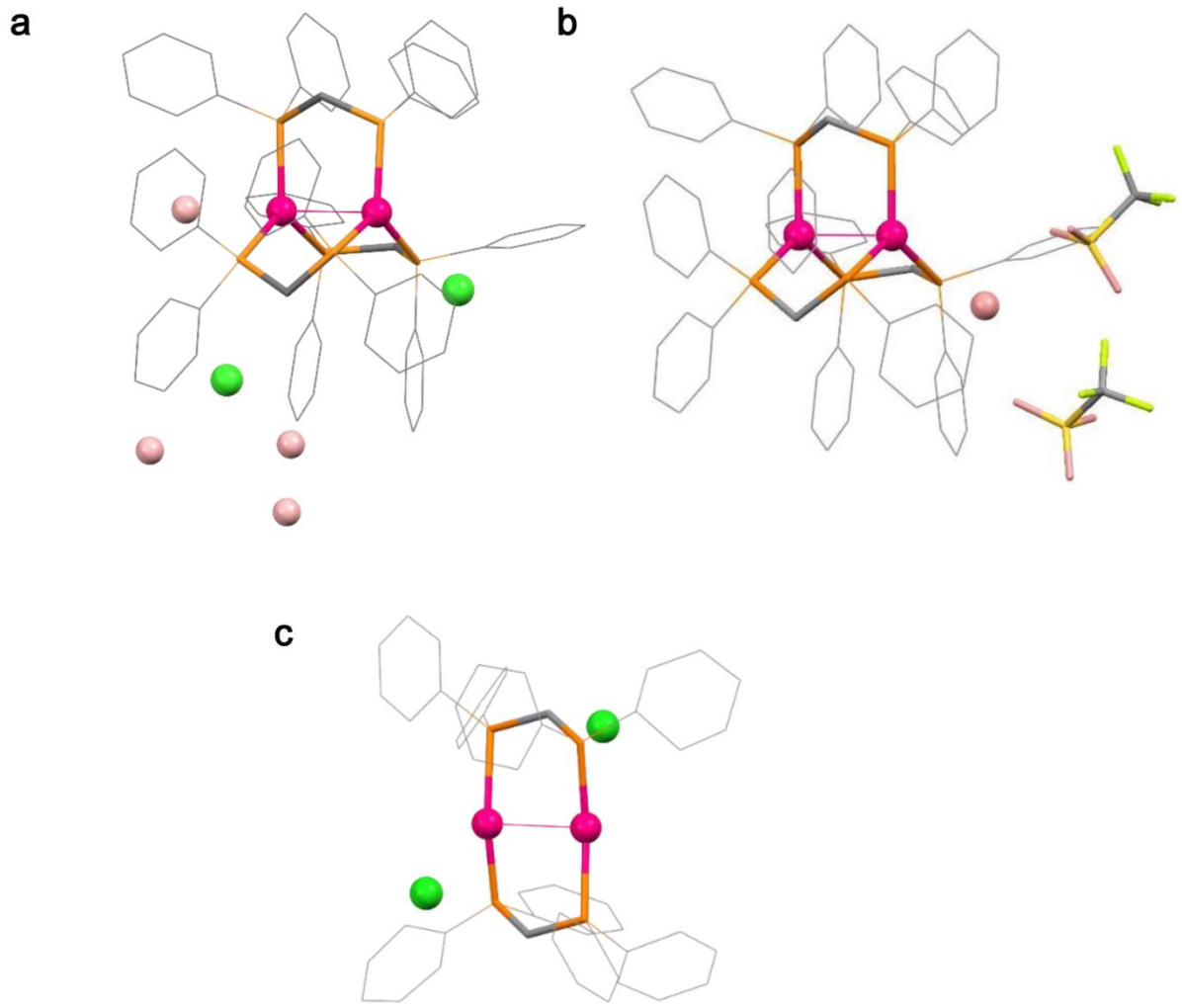

Figure 3-5. Crystal structures of [**5**]$^{2+}$ and [**6**]$^{2+}$. Perspective views of (a) [**5**]$Cl_2 \cdot 8.5H_2O$, (b) [**5**]$(OTf)_2 \cdot H_2O$, and (c) [**6**]Cl_2. Color Codes: Au, red; P, orange; S, yellow; Cl, green; C, gray; O, pink; F, light green.

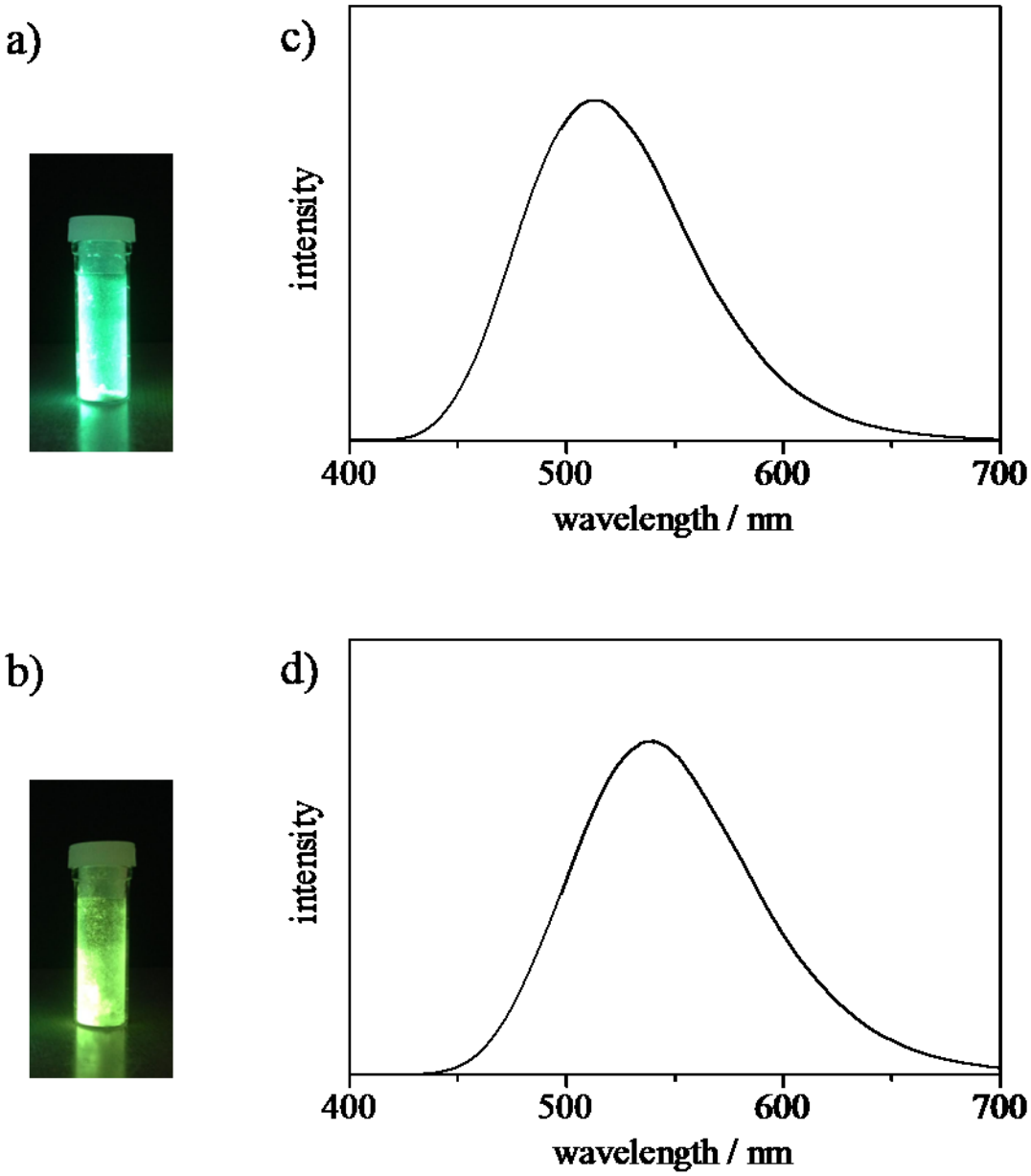

Figure 3-6. Photographs of (a) [**5**]$Cl_2 \cdot 8.5H_2O$ and (b) [**5**]$(OTf)_2 \cdot H_2O$ under UV light. Emission spectra of (c) [**5**]$Cl_2 \cdot 8.5H_2O$ (λ_{max} = 513 nm) and (d) [**5**]$(OTf)_2 \cdot H_2O$ (λ_{max} = 540 nm) in the solid state at room temperature. λ_{ex} = 390 nm for all measurements. λ_{em} = 510 nm for [**5**]$Cl_2 \cdot 8.5H_2O$. λ_{em} = 540 nm for [**5**]$(OTf)_2 \cdot H_2O$.

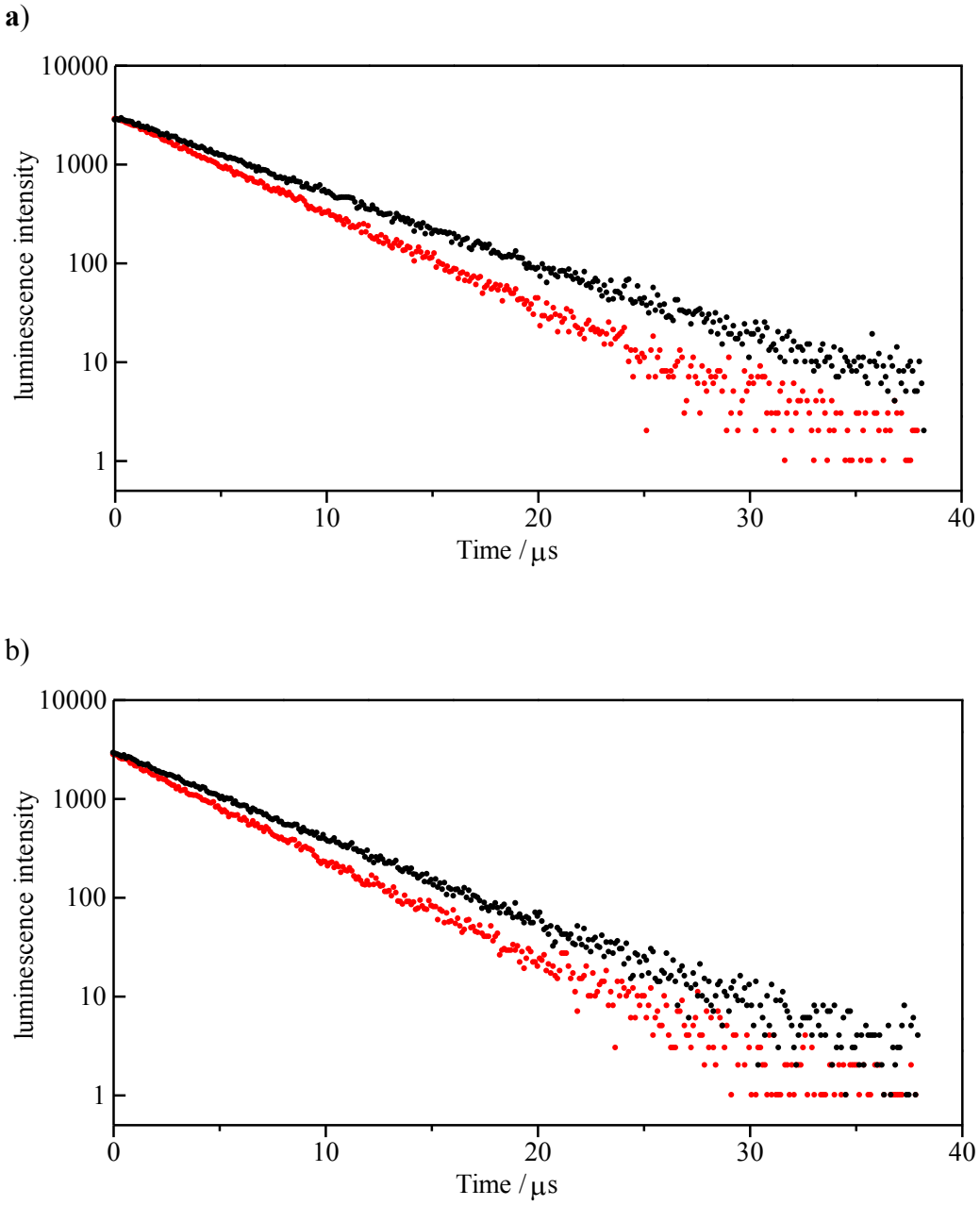

Figure 3-7. Emission decay of a) [**5**]$Cl_2 \cdot 8.5H_2O$ (λ_{ex} = 337 nm) and b) [**5**]$(OTf)_2 \cdot H_2O$ (λ_{ex} = 337 nm). Red and black dots indicate the data measured at room temperature and 77 K.

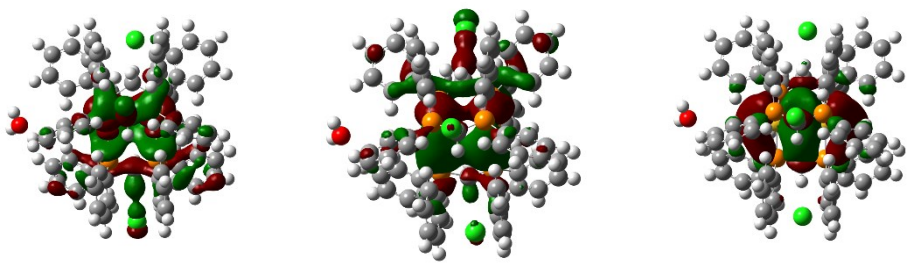

HOMO-12 HOMO-11 LUMO

Figure 3-8. Contour plots of [**5**]$Cl_2 \cdot H_2O$.

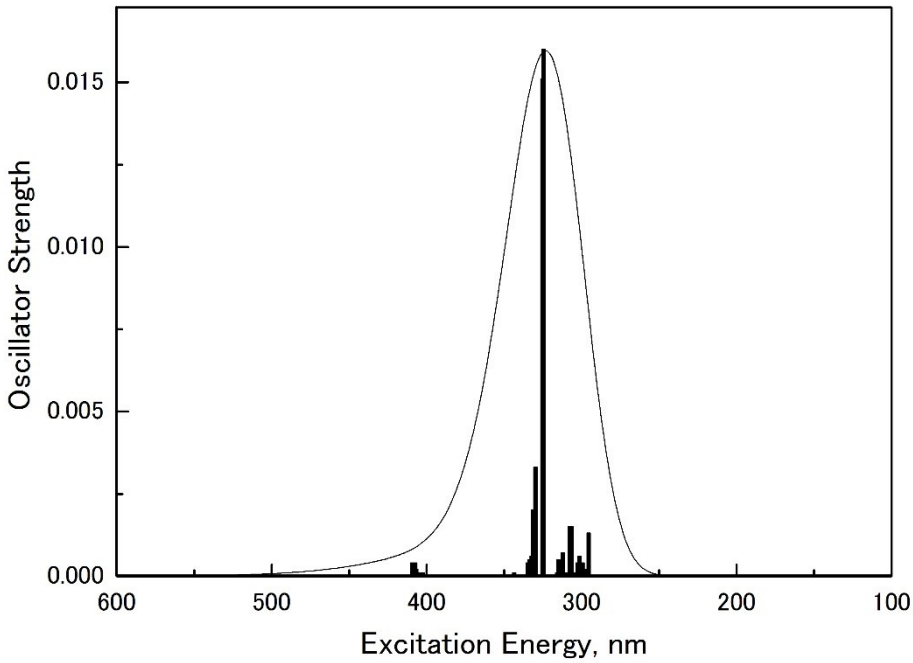

Figure 3-9. Simulated absorption spectrum of Au complex with $3Cl^-$ calculated by TD-DFT calculation. The two dominant components in the absorption spectrum were transitions from HOMO-12 to LUMO and from HOMO-11 to LUMO.

Table 3-3. Major components in the calculated absorption spectrum of Au complex.

System	Absorption energy, nm	Excitation nature [a]
$[Au_2(dppm)_3]Cl_2$	325.2	HOMO-11→LUMO (0.63822)
		HOMO-12→LUMO(-0.15071)
	324.4	HOMO-11→LUMO(0.14028)
		HOMO-12→LUMO(0.64768)

[a] Major coefficients in the CI expansion are in parenthesis.

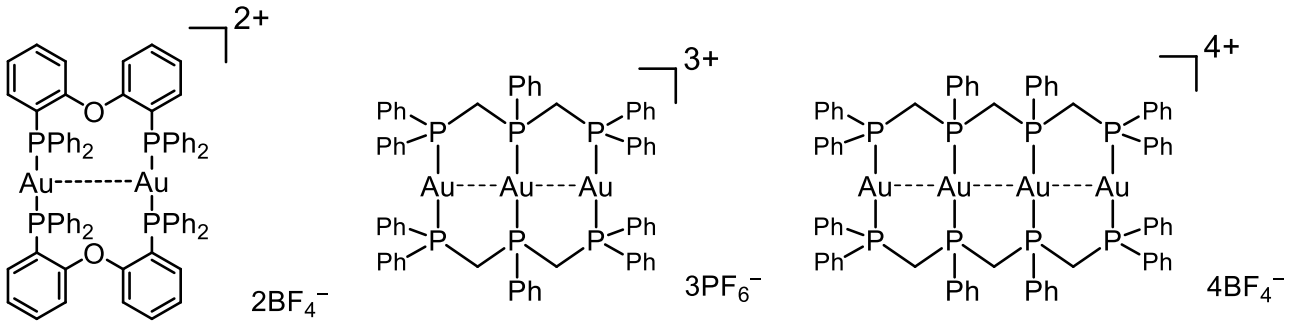

$[Au^I_2(dpephos)_2](BF_4)_2$ (λ_{em} = 558 nm, Φ = 19%)

$[Au^I_3(dpmp)_2](PF_6)_3$ (λ_{em} = 460 nm, Φ = 64%)

$[Au^I_4(dpmppm)_2](BF_4)_4$ (λ_{em} = 494 nm, Φ = 85%)

Chart 3-1. The molecular structures and emission quantum yields of two-coordinated gold(I) complexes.

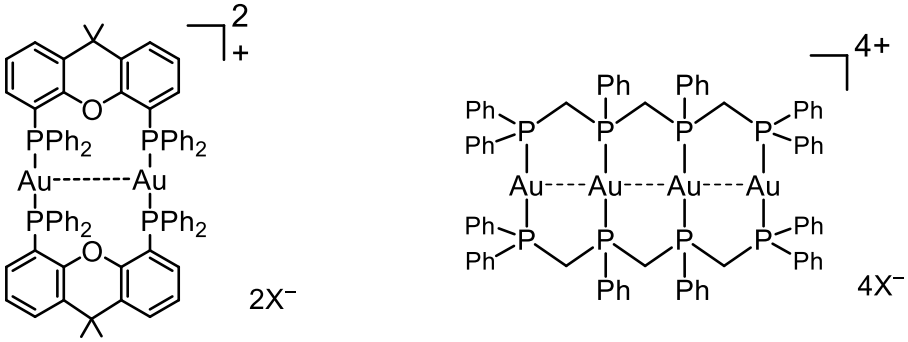

$[Au^I_2(xantphos)_2]X_2$
(X = BF_4, λ_{em} = 457 nm,
X = OTf, λ_{em} = 460 nm,
X = SCN, λ_{em} = 508 nm,
X = PF_6, λ_{em} = 675 nm)

$[Au^I_4(dpmppm)_2]X_4$
(X = Cl, λ_{em} = 505 nm, Φ = 8%,
X = OTf, λ_{em} = 485 nm, Φ = 67%,
X = PF_6, λ_{em} = 485 nm, Φ = 75%,
X = BF_4, λ_{em} = 494 nm, Φ = 85%)

Chart 3-2. The molecular structures and the emission properties of two-coordinated gold(I) complexes.

a)

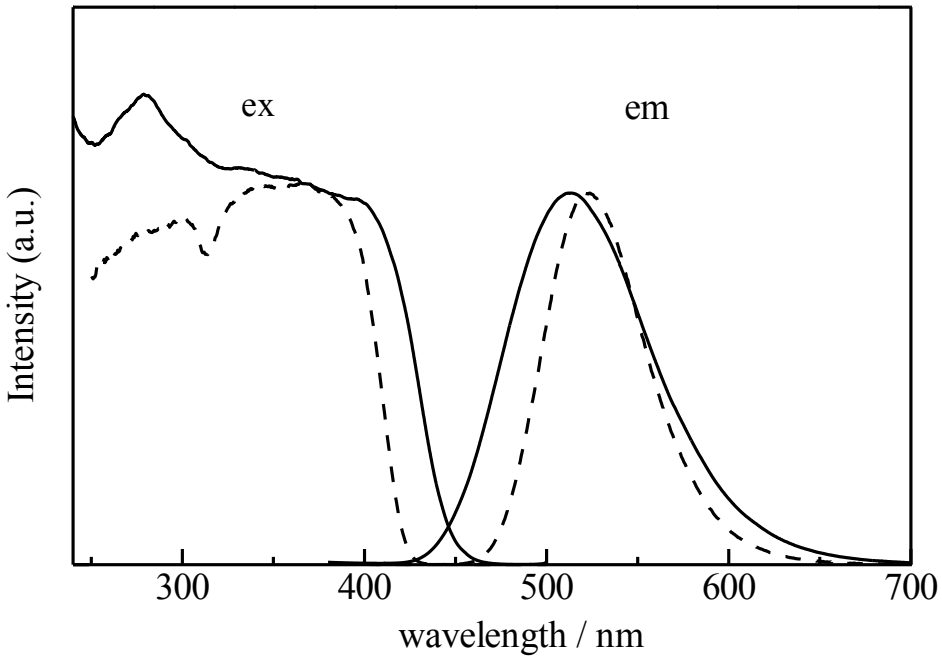

b)

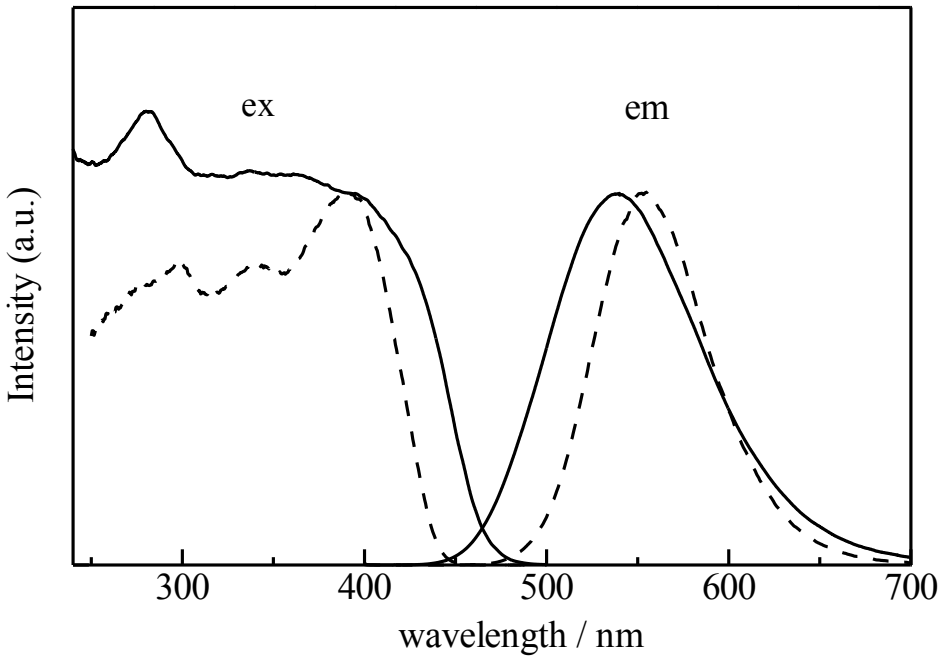

Figure 3-11. Emission (em) and excitation (ex) spectra of a) [**5**]$Cl_2 \cdot 8.5H_2O$ (em: λ_{max} = 523 nm) and b) [**5**]$(OTf)_2 \cdot H_2O$ (em: λ_{max} = 573 nm). Solid and dash lines indicate the data measured at room temperature and 77 K. λ_{ex} = 390 nm for all measurements. λ_{em} = 510 nm (room temperature) or 523 nm (77 K) for [**5**]$Cl_2 \cdot 8.5H_2O$. λ_{em} = 540 nm (room temperature) or 555 nm (77 K) for [**5**]$(OTf)_2 \cdot H_2O$.

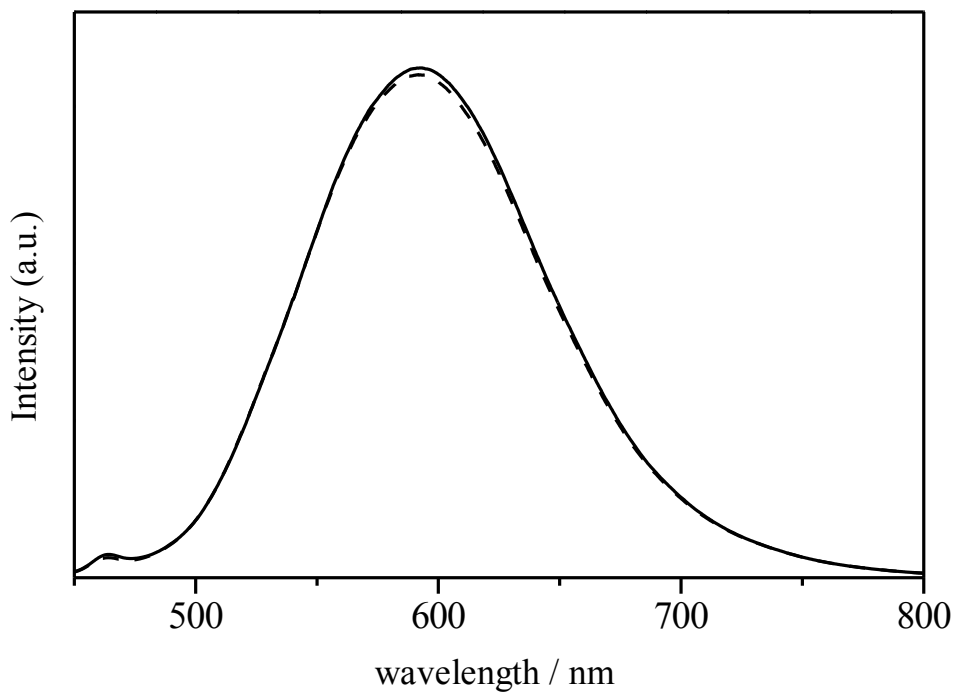

Figure 3-12. Emission spectra of [**5**]$Cl_2 \cdot 8.5H_2O$ (solid line, em: λ_{max} = 593 nm) and [**5**]$(OTf)_2 \cdot H_2O$ (dash line, em: λ_{max} = 592 nm) in MeOH at room temperature (λ_{ex} = 407 nm).

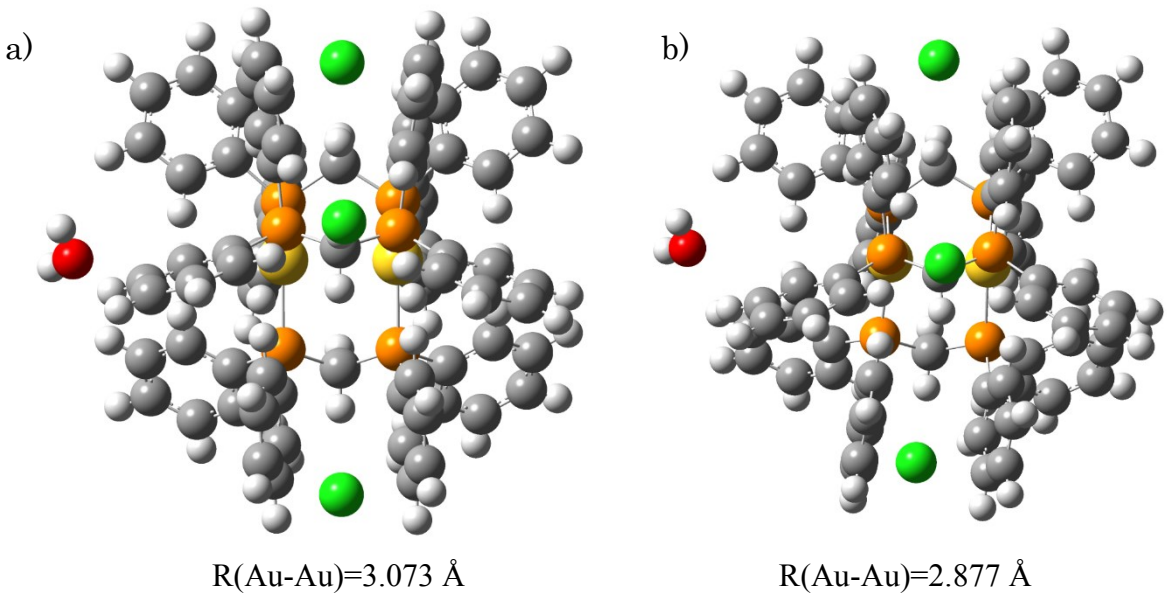

Figure 3-13. Optimized structures of a) singlet ground state and b) triplet excitation state of [**5**]$Cl_2 \cdot H_2O$.

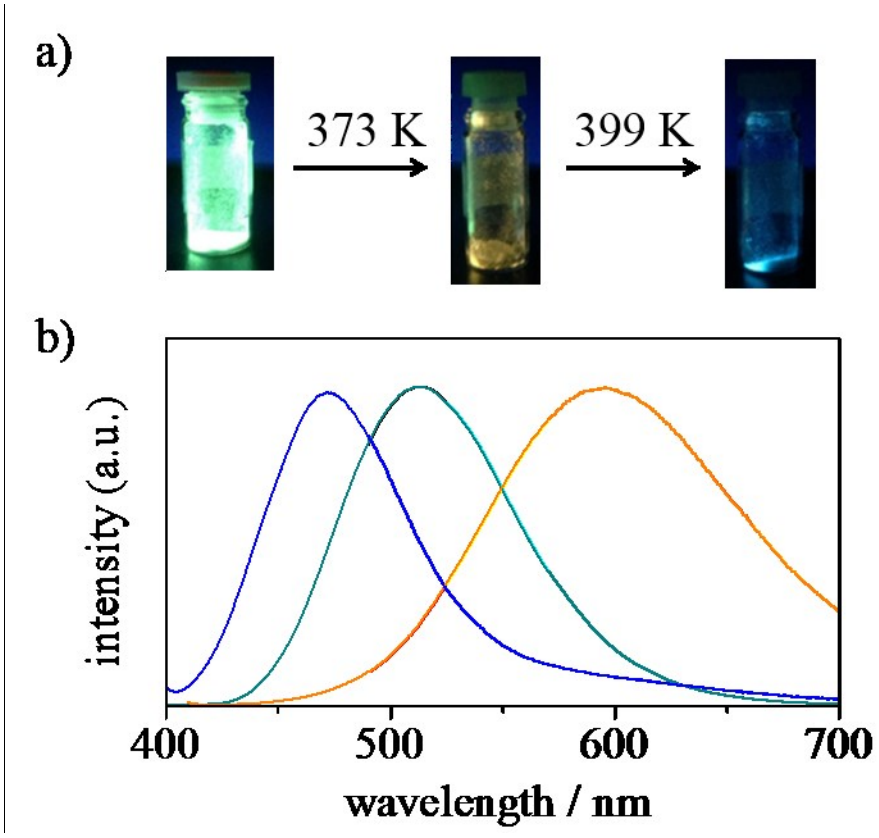

Figure 3-14. (a) Photographs under UV light and (b) emission spectra of fresh (green line, em: λ_{max} = 513 nm) and heated samples (treated at 373 K, yellow line, em: λ_{max} = 590 nm; at 399 K, blue line, em: λ_{max} = 473 nm) of [**5**]$Cl_2 \cdot 8.5H_2O$.

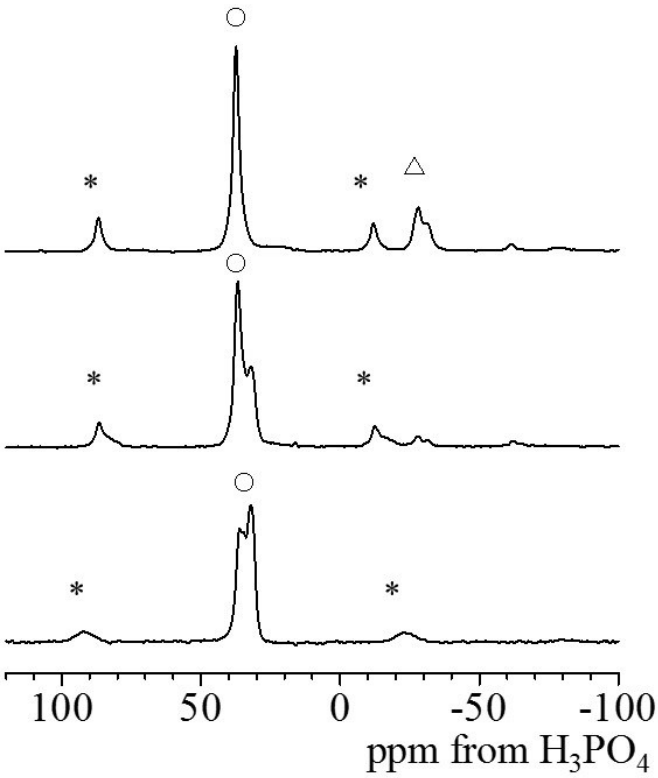

Figure 3-15. Solid-state MAS ^{31}P spectra of [**5**]$Cl_2 \cdot 8.5H_2O$, measured at room temperature. Bottom: fresh, middle: heated at 373 K, top: heated at 399 K. Symbols *, °, and Δ indicate side bands, bands due to coordinated dppm, and a band due to free dppm, respectively.

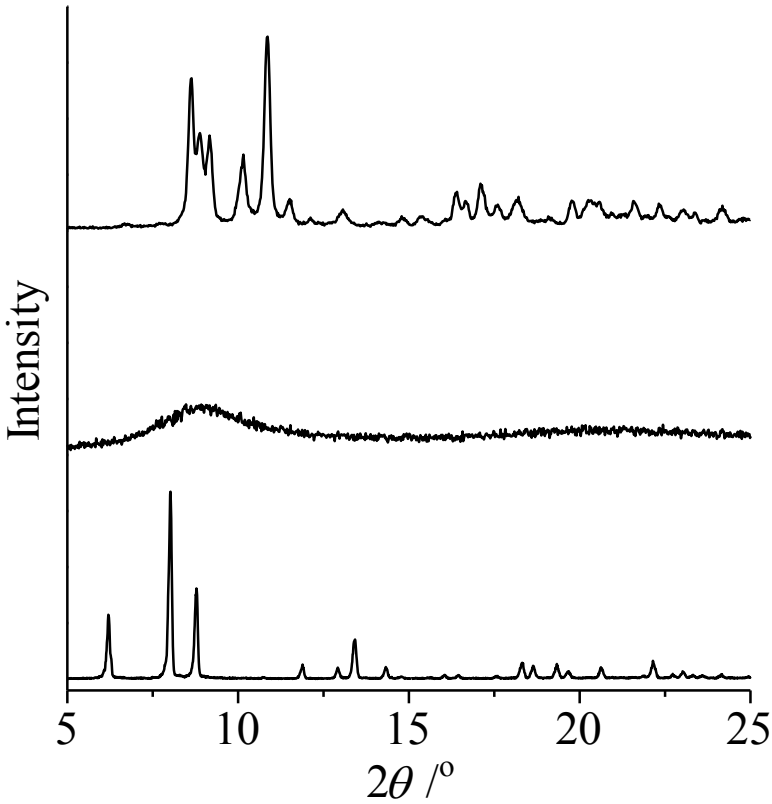

Figure 3-16. Powder X-ray diffraction of [**5**]$Cl_2 \cdot 8.5H_2O$ in the solid state. Bottom: fresh, middle: heated at 373 K, top: heated at 399 K.

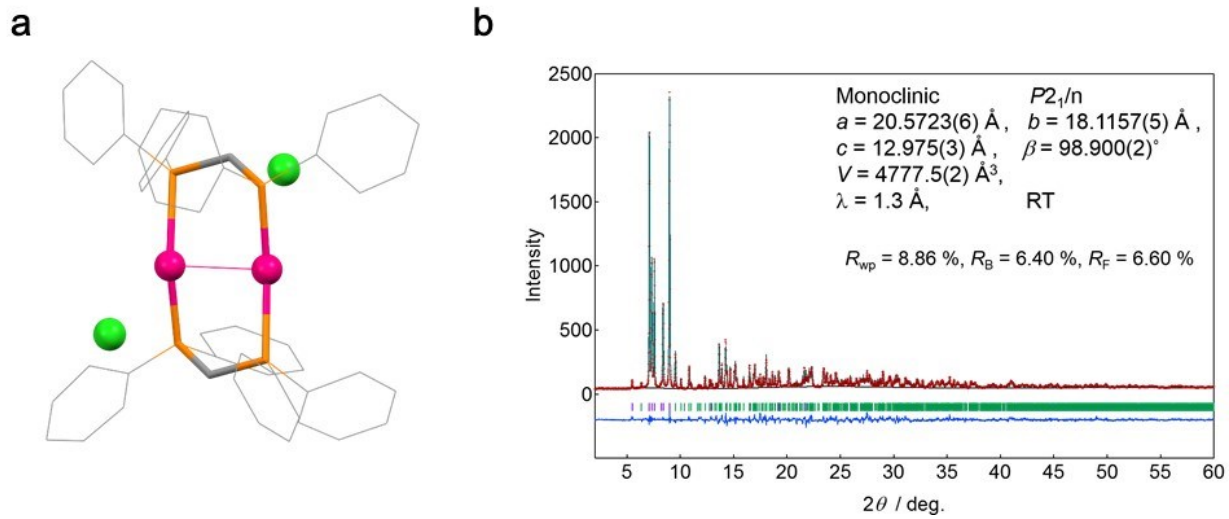

Figure 3-17. Perspective view of a) [**6**]Cl_2, which was determined by b) PXRD studies; experimental (red), calculated (black), and difference (blue) PXRD profiles and Bragg positions (green).

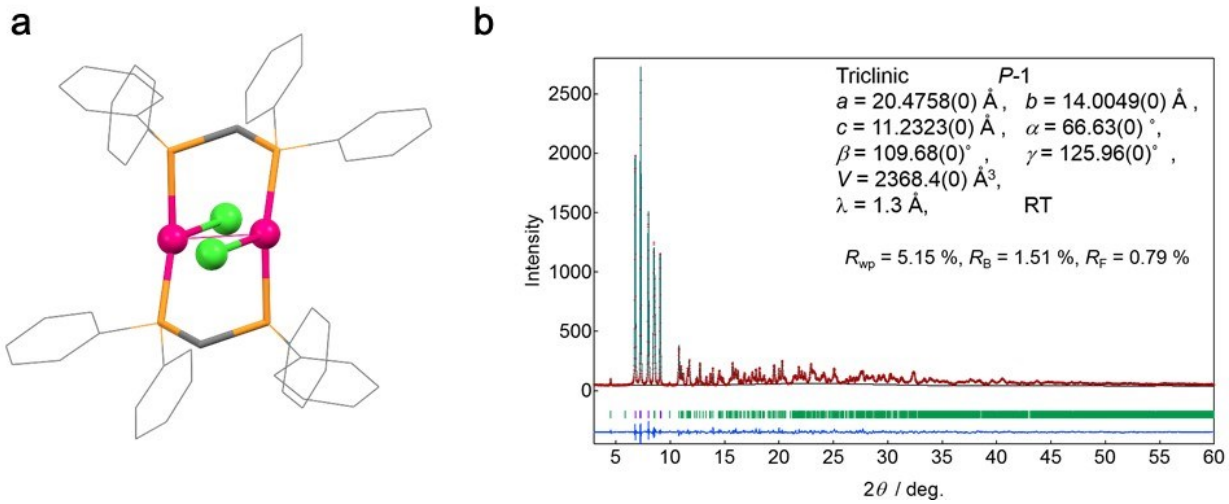

Figure 3-18. A perspective view of a) [$Au_2(dppm)_2Cl_2$], which was determined by b) PXRD studies; experimental (red), calculated (black), and difference (blue) PXRD profiles and Bragg positions (green). I determine the crystal structure of the heated sample of [$Au_2(dppm)_2Cl_2$]·(acetone). The Rietveld analysis of the powder X-ray diffraction pattern showed that the heated sample is [$Au_2(dppm)_2Cl_2$], where Au centers take a T-shaped structure bound by Cl^- (av. Au–Cl = 3.00 Å).

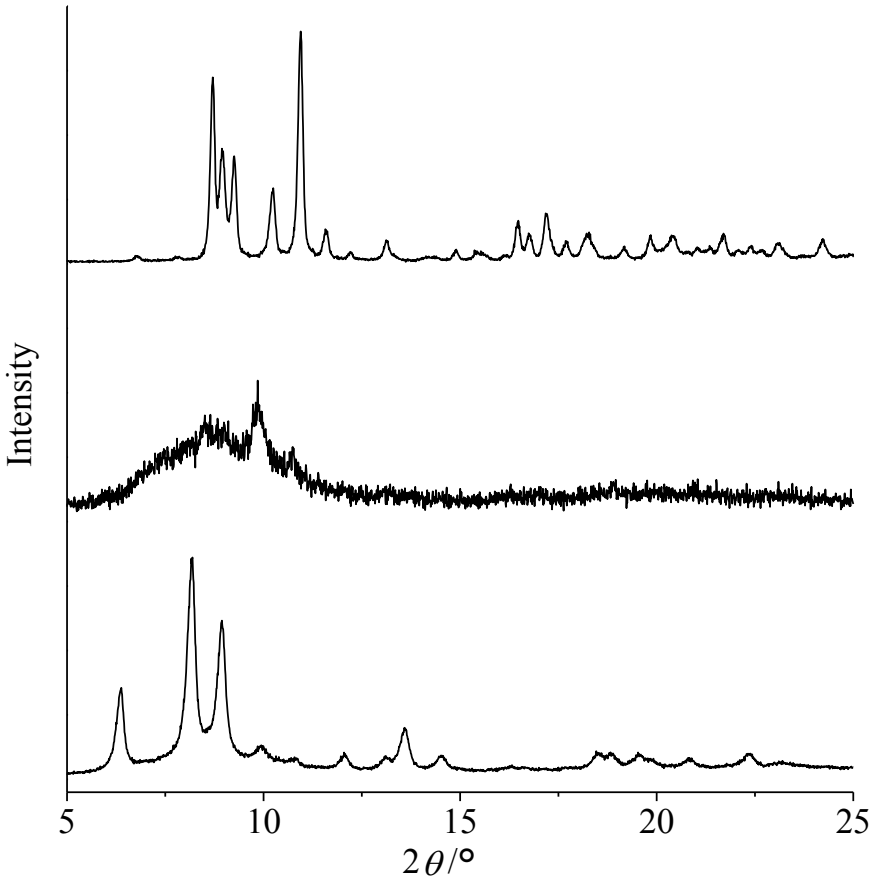

Figure 3-19. Powder X-ray diffraction in the solid state. Bottom: [**6**]Cl_2 after grinding in water, middle: ground sample of [**6**]Cl_2, top: [**6**]Cl_2.

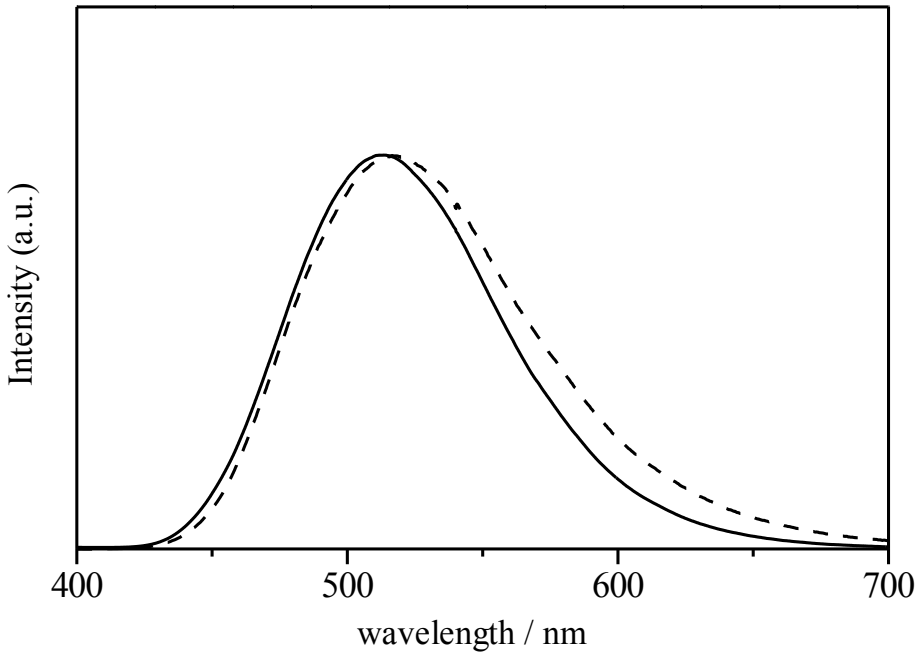

Figure 3-20. Emission spectra in the solid state. Solid line: [**5**]$Cl_2 \cdot 8.5H_2O$ (em: λ_{max} = 513 nm), and dash line: [**6**]Cl_2 (em: λ_{max} = 515 nm) after grinding in water. The emission quantum yield of the recovered sample is 85%. The lower quantum yield is likely due to the imperfect restoration of crystallinity resulting from this manual operation.

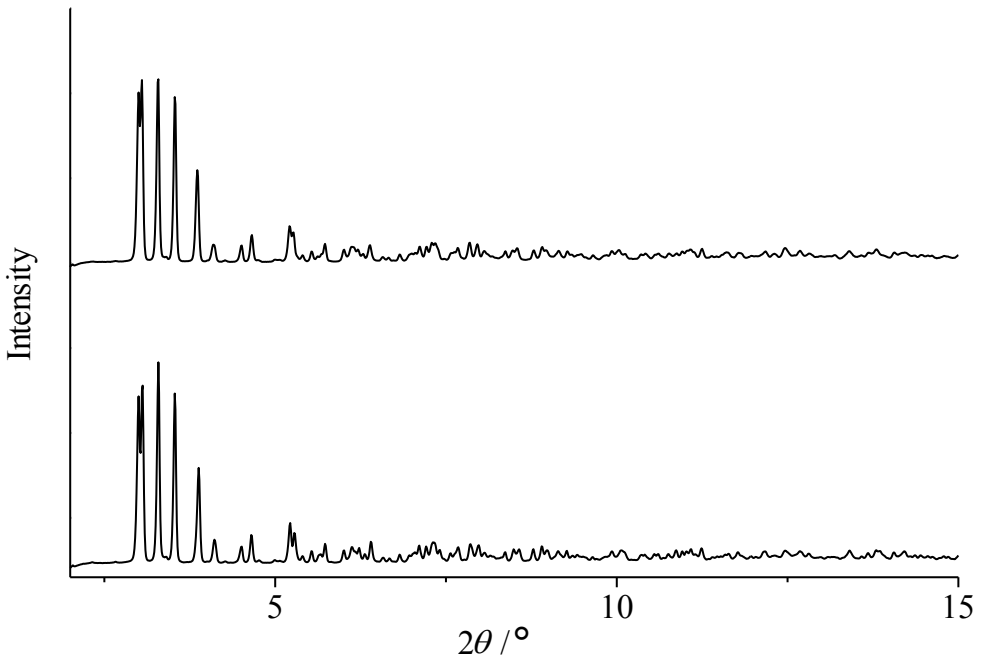

Figure 3-21. Powder X-ray diffraction of [**5**](OTf)$_2$·H$_2$O in the solid state. Bottom: fresh crystals, top: after being heated at 473 K.

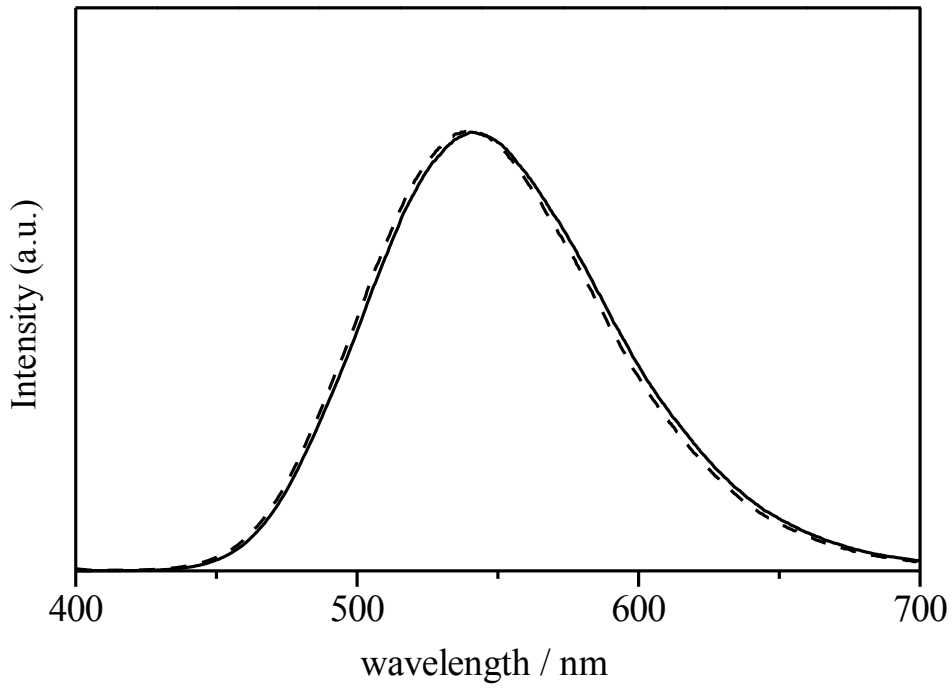

Figure 3-22. Emission spectra of [**5**](OTf)$_2$·H$_2$O in the solid state. Fresh sample (solid line, em: λ_{max} = 540 nm) and after being heated at 473 K (dash line, em: λ_{max} = 540 nm).

Chapter IV. Concluding Remarks.

This research aimed to find out new functionalities in a gold(I)-diphosphine coordination system. Among the four typical products of gold-diphosphine complexes, (i) $[Au_2(Ph_2P^\wedge PPh_2)]^{2+}$, (ii) $[Au_2(Ph_2P^\wedge PPh_2)_2]^{2+}$, (iii) $[Au_2(Ph_2P^\wedge PPh_2)_3]^{2+}$, and (iv) $[Au(Ph_2P^\wedge PPh_2)_2]^{+}$ ($Ph_2P^\wedge PPh_2$ = α,ω-bis(diphenylphosphino)alkanes; Chart 1-2), the linear-type $[Au_2(Ph_2P^\wedge PPh_2)]^{2+}$ and the cage-type $[Au_2(Ph_2P^\wedge PPh_2)_3]^{2+}$ complexes were selected and examined their ability as a crystallization-support unit and a strongly emissive material, respectively. By combining with the linear-type $[Au_2(dppe)]^{2+}$ complex, the crystallinity of the thiol-containing compound that is hardly crystallized by normal methods was drastically improved to form the heteroleptic S-bridged complexes. For the cage-type $[Au_2(dppm)_3]^{2+}$ complex, it was found that this class of compounds shows an extremely high photoluminescence at room temperature in the solid state due to the presence of a strong intramolecular aurophilic interaction and its molecular rigidity.

In Chapter II, the crystallinity improvement of highly hydrophilic metal complexes with thiomalic acid (H_3msa) by the introduction of the linear digold(I) unit, $[Au_2(dppe)]^{2+}$, was investigated. First, the new linear digold(I) complex, $[Au_2(dppe)(H_2msa\text{-}S)_2]$ ([H_4**1**]), in which two H_2msa^- ligands are spanned by a $\{Au_2(dppe)\}^{2+}$ moiety through S atoms, was synthesized by the 1:2 reaction of $[Au_2(dppe)Cl_2]$ with H_3msa in the presence of base. Complex [**1**]$^{4-}$ was successfully crystallized with the monogold(I) complex-cation, $[Au(dppe)_2]^{+}$, and were structurally characterized by single-crystal X-ray analysis. It was found that the coordination of [**1**]$^{4-}$ to Ni^{II} ions gives the three kinds of Au^{I}-Ni^{II} complexes ([**2**]$^{2-}$, [**3**]$^{4-}$, [**4**]), isolated as single-crystals, and their molecular structures were determined by single-crystal X-ray analysis. The three Au^{I}-Ni^{II} complexes with different nuclearity, trinuclear [**2**]$^{2-}$, hexanuclear [**3**]$^{4-}$, and heptanuclear [**4**], were obtained in a controlled manner by changing counter cations or solution pH. In basic conditions, the anionic trinulcear $Au^{I}_2Ni^{II}$ complex ([**2**]$^{2-}$) was crystallized by using small cations (Na^+, Mg^{2+}, Ni^{2+}, Co^{2+}) as a counter cation. On the other hand, the use of bigger Ca^{2+} ion gave only the hexanuclear [**3**]$^{4-}$ as single crystals. In acidic conditions, the heptanuclear $Au^{I}_4Ni^{II}_3$ [**4**] was crystallized through the partial protonation of the carboxylate groups of msa with the formation of μ_3-S structure. It is noteworthy that these heterometallic metal complexes are the first examples of the structurally characterized first-raw transition metal complexes with thiomalic acid. In addition, the tridentate-O_α,O_β,S coordination mode of msa^{3-} was found for the first time in [**2**]$^{2-}$ and [**3**]$^{4-}$. These results indicate that the linear digold(I) complex cations $[Au_2(Ph_2P^\wedge PPh_2)]^{2+}$ can act as a crystallization-supporting reagent available for highly

hydrophilic thiol-containing molecules.

In Chapter III, the digold(I) cage-type complex cation, $[Au_2(dppm)_3]^{2+}$ ($[\mathbf{5}]^{2+}$), was isolated as chloride ($[\mathbf{5}]Cl_2 \cdot 8.5H_2O$) and triflate salts ($[\mathbf{5}](OTf)_2 \cdot H_2O$). The cage-type structure in $[\mathbf{5}]^{2+}$ was confirmed by the single-crystal X-ray analysis for $[\mathbf{5}]Cl_2 \cdot 8.5H_2O$ and $[\mathbf{5}](OTf)_2 \cdot H_2O$. This is the first structural determination of the cage-type $[Au_2(Ph_2P\text{^}PPh_2)_3]^{2+}$ complex-cations. Emission spectral measurement and DFT calculation study demonstrated that crystal $[\mathbf{5}]Cl_2 \cdot 8.5H_2O$ shows a brilliant green emission originated from an Au···Au core under UV light irradiation and that its emission intensity is extremely strong ($\Phi > 0.95$). The emission intensity of $[\mathbf{5}]Cl_2 \cdot 8.5H_2O$ was higher than the ring-like analog, $[Au_2(dppm)_2]Cl_2$ ($\Phi = 0.69$). On the other hand, the triflate salt $[\mathbf{5}](OTf)_2 \cdot H_2O$ showed a brilliant yellow green emission ($\Phi > 0.95$). The difference in emission color was explained by the difference in an Au···Au distance (Au···Au = 3.02 Å ($[\mathbf{5}]Cl_2 \cdot 8.5H_2O$) vs 2.98 Å ($[\mathbf{5}](OTf)_2 \cdot H_2O$) in the crystalline state. The extremely high quantum yield of $[\mathbf{5}]X_2$ is reasonably explained by the rigid molecular structure due to the triple bridge of dppm. Of particular note is the thermal crystalline-amorphous-crystalline transformation for $[\mathbf{5}]Cl_2 \cdot 8.5H_2O$, which is accompanied by drastic two-step emission color changes. The powder X-ray diffractions demonstrated that the two-step transformation was induced by the loss of crystallinity owing to the removal of crystalline water molecules with the subsequent dissociation of partial dppm ligand to form $[\mathbf{5}]^{2+}$. Interestingly, $[\mathbf{5}]^{2+}$ was mechanically reverted back to $[Au_2(dppm)_2]^{2+}$ ($[\mathbf{6}]^{2+}$). The thermal stability of these crystals was decreased as increasing the number of solvated water molecules in crystal structure (Cl <OTf). The more hydrated crystal is easy to collapse its crystal structure because of the removal of solvated water molecules after heating, which weakens the intermolecular interactions in crystal. Therefore, the dppm ligand can be partially dissociated even in the solid state by heating. In summary, the strong emission ability and chromic behavior of $[Au_2(Ph_2P\text{^}PPh_2)_3]^{2+}$ type complex were demonstrated.

In the future, it is expected that the crystallization method of coordination compounds is progressed by using the linear-type $[Au_2(Ph_2P\text{^}PPh_2)]^{2+}$ gold(I)-diphosphine unit as found in the present study. In addition, new chromic materials and light-emitting devices by using gold-diphosphine complexes with cage-type $[Au_2(Ph_2P\text{^}PPh_2)_3]^{2+}$ structure will be developed. Finally, it should be noted that $[Au_2(dppe)]^{2+}$ and $[Au_2(dppm)_3]^{2+}$ have been known over 20 years ago, but the abovementioned functionalities have been unknown without any investigations. In a similar way, interesting but unexplored molecular structures and phenomena would be discovered in gold(I)-phosphine coordination systems.

References.

1. Hofmann, A. W. "Researches on the Phosphorus-Bases.-No. V. Diphosphonium-Compounds." Proceedings of the Royal Society of London 9, **1857**, 651-656.
2. R. F. Ziolo, S. Lipton, Z. Dori, *Chem. Soc.*, *Chem. Commun.*, **1970**, 1124.
3. (a) S. M. Kim, J. H. Park, Y. K. Chung, *Chem. Commun.*, **2011**, *47*, 6719. (b) E. Mizushima, T. Hayashi, M. Tanaka, *Org. Lett.*, **2003**, *5* (18), 3349. (c) T. J. Harrison, J. A. Kozak, M. Corbella-Pané, G. R. Dake, *J. Org. Chem.*, **2006**, *71* (12), 4525. (d) S. L. Crawley, R. L. Funk, *Org. Lett.*, **2006**, *8* (18), 3995.
4. (a) C. K. Mirabelli, R. K. Johnson, D. T. Hill, L. F. Faucette, G. R. Girard, G. Y. Kuo, C. M. Sung, S. T. Crooketm, *J. Med. Chem.* **1986**, *29*, 218. (b) S. S. Gunatilleke, A. M. Barrios, *J. Med. Chem.*, **2006**, *49*, 3933.
5. (a) C. King, J. Wang, Md. N. I. Khan, J. P. Fackler, Jr. *Inorg. Chem.*, **1989**, *28*, 2145. (b) C. King, M. N. I. Khan, R. J. Staples, J. P. Fackler Jr., *Inorg. Chem.* **1992**, *31*, 3236.
6. M. C. Gimeno, *The Chemistry of Gold*, Wiley-VCH, **2008**, 10-30.
7. (a) A. O. Borissova, A. A. Korlyukov, M. Y. Antipin, K. A. Lyssenko, *J. Phys. Chem. A*, **2008**, *112*, (46), 11519. (b) R. J. Staples, C. King, M. N. I. Khan, R. E. P. Winpenny, J. P. Fackler Jr., *Acta Cryst.* **1993**, *C49*, 472. (c) F. Olbrich, R. J. Lagow, *Z. anorg. allg*, *Chem.*, **1995**, *621*, 1929. (d) P. G. Jones, *J. Chem. Soc. Chem. Commun.*, **1980**, 1031.
8. (a) J. M. Forward, D. Bohmann, J. P. Fackler Jr., R. J. Staples., *Inorg. Chem.* **1995**, *34*, 6330. (b) M. Wenzel, B. Bertrand, M. Eymin, V. Comte, J. A. Harvey, P. Richard, M. Groessl, O. Zava, H. Amrouche, P. D. Harvey, P. L. Gendre, M. Picquet, A. Casini, *Inorg. Chem.*, **1992**, *31*, 3236.
9. (a) C. I. Yeo, K. K. Ooi, A. M. Akim, K. P. Ang, Z. A. Fairuz, S. N. B. A. Halim, S. W. Ng, H. Seng, E. R.T. Tiekink, *J. Inorg. Biochem.*, **2013**, *127*, 24. (b) L. Ortego, J. Gonzalo-Asensio, A. Laguna, M. D. Villacampa, M. C. Gimeno, *J. Inorg. Biochem.*, **2015**, *146*, 19.
10. A. McAuliffe, R. V. Parish, P. D. Randall, *J. Chem. Soc.*, *Dalton Trans.*, **1979**, 1730.
11. V. Cámara, N. Masciocchi, J. Gil-Rubio, J. Vicente, *Chem. Eur. J.*, **2014**, *20*, 1389.
12. (a) Y. Hashimoto, K. Tsuge, T. Konno, *Chem. Lett.*, **2010**, *39*, 601. (b) Y. Hashimoto, N. Yoshinari, D. Naruse, K. Nozaki, T. Konno, *Inorg. Chem.*, **2013**, *52*, 14368.
13. A. Igashira-Kamiyama, N. Matsushita, R. Lee, K. Tsuge, T. Konno, *Bull. Chem. Soc. Jpn.*, **2012**, *85*, 706.

14. (a) R. Lee, A. Igashira-Kamiyama, H. Motoyoshi, T. Konno *CrystEngComm*, **2012**, *14*, 1936. (b) R. Lee, A. Igashira-Kamiyama, M. Okumura, T. Konno, *Bull. Chem. Soc. Jpn.*, **2013**, *86*, 908.
15. N. Yoshinari, A. Kakuya, R. Lee, T. Konno, *Bull. Chem. Soc. Jpn.*, **2015**, *88*, 59.
16. (a) P. Pyykkö, *Chem. Rev.* **1997**, *97*, 597. (b) H. Schmidbaur, A. Schier, *Chem. Soc. Rev.*, **2008**, *37*, 1931. (c) C. M. Che, S. W. Lai, *Coord. Chem. Rev.* **2005**, *249*, 1296. (d) M. J. Katz, K. Sakai, D. B. Leznoff, *Chem. Soc. Rev.* **2008**, 37, 1884.
17. (a) S. H. Lim, M. M. Olmstead, A. L. Balch , *J. Am. Chem. Soc.* **2011**, *133*, 10229. (b) C. Jobbágy, P. Baranyai, G. Marsi, B. Rácz, L. Li, P. Naumov, A. Deák (c) S. Pal, N. Kathewad, R. Pant, S. Khan, *Inorg. Chem.* **2015**, *54*, 10172. (d) V. W. Yam, S. W. Choi, K. Cheung, *Chem. Commun.*, **1996**, 1173.
18. S. Al-Baker, W. E. Hill, *J. Chem. Soc. Dalton trans.*, **1985**, 2655.
19. C. D. Delfs, H. J. Kitto, R. Stranger, G. F. Swiegers, S. B. Wild, A. C. Willis, G. J. Wilson, *Inorg. Chem.*, **2003**, *42*, 4469.
20. S. J. Berners-Price, C. K. Mirabelli, R. K. Johnson, M. R. Mattern, F. L. McCabe, L. F. Faucette, C. Sung, S. Mong, P. J. Sadler, S. T. Crooke, *CANCER RESEARCH,* **1986**, *46*, 5486.
21. H. Edward F, C. Joyce, G. Catherine, *Journal of Laboratory and Clinical Medicine*, **1941**, *26*, 1750.
22. W. F. Pickering, A. McAuley, *Journal of the Chemical Society A*: *Inorganic, Physical, Theoretical,* **1968**, 1173.
23. L. F. Larkworthy, D. Sattari, *J. inorg. nucl. Chem*, **1980**, *42*, 551.
24. A. G. Lappin, A. McAuley, *Journal of the Chemical Society, Dalton Transactions*, **1978**, 1606.
25. G. Crisponi, A. Diaz, V. M. Nurchi, T. Pivetta, M. J. T. Estevez, **2002**, 1319.
26. J. S. Fritz, T. A. Palemer, *Analytical Chemistry*, **1961**, *33*, 98.
27. (a) R. S. Saxena, K. C. Gupta, M. L. Mittal, *J. inorg, nucl. Chem.*, **1968**, *30*, 189. (b) K. Nimiya, K. Onoue, Y. Kondoh, N. C. Kasuga, *Polyhedron*, **1995**, *14*, 1359.
28. K. Hegetschweiler, T. Keller, H. Zimmermann, W. Schneider, *Inorganica Chimica Acta*, **1990**, *169*, 235.
29. D. J. LeBlanc, R. W. Smith, Z. Wang, H. E. Howard-Lock, C. J. L. Lock, *J. Chem. Soc., Dalton Trans.*, **1997**, 3263.
30. R. Bau, *J. Am. Chem. Soc.* **1998**, *120*, 9380.
31. R. G. Buckley, A. M. Elsome, S. P. Fricker, *Inorg. Chem.* **1996**, *35*, 1659.
32. D. Hüse, L. Bíró, J. Patalenszki, A. C. Bényei, P. Buglyó, *Eur. J. Inorg. Chem.* **2014**,

5204.

33. (a) T. Konno, T. Yoshimura, K. Aoki, K. Okamoto, M. Hirotsu, *Angew. Chem. Int. Ed.*, **2001**, *40*, 1765. (b) T. Konno, Y. Shimazaki, T. Yamaguchi, T. Ito, M. Hirotsu, *Angew. Chem. Int. Ed.*, **2002**, *41*, 4711. (c) M. Taguchi, A. Igashira-Kamiyama, T. Kajiwara, T. Konno, *Angew. Chem. Int. Ed.*, **2007**, *46*, 2422. (d) T. Aridomi, K. Takamura, A. Igashira-Kamiyama, T. Konno, *Chem. Eur. J.*, **2008**, *14*, 7752. (e) Y. Sameshima, N. Yoshinari, K. Tsuge, A. Igashira-Kamiyama, T. Konno, *Angew. Chem. Int. Ed.*, **2009**, *48*, 8469. (f) A. Igashira-Kamiyama, T. Konno, *Dalton Trans.*, **2011**, *40*, 7249.
34. C. K. Mirabelli, D. T.Hill, L. F. Faucette, F. L. McCabe, G. R. Girard, D. B. Bryan, B. M. Sutton, J. O'L. Bartus, S. T. Crooke, and R. K. Johnson, *J. Med. Chem.* **1987**, *30*, 2181.
35. G. M. Sheldrick, *Acta Cryst*., **2008**, *A64*, 112.
36. A. L. Spek, *Acta Cryst*. **2009**, *D65*, 148.
37. K. Nakamoto, *Infrared and Raman Spectra of Inorganic and Coordination Compounds*, 5th ed., Wiley, Chichester, 1997.
38. J. R. Gispert, Coordination Chemistry, Wiley-VCH Verlag GmbH & Co. KGaA, Weinheim, Germany, **2008**.
39. (a) M. H. Keefe, K. D. Benkstein, J. T. Hupp, *Coordination Chemistry Reviews*, **2000**, *205*, 201. (b) X. Zhang, Z. Chi, Y. Zhang, S. Liu, J. Xu, *J. Mater. Chem. C*, **2013**, *1*, 3376. (c) O. S. Wenger, *Chem. Rev.*, **2013**, *113*, 3686.
40. M. J. Katz, T. Ramnial, H. Yu, D. B. Leznoff, *J. Am. Chem. Soc*. **2008**, *130*, 10662.
41. C. Jobbágy, M. Molnár, P. Baranyai, A. Hamza, G. Pálinkása, A. Deák, *CrystEngComm* **2014**, *16*, 3192.
42. M. Saitoh, A. L. Balch, J. Yuasa, T. Kawai, *Inorg. Chem.* **2010**, *49*, 7129.
43. Liang, J.; Chen, Z.; Yin, J.; Yu, G.; Liu, S. H. *Chem. Commun*. **2013**, *49*, 3567-3569.
44. H. Ito, M. Muromoto, S. Kurenuma, S. Ishizaka, N. Kitamura, H. Sato, T. Seki, *Nat. Commun*. **2013**, *4*, 2009.
45. (a) C. Jobbágy, P. Baranyai, G. Marsi, B. Rácz, L. Li, P. Naumov, A. Deák, *J. Mater. Chem. C*, **2016**, *4*, 10253. (b) M. T. Dau, J. R. Shakirova, A. J. Karttunen, E. V. Grachova, S. P. Tunik, A. S. Melnikov, T. A. Pakkanen, I. O. Koshevoy, *Inorg. Chem*. **2014**, *53*, 4705. (c) T. Tanase, R. Otaki, T. Nishida, H. Takenaka, Y. Takemura, B. Kure, T. Nakajima, Y. Kitagawa, T. Tsubomura, *Chem. Eur. J.* **2014**, *20*, 1577. (d) C. Jobbágy, M. Molnár, P. Baranyai, A. Deák, *Dalton Trans*., **2014**, *43*, 11807.

46. (a) D. Li, C. Che, H. Kwong, V. W. Yam, *J. Chem. Soc., Dalton trans*. **1992**, 3325. (b) S. Shieh, D. Li, S. Peng, C. *J.* Che, *Chem. Soc., Dalton trans*. **1993**, 195. (c) V. W. Yam, W. *J.* Lee, *Chem. Soc., Dalton trans*. **1993**, 2097.
47. Z. Wei, Z. Gu, R. K. Arvapally, Y. Chen, R. N. McDougald Jr., J. F. Ivy, A. A. Yakovenko, D. Feng, M. A. Omary, H. Zhou, *J. Am. Chem. Soc*. **2014**, *136*, 8269.
48. J. B. Birks, *J. Res. Natl. Bur. Stand. A,* **1976**, *80*, 389.
49. G. M. Sheldrick, *Acta Cryst A*, **2008**, *64*, 112.
50. A. Boultif, D. Louër, *J. Appl. Crystallogr*. **1991**, *24*, 987.
51. W I. F. David, K. Shankland, J. Streek, E. Pidcock, W. D. S. Motherwellb, J. C. Cole, *J. Appl. Crystallogr*., **2006**, *39*, 910.
52. H. M. A. Rietveld, *J. Appl. Crystallogr*. **1969**, *2*, 65.
53. F. Izumi, K. Momma, *Solid State Phenom*. **2007**, *130*, 15.
54. K. Momma, F. *J.* Izumi, *Appl. Crystallogr*. **2008**, *41*, 653.
55. Frisch, M. J. *et al.* Gaussian 09, Revision C.01, **2009**, Gaussian, Inc., Wallingford CT.
56. M. Hong, D. Wu, H. Liu, T. C. W. Mak, Z. Zhou, D. Wu, S. Li, *Polyhedron*, **1997**, *16*, 1957-1962.
57. M. Gimeno, A. Laguna, *Chem. Rev.*, **1997**, *97*, *3*, 511.
58. H. Schmidbaur, A. Wohlleben, U. Schubert, A. Frank, G. Huttner, *Chem. Ber*., **1977**, *110*, 2751.

Acknowledgement.

I express my deepest gratitude to Professor Takumi Konno for his expert guidance and constant warm encouragement during the course of my work. I would like to express my deepest appreciation to Professor Takashi Yoshimura and Professor Naoto Ishikawa for their valuable advices. I am also grateful to Professor Kiyoshi Tsuge in University of Toyama, Associate Professor Toshiaki Tsukuda in University of Yamanashi, Associate Professor Asako Igashira-Kamiyama in Meiji Gakuin University, Associate Professor Nobuto Yoshinari, Assistant Professor Naoto Kuwamura, Assistant Professor Tatsuhiro Kojima and Assistant Professor Mihoko Yamada for their helpful discussion and valuable advices. I thank Professor Mitsutaka Okumura in Osaka University for the DFT calculation described in Chapter II, Professor Masaki Kawano and Assistant Professor Hiroyoshi Ohtsu in Tokyo Institute Technology School of Science for assisting with the powder X-ray measurement at the SPring-8 described in Chapter II, and Professor Masako Kato and Assistant Professor Masaki Yoshida in Hokkaido University for the measurement of emission lifetimes described in Chapter II. I also thank all my collaborators of Konno Laboratory.

I am grateful for the financial support from the Programs Leading Graduate Schools: ‘‘Interactive Material Science Cadet Program’’ of Osaka University.

Finally, I would like to express my sincere gratitude to my family for their constant supports and encouragement.

February 2017

Kosuke Igawa

Appendix.
Chapter A. Optical Resolution of Thiomalic Acid with Chiral Amine Compound.

A-1. Introduction

Thiomalic acid (2-mercaptosuccinic acid, H_3msa) is one of the simplest chiral thiol-containing dicarboxylic acids and has been widely employed as a raw material for sulfur-containing organic materials. Because commercially available H_3msa is a racemic mixture of the *S* and *R* enantiomers, the preparation of enantiopure H_3msa has been intensively investigated, prompted by the finding of an efficient antirheumatic activity in a gold(I) adduct of the thiomalate ion, *viz*. $\{Na_2[Au(msa)]\cdot 1.75H_2O\}_n$, by Nomiya and coworkers in 1995.[A1] For example, LeBlanc and coworkers reported the asymmetric synthesis of the pure (*R*)-thiomalic acid from L-aspartic acid in three steps in 1997, [A2] while Shiraiwa and coworkers reported the optical resolution of the racemic H_3msa with the use of (*S*)-pea (pea = 1-phenyl-ethanamine), which led to the preferential crystallization of $[(S)\text{-Hpea}]^+\cdot[(R)\text{-}H_2msa]^-$ ([**7**]) in 1998.[A3] The latter method is undoubtedly superior to the former, but the resulting salt, [**7**], has not been crystallographically characterized.

As part of the studies on the rational construction of coordination systems based on chiral thiol-containing multidentate ligands,[A4,5] the investigation of the coordination system derived from H_3msa was started. In the course of this investigation, an optically active single crystal of [**7**] was obtained from the reaction of the racemic H_3msa and (*S*)-pea, and its structure was determined by X-ray crystallography. The optical activity of the compound was confirmed by circular dichroism spectroscopy.

A-2. Experimental section.

A-2-1. Materials.

All other chemicals were commercially available and used without further purification.

A-2-2. Preparation of (*S*)-Hpea·(*R*)-H_2msa ([7]).

rac-H_3msa (5.0 g, 33 mmol) and (*S*)-pea (4.0 g, 33 mmol) were dissolved in 1-PrOH (27 ml). After allowing the mixture to stand in a freezer for one week, the crude product of [**7**] (4.6 g) was collected by filtration. This crude product (2.0 g) was dissolved in 1-PrOH (15 mL) at 353 K to give a colourless solution. The solution was cooled slowly to room temperature and colourless plate-shaped crystals ([**7**]) appeared after several hours. Yield: 0.89 g (22%).

A-2-3. X-ray Structual Determinatons.

The single crystal X-ray diffraction measurement for [**7**] was performed on a Rigaku VariMax RAPID/007HF at 200 K. The intensity data were collected by the ω-scan technique and empirically corrected for absorption.

The structures of complexes were solved by direct methods using SHELXS97. The structure refinements were carried out using full matrix least-squares (SHELXL-97). For (*S*)-Hpea·(*R*)-H_2msa, one (*R*)-H_2msa^- anion, one (*S*)-$Hpea^+$ cation, were crystallographically independent. All non-hydrogen atoms except the C atoms were refined anisotropically. Hydrogen atoms were included in calculated positions.

A-3. Results and discussion.

A-3-1. Crystal Structure of (*S*)-Hpea·(*R*)-H_2msa ([7]).

The molecular structure of (*S*)-Hpea·(*R*)-H_2msa is shown in Figure A-1. The crystallographic data are summarized in Table A-1, and selected bond distances and angles are listed in Table A-2. The absolute configurations of cation and anion, which were confirmed by the Flack parameter, are consistent with the previous prediction made by optical rotation measurements. In (*S*)-Hpea·(*R*)-H_2msa, the amine group of pea is protonated to form a $[Hpea]^+$ cation, while one of the two carboxy groups of thiomalic acid (C3, O1 and O2) is protonated and the other (C4, O3 and O4) is deprotonated to form a H_2msa^- anion. Reflecting the protonation of the O1 atom, the C3–O1 bond length (1.297(3) Å) is obviously longer than that of C3–O2 (1.213 (3) Å). On the other hand, the difference between the C4–O3 (1.276(2) Å) and C4–O4 (1.237(3) Å) bond lengths is smaller, which is consistent with the deprotonated form of the COO^- group. The other bond lengths and angles of the cation and the anion are in the ranges normally observed for related compounds.

In the crystal, the protonated carboxy group of each (*R*)-H_2msa^- anion acts as a hydrogen-bond donor, forming an intermolecular O–H ··· O hydrogen bond with a deprotonated carboxylate group of a neighbouring anion [$O1\cdots O3^{ii}$ = 2.501 (2) Å; symmetry code: (ii) –x, y–1/2, –z + 1]. In addition, its protonated carboxy group acts as a hydrogen-bond acceptor, forming an intermolecular S–H···O hydrogen bond with a thiol group of another neighbouring anion [$S1\cdots O2^{i}$ = 3.2741 (19) Å; symmetry code: (i) –x + 1, y + 1/2, –z + 1]. Based on these two kinds of hydrogen bonds, (*R*)-H_2msa^- anions construct a two-dimensional grid network having rectangular cavities surrounded by four anions parallel to the *ab* plane (Figure A-2). It is noted that each rectangular cavity accommodates an ammonium group of an (*S*)-$Hpea^+$ cation through three N–H···O hydrogen bonds [N1···O4 = 2.751 (3) Å, $N1\cdots O3^{iii}$ = 2.797 (2) Å and $N1\cdots O2^{iv}$ = 2.845 (3) Å ; symmetry codes: (iii) –x, y + 1/2, –z + 1; (iv) x, y + 1, z]. Besides these hydrogen-bonding interactions, two kinds of C–H···π interactions exist in the crystal; one is a contact between a methine group of an (*R*)-H_2msa^- anion and a phenyl group of an (*S*)-$Hpea^+$ cation [$H1E\cdots Cg^{ii}$ = 2.62 Å ; Cg is the centroid of the C6–C12 ring; symmetry code: (ii) –x, y – 1/2, –z + 1], and the other is between a methine group of an (*S*)-$Hpea^+$ cation and a phenyl group of a neighbouring cation [$H6\cdots Cg^{v}$ = 2.85 Å ; symmetry code: (v) –x, y + 1/2, –z] (Figure A-3). The latter interaction connects the two-dimensional grids along the *c* axis, giving a three-dimensional structure in (*S*)-Hpea·(*R*)-H_2msa.

A-4. Conclusion.

From these structural features, it is likely that [(*S*)-Hpea]$^+$ selects the *R* isomer of [H_2msa] such that each [(*S*)-Hpea]$^+$ ammonium group forms multiple hydrogen bonds with three [H_2msa] carboxy groups and that each [(*S*)-Hpea]$^+$ phenyl group forms a C–H interaction with a [H_2msa] methane group, leading to the excellent optical resolution of the racemic H_3msa with the use of (*S*)-pea.

A-5. References.

A1. K. Nomiya, H. Yokoyama, H. Nagano, M. Oda, S. Sakuma, *Bull. Chem. Soc. Jpn.* **1995**, *68*, 2875-2883.

A2. D. J. LeBlanc, R. W. Smith, Z. Wang, H. E. Howard-Lock, C. J. L. Lock, *J. Chem. Soc. Dalton Trans.* **1997**, 3263-3267.

A3. T. Shiraiwa, M. Ohkubo, M. Kubo, H. Miyazaki, M. Takehata, H. Izawa, K. Nakagawa, H. Kurokawa, *Chem. Pharm. Bull.* **1998**, *46*, 1364-1369.

A4. T. Konno, *Bull. Chem. Soc. Jpn*, **2004**, *77*, 627-649.

A5. A. Igashira-Kamiyama, T. Konno, *Dalton Trans.*, **2011**, *40*, 7249-7263.

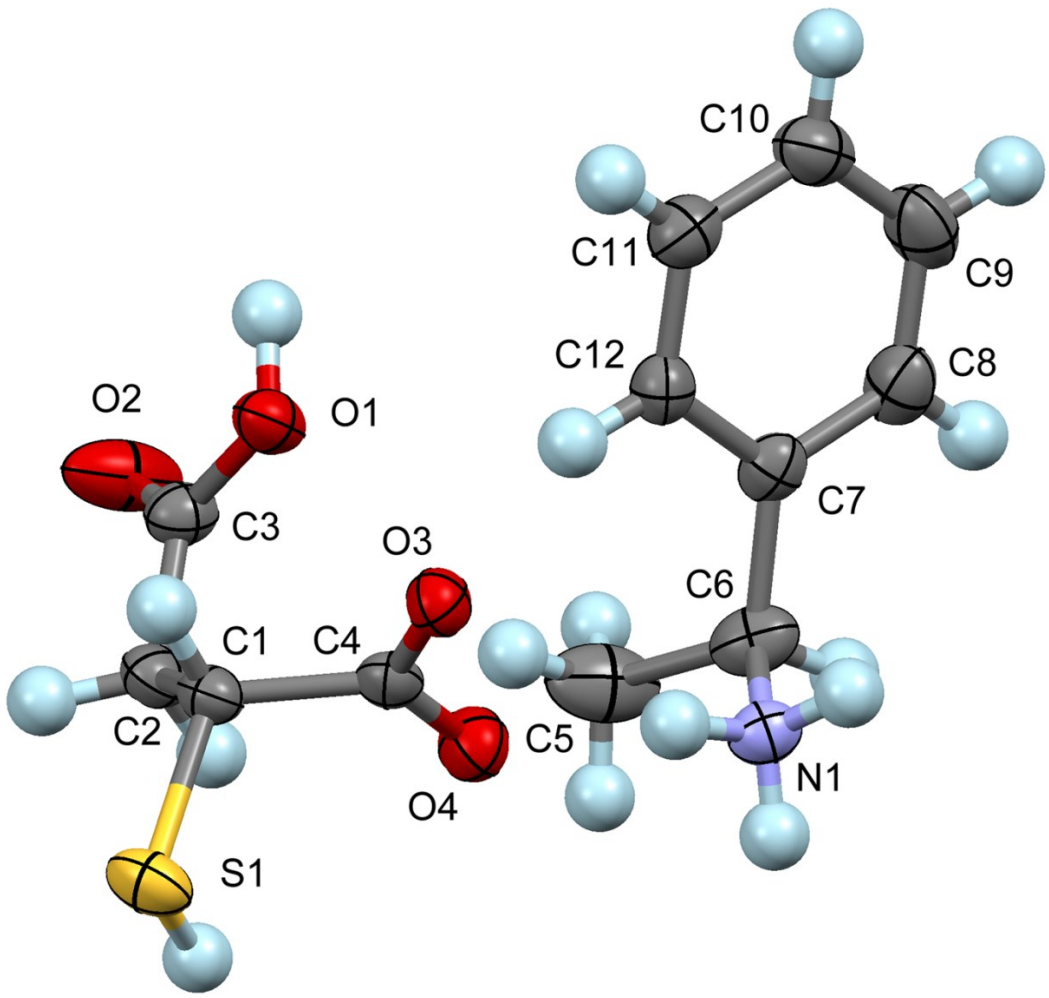

Figure A-1. A view of the asymmetric unit of (**7**), showing the atom-numbering scheme. Displacement ellipsoids are drawn at 50% probability level.

Table A-1. Crystallographic data for (*S*)-Hpea·(*R*)-H_2msa (**7**).

Empirical formula	$C_{12}H_{17}NO_4S$
Formula weight	271.33
Crystal size / mm^3	0.30 ×0.15 ×0.05
Crystal system	Monoclinic
Space group	$P2_1$
a / Å	9.0547(7)
b / Å	8.2304(5)
c / Å	9.3016(7)
α /°	90
β /°	92.760(2)
γ /°	90
V / $Å^3$	692.39(9)
Z	2
T / K	200(2)
ρ_{calcd} / $g \cdot cm^{-3}$	1.301
μ(Mo Kα) /mm^{-1}	0.240
$2\theta_{Max}$	55.0
R(int)	0.0342
GOF	1.117
Flack parameter	0.07(8)
$R1$ (I>2σ(I))[a)]	0.0415
w$R2$ (all data)[b)]	0.1059

a) $R1 = \Sigma||F_o|-|F_c|| / \Sigma|F_o|$. b) $wR2 = [\Sigma(w(F_o^2-F_c^2)^2) / \Sigma w(F_o^2)^2]^{1/2}$.

Table A-2. Bond lengths [Å] and angles [°] for (*S*)-Hpea·(*R*)-H_2msa (**7**).

		Bond lengths	
S(1)-C(1)	1.817(2)	C(5)-C(6)	1.519(4)
O(1)-C(3)	1.298(3)	C(6)-C(7)	1.511(3)
O(2)-C(3)	1.214(3)	C(7)-C(8)	1.386(3)
O(3)-C(4)	1.276(2)	C(7)-C(12)	1.399(3)
O(4)-C(4)	1.237(3)	C(8)-C(9)	1.392(4)
N(1)-C(6)	1.501(3)	C(9)-C(10)	1.380(4)
C(1)-C(2)	1.518(3)	C(10)-C(11)	1.382(3)
C(1)-C(4)	1.531(3)	C(11)-C(12)	1.385(3)
C(2)-C(3)	1.506(3)		
		Angles	
C(2)-C(1)-C(4)	112.52(17)	N(1)-C(6)-C(5)	108.7(2)
C(2)-C(1)-S(1)	111.57(14)	C(7)-C(6)-C(5)	114.5(2)
C(4)-C(1)-S(1)	108.83(14)	C(8)-C(7)-C(12)	118.7(2)
C(3)-C(2)-C(1)	114.13(17)	C(8)-C(7)-C(6)	120.0(2)
O(2)-C(3)-O(1)	123.6(2)	C(12)-C(7)-C(6)	121.3(2)
O(2)-C(3)-C(2)	121.0(2)	C(7)-C(8)-C(9)	120.7(2)
O(1)-C(3)-C(2)	115.39(19)	C(10)-C(9)-C(8)	120.0(2)
O(4)-C(4)-O(3)	125.42(19)	C(9)-C(10)-C(11)	119.9(2)
O(4)-C(4)-C(1)	118.49(18)	C(10)-C(11)-C(12)	120.4(2)
O(3)-C(4)-C(1)	116.09(18)	C(11)-C(12)-C(7)	120.3(2)
N(1)-C(6)-C(7)	108.90(18)		

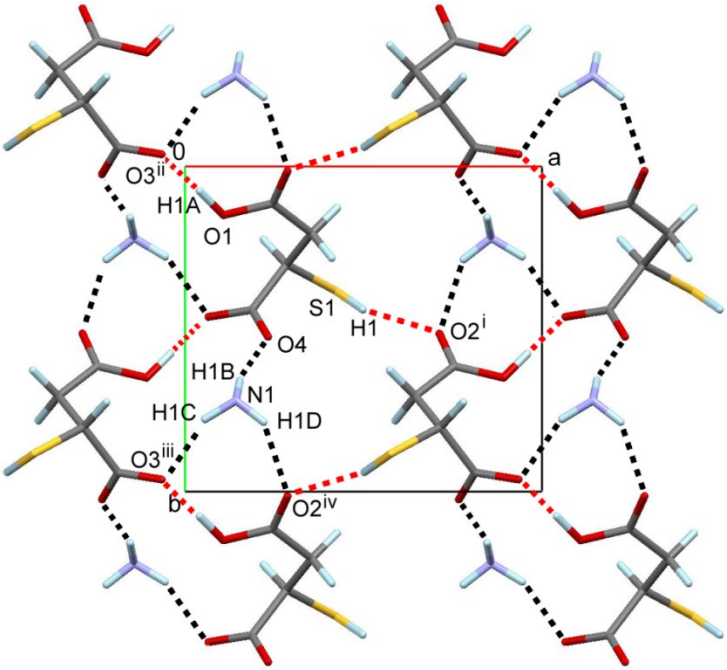

Figure A-2. The two-dimensional grid network of (*R*)-H_2msa^- anions which incorporates ammonium groups of (*S*)-$Hpea^+$ cations in (**7**), viewed parallel to the crystallographic *c* axis. (*S*)-$Hpea^+$ cations, except for their NH_3^+ groups, have been omitted for clarity. The dashed lines show the hydrogen bonds between anions and the hydrogen bonds between anions and cations. [Symmetry codes: (i) –x + 1, y + 1/2, –z + 1; (ii) –x, y – 1/2, –z + 1; (iii) –x, y + 1/2, –z + 1; (iv) x, y + 1, z.]

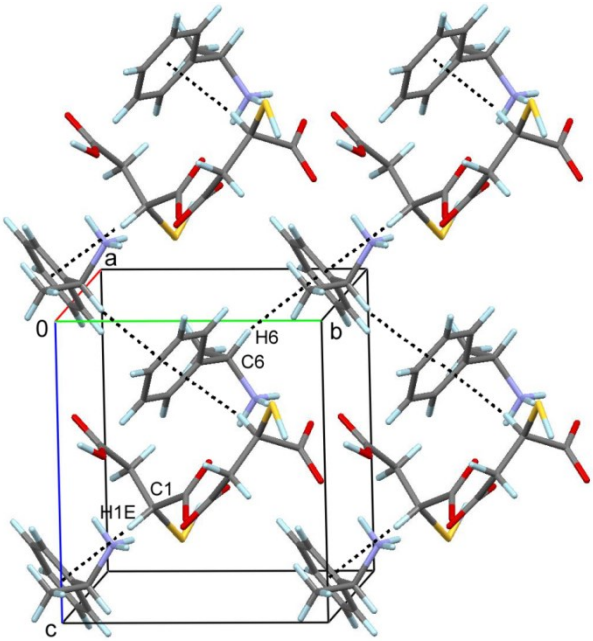

Figure A-3. A view of the C—H···π interaction network in (**7**). Dashed lines indicate the C—H···π interactions.